Refining pedogenic carbonate proxies for improved reconstructions of past terrestrial environmental conditions

by

Timothy Michael Gallagher

A dissertation submitted in partial fulfillment
of the requirements for the degree of
Doctor of Philosophy
(Geology)
in the University of Michigan
2016

Doctoral Committee:

Associate Professor Nathan D. Sheldon, Chair
Assistant Professor Vincent Denef
Associate Professor Gregory J. Dick
Professor Kyger C. Lohmann

Acknowledgements

First, I would like to thank my advisor, Nathan Sheldon, for taking me on as a student, giving me the opportunity to pursue a wide variety of questions during my PhD, and providing helpful advice through it all. I would also like to thank my committee members for providing constructive feedback and supporting an ever-adjusting dissertation plan. Thanks to my coauthors, Mike Hren, Jeff Mauk, Sierra Petersen, Nur Gueneli, and Jochen Brocks, for their helpful comments and assistance with data collection.

Thanks also to all of the lab-mates who listened and helped me work through my ideas (even if the slides were completely blank). Thanks (and sorry) to Sara Leon who crushed so, so many rocks and filled innumerable tin capsules without ever uttering a word of complaint (to my face). Thanks to Lora Wingate for teaching me a lot about machines and always letting me borrow equipment and consumables when I was in a bind. And thanks to all the friends and fellow graduate students in the department who helped make the past five years enjoyable.

This work would not have been possible without the fellowships from the National Science Foundation Graduate Research Fellowship Program and the Department of Earth and Environmental Sciences. My dissertation research was supported by grants from American Philosophical Society, the American Association of Petroleum Geologists Foundation, the Geological Society of America, the Rackham Graduate School, and the Scott Turner Fund.

I would like to thank my parents and sister for all the love and support they provided through the years. Finally and most of all, thanks to Allie for talking me into this whole PhD and

international adventure we have been the past eight years (granted it didn't take much convincing) and always being there with me every step of the way.

Table of Contents

List of Tables

List of Figures

List of Appendices

Abstract

Continental paleoclimate records provide a means to assess regional climate variability through time and assess how the evolution of the terrestrial biosphere has driven and responded to environmental change. Fossil soils (paleosols) are a particularly useful paleoclimate archive, because they are widely distributed throughout the geologic record. Carbonate clumped isotope paleothermometry is an exciting new proxy for paleosols, as it has the potential to assess temperature seasonality. Yet the processes underlying soil carbonate formation and clumped isotope temperature resetting must be further understood before this proxy can be effectively applied. My dissertation centers on improving understanding of the processes controlling soil carbonate formation and critically evaluating the potential resetting of clumped isotope carbonate data from terrestrial deposits.

In Chapter 2, I use modern samples to explore seasonal biases associated with the clumped isotope composition of soil carbonate. The results demonstrate that soil carbonate can form at or below mean annual temperatures. The cold nature of these results is explained by the annual timing of soil water depletion, which is driven by patterns of seasonal precipitation and evapotranspiration. In Chapter 3, modern soil environmental data are compiled to examine how soil temperatures relate to surface air temperatures and to quantify systematic biases that will affect paleosol proxies. Seasonal fluctuations in soil moisture are used to predict the seasonal timing of pedogenic carbonate formation. Soil temperature data indicate that pedogenic

carbonate is more likely to record warm season bias relative to mean annual air temperature. In Chapter 4, I use clumped isotope and organic biomarker analyses on the 1.1 Ga Nonesuch Formation to explore how easily the clumped isotope thermometer can be reset on geologic samples and to evaluate the performance of new solid-state reordering models. Using a solid-state reordering model, I illustrate that the synsedimentary and early-diagenetic calcite were partially reset to elevated temperatures. Taken together, these results illustrate factors that must be considered when producing environmental reconstructions from pedogenic carbonate and other terrestrial archives. These findings provide guidance on how to extract accurate paleoclimate information from paleosol carbonate and highlight the need for a process-based understanding of pedogenic carbonate formation.

CHAPTER 1

Introduction

Paleoclimate data provides a means to test our understanding of the Earth's climate system and to develop more accurate predictions of how the Earth will respond to future climate change. While much paleoclimate work has centered on the marine realm, terrestrial paleoclimate data provides an important and complementary perspective. There exist fundamental differences between terrestrial and marine paleoclimatology, both in the specific climate variables that can be reconstructed (e.g. air temperature vs. seawater temperature; precipitation vs. salinity) and in the fundamental nature of the records that are produced. Importantly, marine records tend to provide a more globally integrative climate perspective, whereas terrestrial archives are inherently more local.

The terrestrial and marine response to major global climate events is not always uniform. For example, during the Eocene-Oligocene transition (33.9–33.5 Ma) which marks the onset of Antarctic glaciation, marine geochemical records indicate a fall in atmospheric pCO_2 was accompanied by high latitude ocean cooling of 5°C (Pearson et al., 2009; Liu et al., 2009). The terrestrial temperature response during this event was heterogeneous, with some coastal areas recording a similar drop in mean annual temperature while other regions display no evidence of cooling (Sheldon et al., 2012; Hren et al., 2013). Understanding the complex and spatially

variable response of terrestrial environments to global change is especially important with respect to modern global warming. However, impactful changes in terrestrial climate may not always be captured by mean annual climate variables. For example, shifts in the seasonal timing of precipitation or the frequency of certain extreme phenomena (e.g. droughts and floods) can significantly affect terrestrial ecosystems and pose societal challenges relating to water availability and food security.

The objective of this dissertation is to refine our understanding of how carbonate minerals can be used as a terrestrial paleoclimate archive. My focus is predominantly on pedogenic carbonate (i.e. carbonate authigenically precipitated in soils), which is a phenomenon typically restricted to environments where annual precipitation falls below 100 cm (Cerling and Quade, 1993; Royer 1999; Retallack, 2005). In this dissertation, I assess the environmental factors that control the seasonal formation of pedogenic carbonate, explore the implications of seasonal formation on paleoclimate reconstructions, and assess evidence for post-depositional alteration of terrestrial deposits.

1.1 Paleosols as a Paleoclimate Archive

Paleosols (fossil soils) can be used as an archive of paleoclimate information, because climate is a primary factor controlling soil formation (Jenny, 1941). For example, temperature and moisture availability affects the rate of chemical weathering and secondary mineral formation in soils. Unlike other terrestrial climate archives, such as tree rings, which become rare beyond the past few hundred to thousands of years, the geologic record of paleosols extends much longer, with the earliest paleosols dating to the Archean (e.g. Rye and Holland, 1998). Paleosols also offer certain advantages as compared to other terrestrial paleoclimate archives. In

addition to their existence deep within Earth's history, paleosols tend to be more frequently and evenly deposited within the sedimentary record than these other archives. Furthermore, the long formation time of soils (10^3–10^6 years) means that paleosols are more likely to preserve an integrated, time-averaged record of climate, whereby short-term climate anomalies may be smoothed out (Sheldon and Tabor, 2009).

While certain paleoclimate proxies are based on structural aspects of soils and paleosols (e.g. depth to Bk horizon precipitation proxy; Retallack, 2005), a greater amount of work has centered on developing paleoclimate proxies derived from the geochemistry of paleosols. This geochemical effort can be broadly subdivided into two approaches: one that focuses on the bulk elemental composition of the paleosols and the other that uses specific minerals preserved in paleosols. The bulk geochemistry approach is based on the understanding that enhanced chemical weathering and secondary mineral formation will occur under warm and wet climates. So called "pedo-transfer functions" have been developed based on the bulk composition of modern soils. Bulk soil proxies have been used to reconstruct climate variables such as mean annual precipitation (Sheldon et al., 2002; Nordt and Driese, 2010) and mean annual temperature (Gallagher and Sheldon, 2013). Uncertainty surrounding these pedo-transfer functions increases as one goes further back in time. Oftentimes, it is also difficult to constrain formation times for individual paleosols within stacked sequences, which raises the possibility that reconstructed climatic shifts could instead be attributed to an uneven formation age distribution.

Mineral-specific paleosol proxies can be derived from the relative abundance of certain minerals as well as the isotopic composition of authigenically formed soil minerals. For example, the relative abundance of iron (oxyhydr)oxides, goethite to hematite, in soils is related to the amount of annual precipitation (Hyland et al., 2015). Isotopic approaches to constrain formation

temperatures and hydrological shifts include measuring the oxygen and hydrogen isotope composition of specific minerals, such as goethite, kaolinite or smectite (Delgado and Reyes, 1996; Yapp, 2000) or measuring the oxygen isotope composition of mineral pairs (Tabor, 2007). Numerous paleoenvironmental proxies have also been developed based on the isotopic composition of soil carbonate minerals, including calcite and siderite (e.g. Cerling 1984; Ludvigson et al., 1998), with the former being the focus of this dissertation. With both bulk and mineral specific paleosol proxies, it is also important to note that caution must always be taken to evaluate if later geochemical alteration occurred during burial before applying these proxies.

1.2 Pedogenic Carbonate

Pedogenic carbonate is a prominent feature in semi-arid and arid terrestrial environments, with the total amount of carbon stored in pedogenic carbonate exceeding that of land plants (Monger et al., 2015). It plays an important role in dry-land ecosystems by filling pore space, thereby inhibiting the percolation of water into soils and increasing the water holding capacity of the soil relative to the parent material (Duniway et al., 2007). Pedogenic carbonate can also reduce the availability of phosphorus for plants due to precipitation of Ca-P minerals within the calcic horizon or sorption reactions with $CaCO_3$ (Lajtha and Schlesinger 1988). Interest in using the geochemistry of pedogenic carbonate as a paleoclimate archive expanded after it was shown that their oxygen and carbon stable isotope composition was directly related to environmental factors (Cerling, 1984). The oxygen isotope composition of pedogenic carbonate is influenced by both temperature and the isotopic composition of soil water, which in turn is a function of the initial isotopic value of precipitation and subsequent evaporation. The carbon isotope value of pedogenic carbonate reflects the isotopic composition of soil CO_2, which is primarily controlled

by the composition of soil organic matter. The oxygen isotope composition of pedogenic carbonate preserved in paleosols has been used to reconstruct changes in temperature (e.g. Dworkin et al., 2005; Cleveland et al., 2008), hydrology (e.g. Amundson et al., 1996; Deutz et al., 2001), and elevation (e.g. Garzione et al., 2000; DeCelles et al., 2007). The carbon isotope composition of pedogenic carbonate has been used to reconstruct the relative abundance of C_3 and C_4 plants in overlying vegetation (e.g. Quade and Cerling, 1995; Fox and Koch, 2003; Levin et al., 2004) as well as to estimate past atmospheric pCO_2 values (e.g. Cerling, 1991; Ekart et al., 1999; Breecker et al., 2010).

The effectiveness of climate reconstructions derived from the geochemistry of pedogenic carbonate relies on an accurate understanding of the processes that control the seasonal timing of carbonate formation. The original expectation was that the geochemical composition of pedogenic carbonate would tend to reflect the mean growing season conditions (Cerling and Quade, 1993). However, more recently, evidence from modern soils in New Mexico suggested that pedogenic carbonate may instead form during periods of excessive dryness that differ significantly from mean growing season conditions (Breecker et al., 2009).

The advent of carbonate clumped isotope thermometry offered a new tool to assess the seasonal formation of pedogenic carbonate. Carbonate clumped isotope thermometry is based on the observation that the abundance of bonds between rare isotopes of carbon and oxygen (e.g. ^{13}C and ^{18}O) is controlled by the temperature of carbonate formation (Ghosh et al., 2006; Eiler, 2011). Initial clumped isotope studies of pedogenic carbonate suggested that pedogenic carbonate tends to exhibit a warm-season bias (Passey et al., 2010; Quade et al, 2013; Hough et al., 2014). However, clumped isotope analyses of pedogenic carbonate collected along an elevation transect in the Andes documented formation temperatures close to mean annual

temperature in areas where precipitation was concentrated during the summer months (Peters et al., 2013). A modeling study by Meyer et al. (2014) further suggested that the phenology of overlying vegetation could affect the timing of pedogenic carbonate formation.

Great strides have been made in developing pedogenic carbonate as a paleoclimate archive; however, areas of uncertainty persist that need to be addressed in order to improve its utility for climate reconstructions. For example, the majority of clumped isotope studies of modern carbonate bearing soils document a warm-season bias, but as the results of the Peters et al. (2013) study illustrate, this particular bias may not always apply. Additionally, the majority of clumped isotope studies of modern pedogenic carbonate have focused on carbonate that forms on the underside of large clasts, whereas pedogenic carbonate preserved in paleosols is often nodular in form. It has also been observed that the soil environment can differ substantially from the surface environment due to processes such as excess ground heating (Quade et al., 2013), causing soil temperatures to deviate significantly from air temperatures. Therefore, a thorough understanding of the factors controlling pedogenic carbonate formation are required to constrain the biases that may be imparted on the carbonate.

1.3 Structure of Thesis

The seasonal processes that control pedogenic carbonate formation are investigated in Chapter 2 through examination of ten modern carbonate-bearing soils that formed under different seasonal precipitation regimes. The carbonate clumped isotope temperatures of the pedogenic carbonate are compared to modeled seasonal variation in soil temperature and moisture. This approach is used to assess if a warm-season formation bias can always be presumed for

pedogenic carbonate and to evaluate if seasonal fluctuations in soil moisture exhibit a control on the timing of carbonate formation.

In order to improve environmental reconstructions from pedogenic carbonate, a better understanding of how fluctuations in soil temperature and moisture to climate variables, such as air temperature and precipitation, is required. Instrumental soil temperature and moisture data was compiled from the Soil Climate Analysis Network in Chapter 3 in order to investigate soil temperature fluctuations relative to air temperature. Systematic biases are assessed between mean annual and mean soil temperature. The temperature biases likely to be recorded by pedogenic carbonate are assessed by first using seasonal trends in soil moisture depletion to identify likely periods of carbonate formation. Soil temperatures during these time intervals are then compared to mean annual air temperature in order to quantify the relative likelihood of a warm-season bias.

Chapter 4 examines issues surrounding the alteration of terrestrial paleoenvironmental archives during diagenesis and burial. This chapter focuses on samples from the Nonesuch Formation, which was deposited in a lacustrine environment approximately ~1.1 Ga. In order to better constrain the thermal history of this unit, I compare organic thermal maturity data to the carbonate clumped isotope composition of three different carbonate pools (sedimentary, early-diagenetic, later-stage veins). Maximum burial temperatures are assessed and the likelihood of a spatially variable thermal history is explored using the geochemical data and solid-state reordering models.

Collectively, these new results will demonstrate that a number of complicating factors exist that must be considered when reconstructing paleoclimate from carbonate preserved in terrestrial sedimentary archives. However, these complications can be overcome by improving

our understanding of the processes that control pedogenic carbonate formation in modern soils and employing a multi-proxy approach when producing environmental reconstructions.

1.4 References

Amundson, R., Chadwick, O., Kendall, C., Wang, Y., and DeNiro, M., 1996, Isotopic evidence for shifts in atmospheric circulation patterns during the late Quaternary in mid-North America: Geology, v. 24, p. 23-26.

Breecker, D.O., Sharp, Z.D., and McFadden, L.D., 2009, Seasonal bias in the formation and stable isotopic composition of pedogenic carbonate in modem soils from central New Mexico, USA: Geological Society of America Bulletin, v. 121, p. 630-640.

Breecker, D.O., Sharp, Z.D., and McFadden, L.D., 2010, Atmospheric CO_2 concentrations during ancient greenhouse climates were similar to those predicted for A.D. 2100: Proceedings of the National Academy of Sciences of the United States of America, v. 107, p. 576-580.

Cerling, T.E., 1984, The stable isotopic composition of modern soil carbonate and its relationship to climate: Earth and Planetary Science Letters, v. 71, p. 229-240.

Cerling, T.E., 1991, Carbon dioxide in the atmosphere: evidence from Cenozoic and Mesozoic paleosols: American Journal of Science, v. 291, p. 377-400.

Cerling, T.E., and Quade, J., 1993, Stable Carbon and Oxygen Isotopes in Soil Carbonates, *in* Swart, P.K., Lohmann, K.C., Mckenzie, J., and Savin, S., eds., Climate Change in Continental Isotopic Records, Volume 78: Geophysical Monograph, American Geophysical Union Geophysical Monograph, p. 217-231.

Cleveland, D.M., Nordt, L.C., Dworkin, S.I., and Atchley, S.C., 2008, Pedogenic carbonate isotopes as evidence for extreme climatic events preceding the Triassic-Jurassic boundary: Implications for the biotic crisis?: Geological Society of America Bulletin, v. 120, p. 1408-1415.

DeCelles, P.G., Quade, J., Kapp, P., Fan, M., Dettman, D.L., and Ding, L., 2007, High and dry in central Tibet during the Late Oligocene: Earth and Planetary Science Letters, v. 253, p. 389-401.

Delgado, A., and Reyes, E., 1996, Oxygen and hydrogen isotope compositions in clay minerals: A potential single-mineral geothermometer: Geochimica Et Cosmochimica Acta, v. 60, p. 4285-4289.

Deutz, P., Montanez, I.P., Monger, H.C., and Morrison, J., 2001, Morphology and isotope heterogeneity of Late Quaternary pedogenic carbonates: Implications for paleosol

carbonates as paleoenvironmental proxies: Palaeogeography Palaeoclimatology Palaeoecology, v. 166, p. 293-317.

Duniway, M.C., Herrick, J.E., Monger, H.C., 2007, The high water-holding capacity of petrocalic horizons: Soil Science Society of America Journal, v. 71, p. 812–819.

Dworkin, S.I., Nordt, L., and Atchley, S., 2005, Determining terrestrial paleotemperatures using the oxygen isotopic composition of pedogenic carbonate: Earth and Planetary Science Letters, v. 237, p. 56-68.

Eiler, J.M., 2011, Paleoclimate reconstruction using carbonate clumped isotope thermometry: Quaternary Science Reviews, v. 30, p. 3575-3588.

Ekart, D.D., Cerling, T.E., Montanez, I.P., and Tabor, N.J., 1999, A 400 million year carbon isotope record of pedogenic carbonate: Implications for paleoatmospheric carbon dioxide: American Journal of Science, v. 299, p. 805-827.

Fox, D.L., and Koch, P.L., 2004, Carbon and oxygen isotopic variability in Neogene paleosol carbonates: constraints on the evolution of the C-4-grasslands of the Great Plains, USA: Palaeogeography Palaeoclimatology Palaeoecology, v. 207, p. 305-329.

Gallagher, T.M., and Sheldon, N.D., 2013, A new paleothermometer for forest paleosols and its implications for Cenozoic climate: Geology, v. 41, p. 647-650.

Garzione, C.N., Dettman, D.L., Quade, J., DeCelles, P.G., and Butler, R.F., 2000, High times on the Tibetan Plateau: Paleoelevation of the Thakkhola graben, Nepal: Geology, v. 28, p. 339-342.

Ghosh, P., Adkins, J., Affek, H., Balta, B., Guo, W.F., Schauble, E.A., Schrag, D., and Eller, J.M., 2006, ^{13}C-^{18}O bonds in carbonate minerals: A new kind of paleothermometer: Geochimica Et Cosmochimica Acta, v. 70, p. 1439-1456.

Hough, B.G., Fan, M., and Passey, B.H., 2014, Calibration of the clumped isotope geothermometer in soil carbonate in Wyoming and Nebraska, USA: Implications for paleoelevation and paleoclimate reconstruction: Earth and Planetary Science Letters, v. 391, p. 110-120.

Hren, M.T., Sheldon, N.D., Grimes, S.T., Collinson, M.E., Hooker, J.J., Bugler, M., and Lohmann, K.C., 2013, Terrestrial cooling in Northern Europe during the Eocene-Oligocene transition: Proceedings of the National Academy of Sciences of the United States of America, v. 110, p. 7562-7567.

Hyland, E.G., Sheldon, N.D., Van der Voo, R., Badgley, C., and Abrajevitch, A., 2015, A new paleoprecipitation proxy based on soil magnetic properties: Implications for expanding paleoclimate reconstructions: Geological Society of America Bulletin.

Jenny, H., 1941, Factors of soil formation; a system of quantitative pedology: New York and London, McGraw-Hill, xii,281 p. p.

Lajtha, K., and Schlesinger, W.H., 1988, The effect of CaCO3 on the uptake of phosphorus by 2 desert shrub species Larrea-Tridentata (DC.) Cov. and Parthenium incanum: Botanical Gazette, v. 149, p. 328-334.

Levin, N.E., Quade, J., Simpson, S.W., Semaw, S., and Rogers, M., 2004, Isotopic evidence for Plio-Pleistocene environmental change at Gona, Ethiopia: Earth and Planetary Science Letters, v. 219, p. 93-110.

Liu, Z.H., Pagani, M., Zinniker, D., DeConto, R., Huber, M., Brinkhuis, H., Shah, S.R., Leckie, R.M., and Pearson, A., 2009, Global Cooling During the Eocene-Oligocene Climate Transition: Science, v. 323, p. 1187-1190.

Ludvigson, G.A., Gonzalez, L.A., Metzger, R.A., Witzke, B.J., Brenner, R.L., Murillo, A.P., and White, T.S., 1998, Meteoric sphaerosiderite lines and their use for paleohydrology and paleoclimatology: Geology, v. 26, p. 1039-1042.

Meyer, N.A., Breecker, D.O., Young, M.H., and Litvak, M.E., 2014, Simulating the Effect of Vegetation in Formation of Pedogenic Carbonate: Soil Science Society of America Journal, v. 78, p. 914-924.

Monger, H.C., Kraimer, R.A., Khresat, S.e., Cole, D.R., Wang, X., and Wang, J., 2015, Sequestration of inorganic carbon in soil and groundwater: Geology, v. 43, p. 375-378.

Nordt, L.C., and Driese, S.D., 2010, New weathering index improves paleorainfall estimates from Vertisols: Geology, v. 38, p. 407-410.

Passey, B.H., Levin, N.E., Cerling, T.E., Brown, F.H., and Eiler, J.M., 2010, High-temperature environments of human evolution in East Africa based on bond ordering in paleosol carbonates: Proceedings of the National Academy of Sciences of the United States of America, v. 107, p. 11245-11249.

Pearson, P.N., Foster, G.L., and Wade, B.S., 2009, Atmospheric carbon dioxide through the Eocene-Oligocene climate transition: Nature, v. 461, p. 1110-U204.

Peters, N.A., Huntington, K.W., and Hoke, G.D., 2013, Hot or not? Impact of seasonally variable soil carbonate formation on paleotemperature and O-isotope records from clumped isotope thermometry: Earth and Planetary Science Letters, v. 361, p. 208-218.

Quade, J., and Cerling, T.E., 1995, Expansion of C_4 grasses in the Late Miocene of Northern Pakistan: evidence from stable isotopes in paleosols: Palaeogeography Palaeoclimatology Palaeoecology, v. 115, p. 91-116.

Quade, J., Eiler, J., Daeron, M., and Achyuthan, H., 2013, The clumped isotope geothermometer in soil and paleosol carbonate: Geochimica Et Cosmochimica Acta, v. 105, p. 92-107.

Retallack, G.J., 2005, Pedogenic carbonate proxies for amount and seasonality of precipitation in paleosols: Geology, v. 33, p. 333-336.

Royer, D.L., 1999, Depth to pedogenic carbonate horizon as a paleoprecipitation indicator?: Geology, v. 27, p. 1123-1126.

Rye, R., and Holland, H.D., 1998, Paleosols and the evolution of atmospheric oxygen: A critical review: American Journal of Science, v. 298, p. 621-672.

Sheldon, N.D., Costa, E., Cabrera, L., and Garces, M., 2012, Continental Climatic and Weathering Response to the Eocene-Oligocene Transition: Journal of Geology, v. 120, p. 227-236.

Sheldon, N.D., Retallack, G.J., and Tanaka, S., 2002, Geochemical climofunctions from North American soils and application to paleosols across the Eocene-Oligocene boundary in Oregon: Journal of Geology, v. 110, p. 687-696.

Tabor, N.J., 2007, Permo-Pennsylvanian palaeotemperatures from Fe-Oxide and phyllosilicate delta O-18 values: Earth and Planetary Science Letters, v. 253, p. 159-171.

Yapp, C.J., 2000, Climatic implications of surface domains in arrays of SD and delta O-18 from hydroxyl minerals: Goethite as an example: Geochimica Et Cosmochimica Acta, v. 64, p. 2009-2025.

CHAPTER 2

Combining soil water balance and clumped isotopes to understand the nature and timing of pedogenic carbonate formation

2.0 Abstract

Pedogenic carbonate is an important archive for paleoclimate, paleoecology, and paleoelevation studies. However, it can form under seasonal environmental conditions that differ significantly from the mean growing season environment or mean annual conditions, potentially complicating its use for proxy reconstructions. The observed seasonal temperature is typically, but not always, biased high relative to mean annual air temperature (MAT). To evaluate the annual timing of pedogenic carbonate formation, ten different soils were sampled across the western United States. Sites were selected to span a variety of precipitation regimes and soil orders. Precipitation regimes ranged from arid sites (mean annual precipitation (MAP) < 20 cm) that receive the majority of precipitation during the winter to wetter sites (MAP > 50 cm) dominated by summer precipitation. Pedogenic carbonate formation temperatures derived from clumped isotope measurements ranged between 6 and 22 °C, with most samples falling at or below MAT. Clumped isotope temperatures were compared to monthly precipitation normals and modeled monthly values of evapotranspiration and soil water content. Results show that carbonate formation temperatures agree with the annual timing of soil water depletion,

suggesting soil moisture content is a primary control on the timing of pedogenic carbonate formation. Although the seasonal bias is a function of environmental factors that are difficult to reconstruct in paleo-studies, the use of other paleosol proxies can help to assess if changes in clumped isotope temperatures are a function of changes in air temperature or hydrology. These results have important implications for the production of accurate paleoclimate and paleoelevation estimates.

2.1 Introduction

Many soils in semi-arid to arid environments exhibit a distinct calcic horizon identifiable by an accumulation of authigenically precipitated pedogenic carbonate. Depending on the age and texture of the soil, pedogenic carbonate can precipitate as thin filaments, clast undercoatings, root casts, nodules, or continuous indurated horizons (Gile et al., 1966). Pedogenic carbonate preserved in paleosols is of particular interest in paleoclimate research. The occurrence of pedogenic carbonate provides a paleoprecipitation limit, as it tends only to form when mean annual precipitation (MAP) is less than 100 cm (Cerling and Quade, 1993; Royer, 1999; Retallack, 2005). Proxies based on the physical nature of pedogenic carbonate, such as depth in soil profile or horizon thickness, have been developed to reconstruct variables such as MAP and degree of seasonality (Retallack, 1994; Retallack, 2005). Widespread interest in the geochemistry of pedogenic carbonate expanded since it was demonstrated that the oxygen and carbon isotopic composition of the carbonate was a reflection of the environment in which it formed (Cerling, 1984; Cerling and Quade, 1993). Subsequently, the oxygen isotope composition of pedogenic carbonate has been used to reconstruct paleohydrology (e.g. Amundson et al., 1996; Deutz et al., 2001; Fox and Koch, 2004), paleotemperature (e.g. Dworkin

et al., 2005; Cleveland et al., 2008), and paleoelevation (e.g. Garzione et al., 2000; DeCelles et al., 2007). The carbon isotope composition of pedogenic carbonate has been used to reconstruct relative abundances of C_3 and C_4 vegetation (e.g. Quade and Cerling, 1995; Deutz et al, 2001; Fox and Koch, 2003; Levin et al., 2004) as well as atmospheric pCO_2 (e.g. Cerling. 1991; Ekart et al., 1999; Cotton and Sheldon, 2012; Montañez, 2013).

However, complications exist when using pedogenic carbonate as a paleoclimate proxy. The traditional assumption was that pedogenic carbonates form during conditions reflective of the mean growing season environment, which would typically imply soil temperature conditions between average and maximum annual soil temperature (Cerling and Quade, 1993). However, the growing season occurs at different times of the year under different climate regimes. For example, the growing season in the central plains of North America extends from spring to early autumn (Ode et al., 1980), whereas the growing season in the eastern Mojave Desert extends from late autumn to early spring (Beatley, 1974). It has also been documented in modern soils that carbonate can precipitate at times of excessive dryness when climatic conditions differ strongly from the mean growing season conditions (Breecker et al., 2009). These findings suggest that, in some cases, a complicated seasonal bias may strongly affect the formation and isotopic composition of pedogenic carbonate.

Carbonate clumped isotope thermometry is an attractive tool to apply to the study of pedogenic carbonate, as the abundance of doubly substituted rare isotopes in carbonate is predominantly a function of temperature (Ghosh et al., 2006a; Quade et al., 2007; Passey et al. 2010; Eiler, 2011). The carbonate clumped isotope proxy has featured prominently in recent continental paleoclimate (e.g. Passey et al., 2010; Snell et al., 2013; VanDeVelde et al., 2013) and paleoelevation studies (e.g. Ghosh et al., 2006b; Quade et al., 2011; Lechler et al., 2013;

Leier et al., 2013; Fan et al., 2014; Garzione et al., 2014; Huntington et al., 2015). However, relating the temperature of pedogenic carbonate formation to climatic variables such as mean annual temperature (MAT) has proven complicated when analyzing modern samples. For example, clumped isotope studies of pedogenic carbonate in East Africa, Tibet, and the Western United States revealed temperatures reflective of a warm season bias rather than MAT (Passey et al., 2010; Quade et al., 2013; Hough et al., 2014). Quade et al. (2013) highlighted many factors that could complicate the relationship between the temperature of soil carbonate formation and air temperature, including excessive ground heating, damping of temperature variation with depth, slope aspect, and vegetative shading. Despite these factors, Quade et al. (2013) were able to relate many modern carbonate-bearing soils to MAT and warmest average monthly temperature, using a depth-based ground heating model that reflected the generally observed warm-season temperature bias. However, pedogenic carbonates collected along an elevation transect in the Andes showed that clumped isotope derived temperatures can be affected by the timing of seasonal rainfall (Peters et al., 2013). Sites that received the majority of annual rainfall during the summer produced results reflective of mean annual soil temperature, whereas sites dominated by winter rainfall were biased towards warm summer temperatures (Peters et al., 2013). These results demonstrate that studies of pedogenic carbonate cannot always assume a warm-season formation bias.

This paper examines the annual timing of pedogenic carbonate formation under different climate regimes, including sites with different annual precipitation regimes and different growing seasons. This study specifically focuses on carbonate-nodule bearing soils ranging from fine to a relatively coarse texture. By comparing clumped isotope derived temperatures of carbonate formation to modelled seasonal soil temperature fluctuations, we assess the relative roles of

normal climate patterns and other environmental factors. Monthly precipitation normals are considered alongside evapotranspiration in order to determine a monthly soil water balance and to assess its control on the timing of pedogenic carbonate formation. The clumped isotope temperatures will also be used to calculate a $\delta^{18}O$ value for the soil water, allowing for comparison with annual fluctuations in the $\delta^{18}O$ of precipitation.

2.2 Site Distribution

Sites in this study were selected in order to span a range of soil types as well as different temperature and precipitation regimes (Fig. 2.1; Table 2.1). The soils analyzed herein represent three different soil taxonomic orders: Aridisols, Mollisols, and Alfisols. Of these three soil orders, Aridisols tend to be the least developed. They are characteristically dry soils that form in

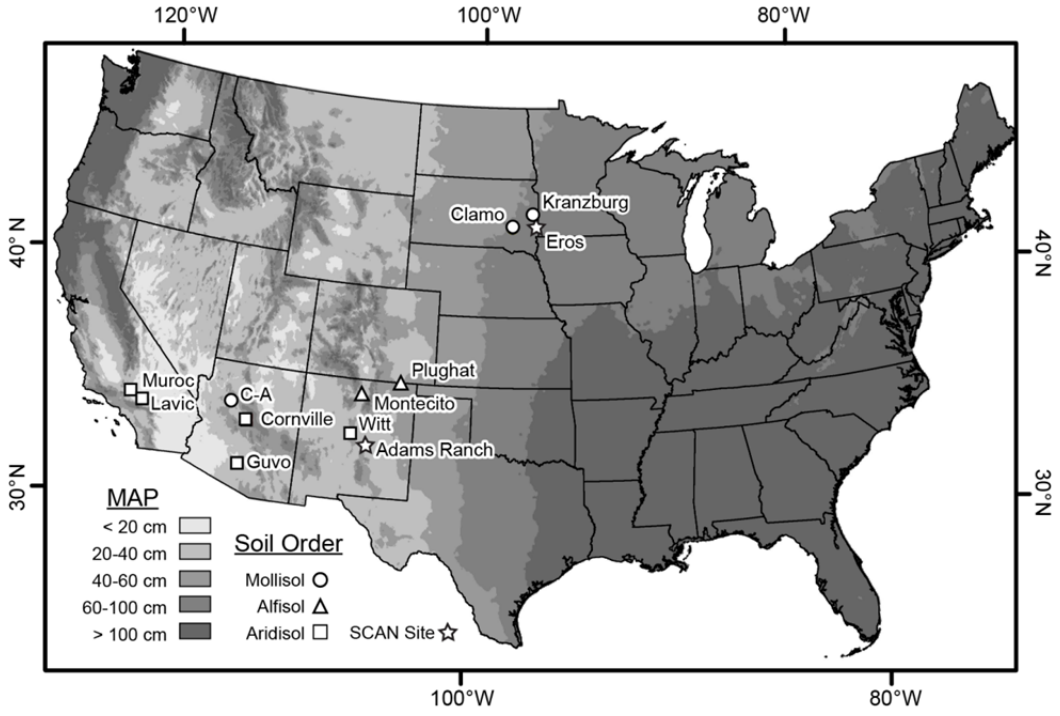

Figure 2.1

Map showing sample localities for pedogenic carbonate nodules analyzed in this study along with a 4 km gridded mean annual precipitation (MAP) dataset interpolated from 1981–2010 climate normals (Prism Climate Group, 2015). Soil orders sampled include Mollisols (circles), Alfisols (triangles), and Aridisols (squares). Soil Climate Analysis Network (SCAN) sites used for data-model comparisons are shown as stars.

Table 2.1 Site Information

Site/Soil	Location N (°)	W (°)	Elevation (m)	Soil Order	Nodule Depth (cm)	MAT (°C)	MAP (cm)
Arid – Winter Precipitation (MAP 10-20 cm)							
Muroc	34.918	-118.152	781	Aridisol	21	17.0	16.9
Lavic	34.604	-117.454	859	Aridisol	25	15.8	14.0
Semi-Arid Monsoonal (MAP 20-40 cm)							
Guvo	32.752	-111.962	481	Aridisol	30	21.6	25.0
Cross-Apache	35.331	-112.805	1646	Mollisol	33	12.7	32.5
Cornville	34.603	-111.854	962	Aridisol	35	16.8	36.4
Semi-Arid (MAP 30-50 cm)							
Plughat	37.023	-103.908	1856	Alfisol	60	10.4	45.8
Montecito	36.392	-105.903	2261	Alfisol	35	8.9	32.4
Witt	34.649	-106.343	2097	Aridisol	70	10.6	38.2
Continental (MAP > 50 cm)							
Kranzburg	44.428	-96.784	521	Mollisol	40	6.2	61.7
Clamo	43.834	-97.993	394	Mollisol	40	8.5	54.7

arid environments and are capable of supporting only a limited amount of plant growth. Due to a lack of moisture and productivity, chemical weathering and soil development tend to be very slow in these soils (Knight, 1991). As compared to Aridisols, Mollisols are generally more developed. They typically underlie temperate grasslands, such as the North American Great Plains and the Eurasian Steppe. The defining characteristic of a Mollisol is a thick (generally >25 cm), organic-rich A-horizon known as the mollic epipedon, which is largely a product of the extensive root system of prairie grasses (Soil Survey Staff, 2014). Of the soil orders examined in this study, Alfisols tend to be the most developed, and they are typically found under temperate deciduous forests (Buol et al., 2011). Soils analyzed as part of this study were generally of a finer-grained texture, allowing for greater water holding capacity and a slower drainage rate than coarse-grained, gravelly soils. With time, fine-grained soils will also tend to form carbonate nodules as opposed to clast undercoatings due, in part, to the lack of coarse fragments that serve to nucleate carbonate precipitation.

The sites examined in this study can be divided into four distinct precipitation regimes (Table 2.1). The two Southern California sites receive the least amount of rainfall, with both sites having a MAP value of less than 20 cm. The little precipitation that these two sites receive tends

to fall during the winter months (December-March). At the wet end of the spectrum, the two South Dakota soils receive the most precipitation with MAP values around 60 cm. These two sites experience a typical continental climate with cold winters, hot summers, and peak precipitation falling during June and July. The remaining Arizona, New Mexico, and Colorado sites have MAP values that fall between these two end-members; and these sites can be subdivided into two distinct groups based on the timing of precipitation. In New Mexico and Colorado, the winters are generally dry with precipitation peaking in late summer (July/August). The three Arizona sites on the other hand are strongly affected by the Arizona monsoon and are driest between April and June before precipitation peaks in August.

2.3 Materials and methods

All of the pedogenic carbonate samples were collected in the field from calcic soil horizons (Cotton and Sheldon, 2012), and only carbonate nodules measuring at least 1 cm in diameter were analyzed, which equates to formation times of at least 2–6 ka (using the transfer function of Retallack, 2005). Where possible, samples were collected below 30 cm depth in order to minimize the effect of diurnal temperature variations and the relative input of atmospheric CO_2. The only exceptions were the two California soils, Muroc and Lavic. These samples were sourced from the California "Soil Series Pedolarium" (see Tabor et al., 2013), and carbonate nodules were slightly shallower than 30 cm depth. Both of these samples had indurated carbonate nodules, however, the nodules from the Lavic soil were approximately 5 mm in diameter.

2.3.1 Climate data and evapotranspiration

Climate data used in this study were taken from two separate sources, the 1981–2010 United States climate normal (Arguez et al., 2012) and the NCEP North American Regional

Reanalysis (NARR) dataset (Mesinger et al., 2006). The motivation behind using these data sources is twofold. They (1) offer the opportunity to compare instrumental climate data that were collected and analyzed using the same methodology across our widely dispersed study sites and (2) provide a long-term record that is less weighted toward anomalous weather events. Monthly temperature and precipitation data were sourced from the 1981–2010 normals (NCDC, 2012). For each site, the climate normals were taken from the closest NOAA weather station that sits at a similar elevation (Table A.1). In order to calculate monthly estimates of reference evapotranspiration (ET_0), the Penman-Monteith equation was used following the methodology of the United Nations FAO-56 paper (Monteith 1981; Allen et al. 1998). The Penman-Monteith equation is defined as follows:

$$ET_0 = \frac{0.408\,\Delta\,(R_n - G) + \gamma \frac{900}{T+273} u_2 (e_s - e_a)}{\Delta + \gamma(1 + 0.36 u_2)} \qquad (1)$$

where Δ is the slope of the saturation vapor pressure relationship, R_n is the net radiation, G is the soil heat flux density, γ is the psychrometric constant, T (°C) is the 2 m air temperature, u_2 is the 2 m wind speed, and e_s–e_a is the saturation vapor pressure deficit. According to the FAO-56 methodology, Δ, G, γ, and e_s–e_a can be calculated if the atmospheric pressure, relative humidity and temperature variability are known. The Penman-Monteith equation was used rather than an empirical equation, because it is a physically based model that combines energy balance with mass transfer (Allen et al., 1998).

For the ET_0 calculations, average, maximum, and minimum monthly temperature data from the 1981–2010 climate normals were used as input variables. Because instrumental data is lacking in spatial and temporal coverage, the remaining climate variables required for the Penman-Monteith equation (pressure, relative humidity, short and longwave radiation, wind speed, and 2 m air temperature) were sourced from the NARR dataset (ESRL-PSD, 2014). This

long-term, high-resolution dataset (0.3 degrees at the lowest latitude) was produced by assimilation of a number of observed climate variables including precipitation, using the very high resolution NCEP Eta model (Mesinger et al., 2006). NARR data compares favorably when analyzed alongside observational data (Mesinger et al., 2006). Monthly means for all input variables were taken from the grid cell containing each respective soil site and averaged over the years 1981 to 2010. These 30-year monthly average values were then entered into the Penman-Monteith equation (Eq. (1)) to calculate an average daily ET_0 value in mm day^{-1} for each month. The average daily ET_0 value was then multiplied by the number of days in the month to give a 30-year average monthly ET_0 value (cm $month^{-1}$).

2.3.2 Soil temperature and soil water balance

Annual variations in air temperature result in similar temperature variations in soils. However, when considering progressive depths in the soil profile, the amplitude of temperature variation is damped and the phase lag increases (Hillel, 1980). For each soil, annual temperature variation was modeled at the pedogenic carbonate sampling depth. The annual soil temperature variability at depth can be modeled using the equation:

$$T(z,t) = T_{avg} + \frac{A_0\left[\sin\left(\omega t - \frac{z}{d}\right)\right]}{e^{z/d}} \qquad (2)$$

where T_{avg} is equal to MAT, A_0 is the amplitude of annual surface temperature variation, z is depth in the soil, ω is the radial frequency ($2\pi/365$), and d is the damping depth (Hillel, 1980; Quade et al., 2013). At each site, different climate data inputs were used to create two different soil temperature models (Models A and B). For model A, T_{avg} was set to MAT, and A_0 was calculated as the difference between the warmest and coldest average monthly temperatures. For model B, T_{avg} was set to mean monthly maximum temperature, and A_0 was calculated as the

difference between the coldest average monthly temperature and the warmest maximum monthly temperature. The damping depth is defined for all sites as:

$$d = \sqrt{\frac{2\kappa}{C_v \omega}} \qquad (3)$$

where κ is the thermal conductivity and C_v is the volumetric heat capacity of the soil. Because κ and C_v change as a function of soil texture (grain size distribution) and water content, we used values measured from soils of a similar texture and at the lowest water content assessed in order to calculate damping depths for each site (Table A.2; Shukla, 2014).

Soil water balance was calculated by comparing the monthly gains (precipitation) and losses (evapotranspiration and percolation below the B-horizon) of water in the soil (Arkley, 1963; Birkeland, 1974). The soil was considered as a single compartment, and the field capacity (maximum water holding capacity) of the soil was calculated based on textural characteristics of the soil series, similar to Tabor et al. (2013). To calculate if there was net storage during a particular month, the monthly ET_0 value was subtracted from the normal monthly precipitation total. There is net storage during a month if precipitation is greater than ET_0, and conversely there is net loss or no accumulation of soil water if ET_0 is greater than precipitation. The total soil water is never allowed to rise above the field capacity of the soil. Also, because actual evapotranspiration is negligible during cold periods of the year due to frost, ET_0 was set to zero when the daily normal minimum temperature is lower than -4°C (Allen et al., 1998). For months that included days below this threshold, the monthly ET_0 value was multiplied by the fraction of days where daily normal minimum temperatures are above -4°C.

2.3.3 Geochemistry

Analytical methods for Δ_{47} analyses are described in detail in Defliese et al. (2015), but will be briefly outlined here. Carbonate nodules were microdrilled at low speed, and between 5

and 10 mg of drilled sample was reacted in anhydrous phosphoric acid at 75°C. The resulting CO_2 was purified off-line using cryogenic separation on a vacuum line and a Porapak-Q filled column held at –25°C. The Δ_{47} of the purified gas was then measured on a Thermo Scientific MAT 253 dual inlet stable isotope ratio mass spectrometer outfitted to collect masses 44–49 in the Stable Isotope Laboratory at the University of Michigan. At least three replicates were analyzed for each sample; data are summarized in Table 2.2.

Table 2.2 Geochemical results from pedogenic carbonate

Site/Soil	n[a]	$\delta^{13}C$ (‰) VPDB	$\delta^{18}O_{carb}$ (‰) VPDB	Δ_{47} (‰) ARF[b]	StDev (‰)[c]	±1 S.E (‰)[d]	Δ_{47} Temp. (°C) 'Ghosh'[e]	Temp (°C) 'Dennis'[f]	Temp (°C) 'Composite'[g]	±1 S.E (°C)[h]	$\delta^{18}O_{sw}$ (‰) VSMOW[i]
Muroc	3	-5.6	-9.3	0.736	0.013	0.012	20	12	12	4	-10.3
Lavic	3	-3.4	-10.4	0.726	0.015	0.012	22	16	15	4	-10.6
Guvo	3	-3.7	-5.4	0.721	0.010	0.012	23	17	16	4	-5.3
Cross-Apache	3	-6.5	-8.5	0.752	0.009	0.012	17	7	7	3	-10.6
Cornville	3	-0.6	-9.9	0.709	0.008	0.012	25	22	21	4	-8.7
Plughat[j]				0.751	0.013	0.008	17	8	7	2	
Pit 1	3	-6.4	-8.2	0.756	0.014	0.012	16	6	6	3	-10.6
Pit 2	3	-6.5	-9.1	0.745	0.012	0.012	18	9	9	3	-10.7
Montecito	3	-4.5	-8.8	0.755	0.009	0.012	16	6	6	3	-11.2
Witt	3	-5.0	-6.6	0.745	0.008	0.012	18	10	9	3	-8.2
Kranzburg	3	-0.7	-6.0	0.732	0.008	0.012	21	14	13	4	-6.6
Clamo	3	-0.6	-5.2	0.705	0.009	0.012	26	23	22	4	-3.9

[a]Number of replicate analyses
[b]Δ_{47} values normalized to the Absolute Reference Frame of Dennis, et al. (2011)
[c]Standard deviation of replicate analyses
[d]Standard error calculated using the long-term σ of standards (0.020‰) divided by the square root of n
[e]Temperature calibration of Ghosh, et al. (2006a), modified for use in the absolute reference frame by Dennis et al. (2011)
[f]Temperature calibration of Dennis and Schrag (2010), modified for use in the absolute reference frame by Dennis et al. (2011)
[g]Composite calibration of studies which analyzed samples at >70°C, excluding siderite (Defliese et al. 2015)
[h]Standard error of calculated temperatures using the 'Composite' calibration
[i]Calculated $\delta^{18}O$ of soil water using the $\delta^{18}O_{carb}$ value and the temperature from the composite calibration
[j]Average values calculated by combining data from both Plughat soil pits

In order to correct for scale compression and nonlinearity, reference gasses of varying bulk isotopic composition were analyzed after being heated to 1000°C in order to attain a stochastic distribution of isotopes among isotopologues (Huntington et al., 2009). CO_2 standards equilibrated with H_2O at 25°C and the Carrara Marble interlaboratory standard were also measured to allow normalization of Δ_{47} values to the absolute reference frame of Dennis et al. (2011). Long-term laboratory analyses of the Carrara Marble standard yield average values of

0.418‰ with a standard deviation of 0.020‰. An empirically derived acid fractionation correction of 0.067‰ was applied to Δ_{47} measurements to account for the digestion temperature of 75°C (Hren et al., 2013; Defliese et al., 2015).

Conventional carbonate stable isotope data ($\delta^{13}C$ and $\delta^{18}O$) were simultaneously measured during Δ_{47} measurement. Empirically derived corrections of +0.36‰ and +0.10‰ were applied to raw $\delta^{18}O$ and $\delta^{13}C$ values, respectively, to account for temperature dependent–fractionation resulting from the transfer of samples through the Porapak-Q column held at -25°C (Petersen et al., 2016). Reference gasses were also passed through the Porapak-Q column held at -25°C, so a further correction to Δ_{47} values was not required. The $\delta^{18}O$ values were then corrected using acid fractionation factor of 1.00830 for calcite reacted at 75°C (Swart et al., 1991). The corrected carbonate $\delta^{18}O$ value and the Δ_{47} temperature were used to calculate the $\delta^{18}O$ value of the precipitating soil water ($\delta^{18}O_{sw}$) using the fractionation factor of Friedman and O'Neil (1977).

$$1000 \ln \alpha_{calcite-water} = 2.78 \times 10^6 T^{-2} - 2.89 \qquad (4)$$

2.4 Results

Complete results of ET_0 and soil water balance calculations are presented in Table A.3. As an example, the soil temperature and water balance model results for two Soil Climate Analysis Network (SCAN) sites, *Eros* and *Adams Ranch*, are shown in Fig. 2.2 and Fig. 2.3. Modelled soil temperatures peak during mid to late July, and reach their nadir between mid-January and early February (Fig 2.2). Soil temperature model B consistently produces higher temperature results than model A, with the difference most pronounced at peak soil temperatures. Monthly precipitation is greater than ET_0 between October and April at the *Eros*

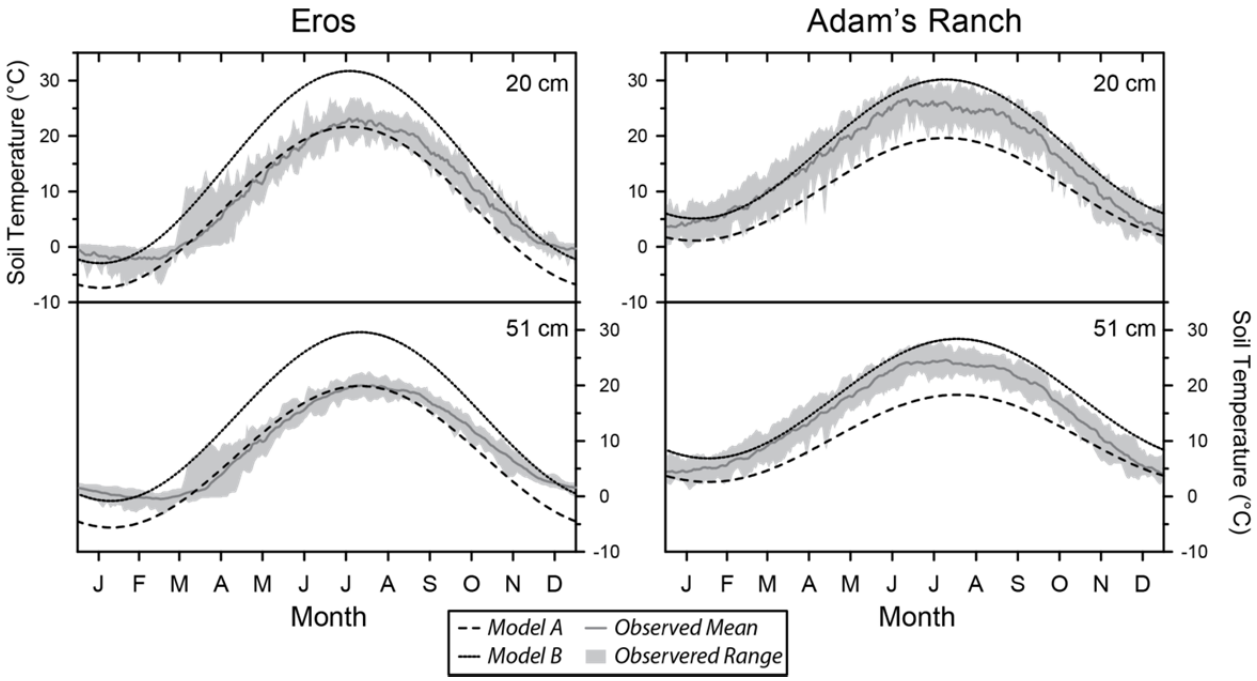

Figure 2.2

Observed and modeled temperatures for the *Eros* and *Adams Ranch* SCAN sites at soil depths of 20 cm (A and C) and 51 cm (B and D). Temperature data was available and compiled between the years 2003–2015 for the *Eros* station and 1997–2015 for the *Adams Ranch* station (NRCS, 2016). The grey window highlights the absolute range of observed temperatures, while the solid gray line shows the mean temperature during the observation period. Daily soil temperatures were recorded at midnight each night. Model A (dotted line) uses the monthly mean, minimum and maximum 1981–2010 monthly normal average temperatures. Model B uses the minimum monthly normal average temperature and the mean and maximum normal maximum average temperatures.

station (Fig. 2.3B) and between December and February at the *Adams Ranch* station (Fig. 2.3E), causing water to accumulate in the soils. As ET_0 becomes greater than monthly precipitation, soil water storage declines until the soil effectively "dries out" during April at the *Adams Ranch* site (Fig. 2.3F). The soil water balance never reaches zero at the *Eros* site, instead sitting at approximately 2 cm between August and October (Fig. 2.3C). Soil water balance results for all of the sites are summarized in Fig. 2.4 by highlighting the months for which there is effectively no net soil water storage.

Complete clumped isotope geochemistry data are presented in Tables A.4 through A.6. Average Δ_{47} values for soil carbonate samples range from 0.756 to 0.705‰, with an average

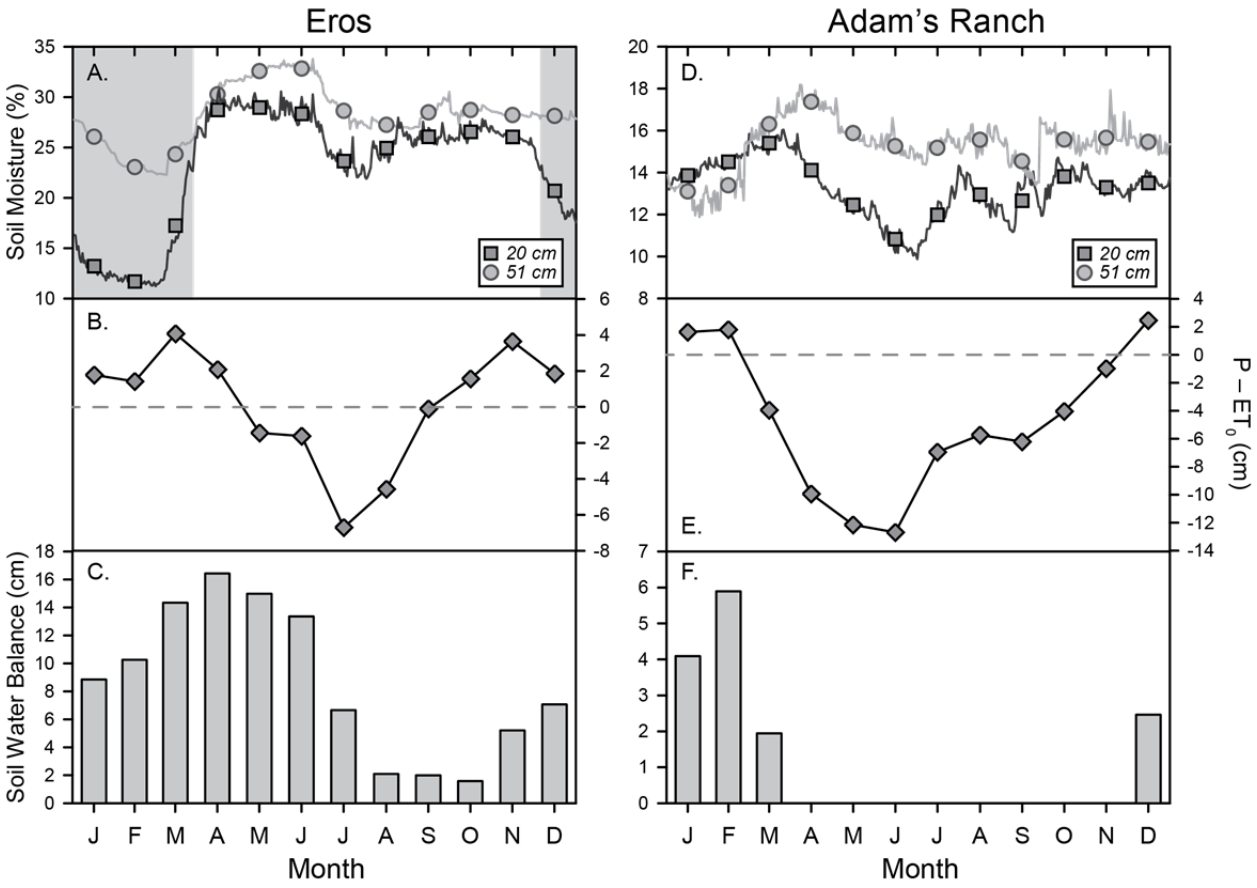

Figure 2.3

Observed soil moisture data and water balance model results for the *Eros* and *Adams Ranch* SCAN sites. Soil moisture data was available and compiled between the years 2003–2015 for the *Eros* station (A) and 1997–2015 for the *Adams Ranch* station (D; NRCS, 2016). Solid lines represent the mean daily soil moisture averaged over the observation period, while the symbols represent average monthly soil moisture content. The area shaded gray for the *Eros* station highlight winter months when soil temperature is below freezing. The difference between normal monthly precipitation and modelled reference evapotranspiration (ET_0) is plotted below (B and E) as well as the modeled soil water storage for each site (C and F).

standard deviation for replicate analyses of 0.011‰ (Table 2). For all samples, the laboratory long-term standard deviation of replicate standard analyses (0.020‰) exceeded that of replicate sample analyses (Petersen et al., 2016). Therefore the standard error was calculated for each sample using the long-term standard deviation of the Carrara marble divided by the square root of the number of replicates. Due to uncertainties based on discrepancies among carbonate temperature calibrations, Δ_{47} results are converted to temperatures using the multiple empirical calibrations in Table 2.2. To date, numerous carbonate clumped isotope temperature calibrations

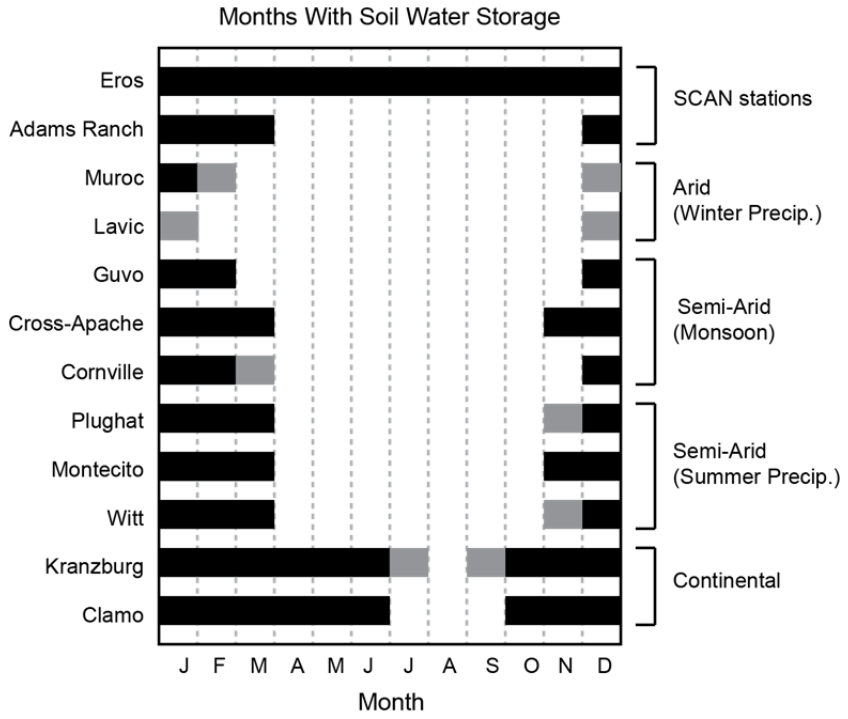

Figure 2.4

Summary of soil water balance calculations for all sites. Months with a positive water balance are shown by the black bar for each site. Months highlighted by a gray bar represent months when the net water balance is less than 0.5 cm month^{-1}.

have been developed using a wide range of materials including synthetic calcite and aragonite (Ghosh et al., 2006; Dennis and Schrag, 2010; Zaarur et al., 2013; Grauel et al., 2013; Petrizzo et al., 2014; Wacker et al., 2014; Tang et al., 2014; Defliese et al., 2015), biogenic calcite and aragonite (Ghosh et al., 2006; Ghosh et al., 2007; Tripati et al., 2010; Thiagarajan et al., 2011; Henkes et al., 2013; Eagle et al., 2013), and siderite (Fernandez et al., 2014). It has been observed that these calibrations can be grouped into two broad categories according to the temperature of the phosphoric acid during sample digestion, where studies that digest samples at temperatures > 70°C tend to produce shallower calibration slopes than those that react samples at 25°C (Fernandez et al., 2014). Exceptions to this observation include the Grauel et al. (2013) calibration, which produced a steep slope from samples reacted at 70°C, and the Petrizzo et al. (2014) calibration, which produced a shallow slope from samples reacted at 25°C. Samples in

this study were digested in phosphoric acid held at 75°C, and analysis of synthetic calcite at the University of Michigan produces results within error of other > 70°C calibrations (Defliese et al., 2015). Due to the ongoing uncertainty involving carbonate temperature calibrations, this paper will focus on temperature results using a composite calibration that combines results from multiple studies that reacted samples in phosphoric acid > 70°C, excluding siderite (Defliese et al., 2015).

Using the composite calibration, the measured Δ_{47} values correspond to a temperature range of 6 to 22°C. Carbonate nodules from two separate sampling pits were analyzed for the Plughat site. The calculated temperatures of 6 ± 3°C and 9 ± 3°C from the two Plughat pits are within error of each other. The final Plughat site temperature (7 ± 2°C) is determined by combining all of the data from both pits. The Clamo site from South Dakota produced the highest Δ_{47} temperature of 22 ± 4°C, while the Montecito site in New Mexico produced the lowest temperature of 6 ± 3°C.

Measured $\delta^{18}O$ values of soil carbonate ($\delta^{18}O_{carb}$) ranged between -10.5 and -5.3‰ VPDB, while $\delta^{13}C$ values ranged between -6.4 to -0.5‰ VPDB. The $\delta^{18}O_{carb}$ values are relatively well dispersed across the ~5‰ range, whereas the $\delta^{13}C$ values cluster in two separate groups. The carbonate from the Kranzburg, Clamo, and Cornville soils all had $\delta^{13}C$ values of 0.5–0.6‰, while the remaining seven soils had pedogenic carbonate with a $\delta^{13}C$ value < -3.3‰.

The $\delta^{18}O$ values for the precipitating soil waters ($\delta^{18}O_{sw}$) were calculated using the Δ_{47} temperatures and the calcite-water fractionation factor of Friedman and O'Neil (1977), and the calculations are summarized in Table A.7. Calculated $\delta^{18}O_{sw}$ values ranged between -3.9 and -11.2‰ VSMOW (Table 2). The two South Dakota sites had $\delta^{18}O_{sw}$ values of -3.9 and -6.6‰, whereas the remaining sites all had $\delta^{18}O_{sw}$ values below -8.7‰. The only exception was the

Guvo soil from Arizona, which had a $\delta^{18}O_{sw}$ value of -5.3‰. Of note, the carbonate sampled from two separate soil pits at the Plughat site produced $\delta^{18}O_{carb}$ values that differed by 0.9‰. However, individually calculated $\delta^{18}O_{sw}$ values of -10.6 and -10.7‰ for each pit were well within error.

2.5. Discussion

2.5.1 Data-model comparison

Given that long-term instrumental soil records are unavailable near our study sites, the effectiveness of the soil temperature and moisture models can be assessed using instrumental data for the *Eros* and *Adams Ranch* SCAN stations. Soil temperature and moisture data is available at the *Eros* station since 2003, while the same data is available for the *Adams Ranch* station since 1997 (NRCS, 2016). The *Eros* station is located relatively close to the Kranzburg site (~80 km) and experiences similar temperatures throughout the year, yet it receives nearly 9 cm more annual precipitation. The *Adams Ranch* station is located ~100 km SE of the Witt site, while sitting ~200 m lower in elevation and receiving about 7 cm more annual precipitation.

In Fig. 2.2, the soil temperature model results at depths of 20 and 51 are compared to instrumental data from both SCAN sites. Model A compares favorably with the observed average soil temperature record between March and October at the *Eros* station, but it under-predicts temperatures between November and February. This discrepancy likely arises because the temperature model does not take into account the effects of freezing and snowpack insulation under extremely cold air temperatures. Poor model performance during very cold points during the year will not affect the overall conclusions of this study, as snowpack and freezing is primarily an issue at the two South Dakota sites and carbonate formation is extremely unlikely at

these temperatures. At the *Adams Ranch* station, model B compares favorably with the average observed soil temperature between February and June. The better performance of model B is likely a result of reduced vegetative cover as compared to the South Dakota sites, which would allow for greater ground heating. Taken together, the temperature data from the SCAN sites suggests that model A produces a more accurate picture of annual soil temperature variation for the South Dakota grassland sites, while model B is likely more valid at the remaining semi-arid to arid sites during late winter to early summer. Some uncertainty remains, but at the very least, the two models together form a range of likely soil temperatures for the majority of the year under a variety of precipitation regimes. More importantly for the purposes of this study, the temperature model performance is best during the times of the year that the soil water balance models indicate soils are likely drying out.

Soil moisture data from the SCAN sites is compared to evapotranspiration and soil water balance results in Fig. 2.3. Observed soil moisture data is calculated by relating the soil dielectric permittivity to soil-water content using a general multi-soil 'loam' calibration equation (Seyfried et al., 2005). The soil water balance results should also not be taken at face value to mean that the soil moisture is completely depleted, but rather the soil effectively begins to dry out. Plants are generally unable to deplete soil water completely, because the adhesive forces to soil particles increase relative to matric water potential forces when soil water content falls. The annual trend of precipitation−ET_0 results compare favorably to the trend in observed soil moisture, especially at 20 cm where the soil moisture will be more readily affected by changes in evapotranspiration. The main discrepancy occurs during the winter at the *Eros* station at 20 cm depth (shaded regions in Fig. 2.3A), which can be explained by freezing soil temperatures during the winter months (Fig. 2.2A). The soil water balance compare more favorably with the 51 cm

soil moisture results. Data from the *Eros* station shows that it is not until late summer-early fall that soil moisture reaches its growing season minimum, whereas April marks the inflection point at the *Adams Ranch* station. Generally the *Eros* soil is much wetter than the *Adams Ranch*, which may imply that it is only during drought years that the soil effectively dries out

2.5.2 Timing of pedogenic carbonate formation

The majority of published clumped isotope measurements on modern pedogenic carbonate have produced formation temperatures that tend to fall between warmest monthly temperature and MAT (e.g. Passey et al., 2010; Quade et al., 2013; Hough et al., 2014). However, soils examined as part of this study tend to be substantially colder than these earlier

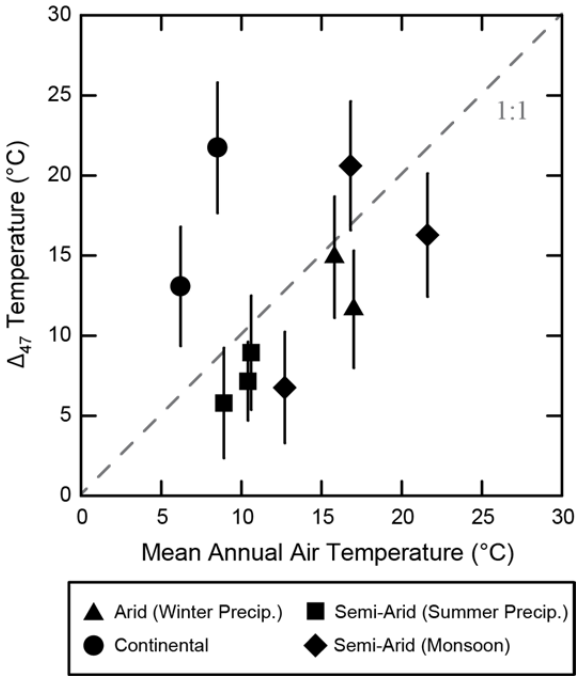

Figure 2.5

Average clumped isotope derived temperatures of pedogenic carbonate formation plotted against mean annual air temperature for each site. The broadly-defined climate regime is indicated by the symbols. The two California sites (triangles) are the driest sites examined in this study (MAP 10-20 cm). The three Arizona sites (diamonds) receive 25–40 cm of annual rainfall, with an exceptionally dry period between April and June. The New Mexico and Colorado sites (squares) receive between 30 and 40 cm of annual rainfall. The South Dakota sites (circles) are the wettest, with MAP in excess of 50 cm. Error bars display a ±1 S.E. window.

studies, with all but three of the Δ_{47} temperatures falling at or below MAT (Fig. 2.5). The long formation time of pedogenic carbonate complicates comparisons to short-term instrumental records of climate and soil conditions. While the concern surrounding short term anomalous weather events (e.g. droughts) is reduced by use of 30 year normal climate data to model typical soil conditions, uncertainty persists regarding regional climate change that occurred while the carbonate nodules formed (2–6 kyrs using the transfer function of Retallack, 2005). Proxy-based climate reconstructions and model simulations indicate that between the Mid-Holocene (~6000 cal years BP) and the preindustrial period (AD ~1700) the North American continental interior generally became more humid and summer temperatures declined slightly (0.5−2°C), while the monsoon-affected North American southwest became drier (Wanner et al., 2008). A small decrease in temperature over this timeframe would serve to increase the extent to which Δ_{47} derived temperatures in the present study fall below MAT. Greater uncertainty surrounds seasonal hydrologic patterns throughout this period, but in the absence of more detailed paleoclimate data we assume that patterns similar to modern were predominant.

It is important to note that choice of clumped isotope temperature calibration can drastically affect the calculated temperatures, especially for the range of Δ_{47} values measured as part of this study. For example, use of the Ghosh (2006a) calibration would result in temperatures at or above MAT for all of our sites (Table 2) and fall more in line with previous studies of pedogenic carbonate that observed Δ_{47}–derived reflecting a warm-season bias (Passey et al. 2010; Quade et al. 2013; Hough et al. 2014). However, the Ghosh (2006a) calibration is not thought to be the appropriate choice for our study, based on the analytical methods used in the University of Michigan Stable Isotope Laboratory and the current understanding of calibration issues related to clumped isotopes (Defliese et al., 2015).

Uncertainties about calibration choice do not confound earlier work that observed a warm-season bias primarily using the Ghosh et al. (2006a) calibration. For example, if reaction temperature is indeed the primary control underlying the calibration discrepancies (Fernandez et al., 2014; Defliese et al., 2015), use of the Ghosh et al. (2006a) calibration was appropriate in the study of Quade et al. (2013), as their samples were reacted at 25°C. In contrast, samples from Hough et al. (2014) study were reacted at 90°C, and most of the calculated temperatures are reduced (average reduction = 6°C) using the composite calibration of Defliese et al. (2015) rather than the Ghosh et al. (2006a) calibration. However, the recalculated temperatures for all but one site still fall above the range of MAT values included in their study. Therefore, while calibration uncertainties do not contradict the documented warm-season bias for some sites, the colder nature of the results presented herein do underscore that a warm-season temperature bias cannot be presumed for pedogenic carbonate in all settings.

As would be expected from the cold nature of the temperature results in this study, only a few of the soils can be explained using the depth-based ground heating model of Quade et al. (2013). Relatively cold pedogenic carbonate formation temperatures are expected to be less common, in part because calcite tends to be more soluble under colder temperatures (Breecker et al. 2009). However, clumped isotope derived temperatures that fall closer to MAT may occur in some settings due to the mediating effect of precipitation on the timing of pedogenic carbonate formation (Peters et al., 2013). As discussed by Breecker et al. (2009), pedogenic carbonate formation can be driven not only by an increase in temperature, but also by a decline in soil pCO_2 or increased Ca^{2+} activity in the soil solution, both of which are tied to precipitation and soil water. Soil pCO_2 at depth is primarily sourced from soil respiration, which is a combination of respiration by roots, microbial decomposition of soil organic matter, and respiration by other

fauna in the soil (Luo and Zhou, 2006). In arid and semi-arid environments, overall productivity is controlled by the availability of water (Noy-Meir, 1973). Small pulses of water to these ecosystems trigger microbial respiration primarily near the soil surface, and it is not until a larger threshold of water is provided to the soil system that vascular plant productivity will increase, thereby increasing plant water uptake and root respiration and driving a build-up of soil pCO_2 at depth (Huxman et al., 2004). Then, as the soil begins to dry out, soil pCO_2 will fall as productivity and microbial respiration of soil organic matter slows (Liu et al., 2002).

The activity and availability of Ca^{2+} is also tied to precipitation in arid and semi-arid environments. Due to the lack of moisture and biological activity, chemical weathering tends to proceed at a much slower rate under arid and semi-arid climate regimes (Knight, 1991; Cotton et al., 2013), thereby limiting the in-situ supply of Ca^{2+} ions to the soil solution. It has long been suggested that dust sourced Ca^{2+} is important under these climate regimes (e.g. Gile et al., 1966; Machette, 1985). In arid settings, as much as 98% of the Ca^{2+} in the soil can be attributed to dust deposition rather than weathering of bedrock derived silicate minerals (Capo and Chadwick, 1999). If the majority of Ca^{2+} is delivered to the surface during dry months, precipitation is required to translocate dust sourced Ca^{2+} into the soil profile to the depth of carbonate formation. Subsequently, as the soil dries out, the activity of Ca^{2+} will increase, promoting the formation of pedogenic carbonate (Breecker et al., 2009). Therefore, a thorough evaluation of annual fluctuations in precipitation and soil water content is necessary to assess the annual timing and formation temperature of pedogenic carbonate.

2.5.2.1 Soil water control

As discussed above, the timing of annual precipitation can influence the timing of pedogenic carbonate formation through its effect on $Ca^{2+}$and soil pCO_2. In addition to monthly

precipitation totals, soil water storage and fluctuations in evapotranspiration need to be considered when assessing the timing of soil moisture depletion. For example, antecedent water that accumulates at cooler times of the year (e.g. winter) can be an important source of water to sustain productivity even when monthly precipitation levels are low (Reynolds et al., 2004). The soil water balance can be driven to zero either by a sizeable decrease in precipitation, or by sustained high evapotranspiration.

Water inputs into the soil are limited under arid climate regimes. Therefore, soil water will likely be exhausted soon after a sizable drop in precipitation. The two California soils, Muroc and Lavic, demonstrate this scenario, as they are the driest sites examined in this study. Both of these sites receive the bulk of their precipitation during the winter months, before experiencing a sharp drop in rainfall during April (Fig. 2.6). Yet these soils are likely drying out ahead of the decline in precipitation due to evapotranspiration losses, with water balance results indicating that the Lavic soil begins to dry out during February and the Muroc soil begins to dry out in March. Clumped isotope temperatures within error of the modeled soil temperature support formation of pedogenic carbonate at these sites during February and March, respectively (Fig 6).

Although the three Arizona soils receive more precipitation on an annual basis than the California soils, the three Arizona soils experience a severe drop in precipitation beginning in April that is driven by the monsoonal climate regime (Fig. 2.6). Soil water balance results indicate that the Cross-Apache and Cornville sites dry out in April, coincident with the decline in rainfall, whereas the hotter Guvo site dries out a month earlier. The clumped isotope temperatures agree with the modeled soil temperatures during April and March for the Cornville and the Guvo sites, respectively (Fig 6). This agreement further supports the idea that the timing

of carbonate formation is biased by a sharp decline in precipitation that coincides with the annual rise in soil temperature and evapotranspiration. However, the third Arizona soil, Cross-Apache, does not follow this explanation as clearly. The clumped isotope temperature from the Cross-Apache site would better agree with the modelled soil temperatures if the soil water balance predicted that the soil began to dry out a month earlier (March). A possible explanation for this discrepancy is the abundance of coarse fragments in the Cross-Apache soil, with the soil series containing up to 35 percent pebbles and cobbles. Coarse fragments were not accounted for when calculating maximum water holding capacity for each soil, and abundant coarse fragments will likely facilitate flow through and reduce the soil's ability to retain water during the cool winter months. Therefore, it is likely that the Cross-Apache soil dries out earlier than the soil water balance model would suggest.

Unlike the California and Arizona soils, the remaining soils analyzed in this study all lack an excessively dry period during the spring/early-summer. At these sites, the driest months are during the winter when temperatures drop below freezing, inhibiting productivity and likely carbonate formation as well. Soil water balance results for Plughat, Montecito, and Witt indicate that these sites all dry out in April (Fig. 2.6). The clumped isotope temperatures from all of these sites fall generally agree with the modelled soil temperature range for April. The clumped isotope temperature window for both of the South Dakota soils is distinct from the other sites examined in this study, as it sits at or near the maximum modeled soil temperature at Bk horizon depth. These two sites also receive the most precipitation and experience the widest annual temperature variation (Fig. 2.6). The soil temperatures peak during July and August, which, for the Clamo soil at least, suggests mid-summer carbonate formation. At first, it may seem counterintuitive that soil carbonate forms when there is still 6 to 8 cm of monthly precipitation

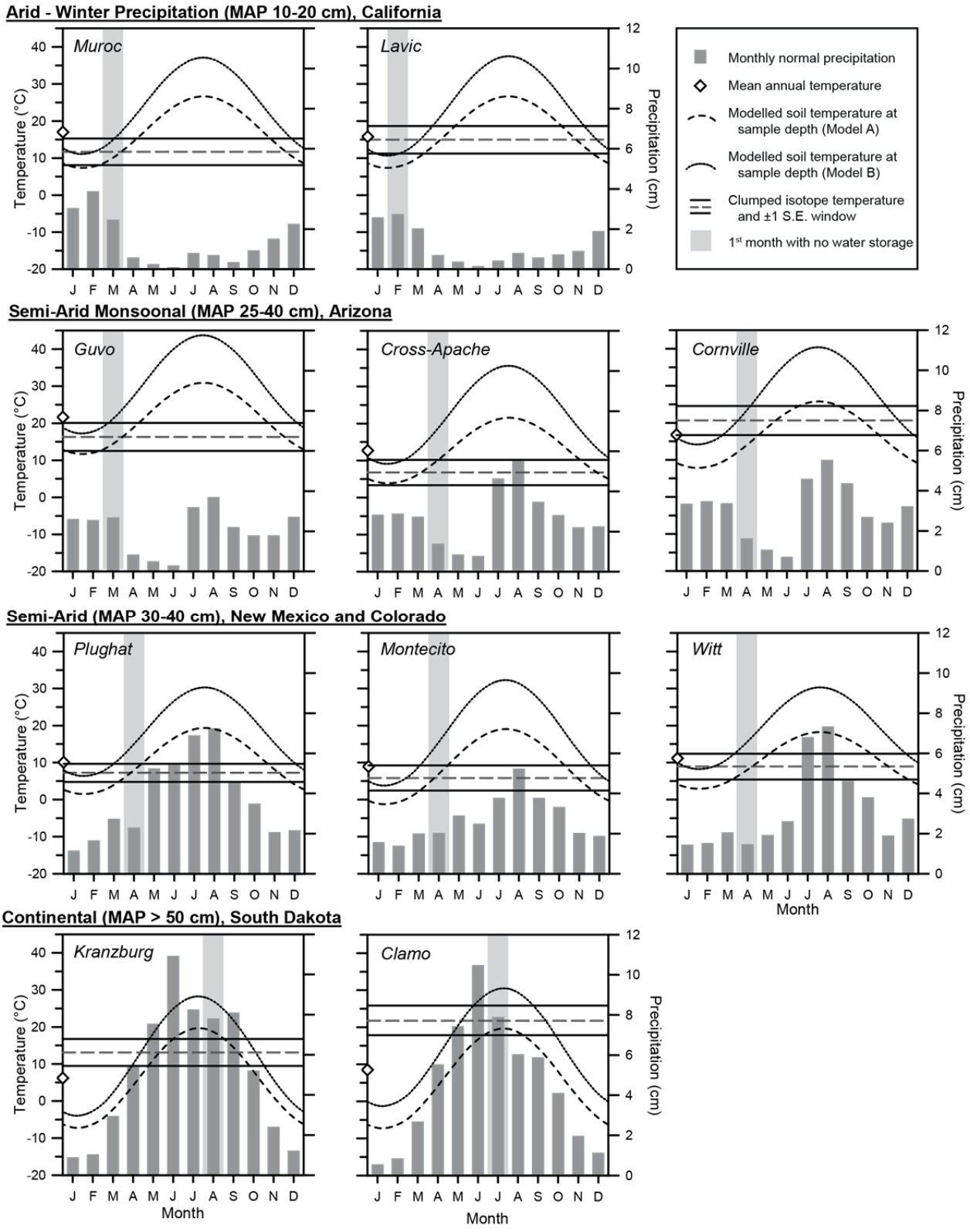

Figure 2.6

Plots for each site showing monthly precipitation totals and mean annual temperature values taken from the 1981–2010 climate normals. Annual variation in soil temperature was modeled for the depth at which

Figure 2.6 (contiued)

the pedogenic carbonate was sampled. Model A (dotted line) uses the monthly mean, minimum and maximum 1981–2010 monthly normal average temperatures. Model B uses the minimum monthly normal average temperature and the mean and maximum normal maximum temperatures. The Δ_{47} derived temperature is shown as a dashed horizontal line with solid lines highlighting a ±1 S.E. window. The light gray vertical bar highlights the first month when soil water storage equal 0.

on average; however, according to the soil water balance results this is precisely the time when water storage at this site is exhausted (Fig. 2.4). At the Kranzburg site, the clumped isotope window overlaps during both late spring and early autumn. Carbonate formation during late August and September is considered more likely due to lower precipitation totals and because a sizeable increase in soil water balance does not occur until October (Fig. 2.4).

It is important to note that there is a level of uncertainty in the evapotranspiration derived soil water estimates, attributable to necessary model assumptions. First, ET_0 is distinct from 'real' evapotranspiration because it represents the theoretical evapotranspiration from a uniform grass cover assuming peak growth conditions (Lhomme, 1997). When applied to agricultural crops, calculated Penman-Monteith ET_0 values are subsequently modified by a crop coefficient depending on the particular species. Adequate data necessary to create a more precise estimate of evapotranspiration were unavailable for vegetation at sites examined in this study. Therefore, the monthly ET_0 values should be considered as an upper limit of actual evapotranspiration (Lhomme, 1997). The use of monthly precipitation totals as soil infiltration totals should also be considered a maximum value, because some fraction may be lost to runoff or interception by vegetation (Huxman et al., 2004). Despite these necessary assumptions, the calculated soil water estimates allow for a detailed evaluation of soil water limitation and help explain variations in Δ_{47}–derived temperatures.

Pedogenic carbonate, which typically forms on timescales of hundreds to thousands of years, can preserve an integrated signal of past environmental conditions. Its integrative nature

depends on, in part, if overprinting (precipitation of younger crystal overgrowths) or recrystallization is the dominant process in the soil (Deutz et al., 2002). It should also be noted that pedogenic carbonate does not necessarily form every year or always during a certain month, potentially forming during shorter-term, anomalous events that deviate from normal patterns, such as droughts (Breecker et al. 2009; Hough et al., 2014). These factors may contribute to some of the uncertainty in the clumped isotope derived temperatures. However, the general agreement between the Δ_{47}-temperatures and the model results suggests that normal climate factors were the primary control on carbonate formation at our sites. As with other paleosol-based paleoclimate proxies, the integrative nature of paleosol Δ_{47} values can be seen as an advantage because the influence of short-lived climatic events are reduced to some degree and do not dominate the signal (Sheldon and Tabor, 2009).

2.5.2.2 Vegetation and excessive ground heating

Additional factors, including vegetation composition and excessive ground heating can affect the annual timing of pedogenic carbonate formation. When other environmental variables are equal, model results suggest that soils under C_3 vegetation may dry out earlier in the year than soils under C_4 vegetation (Meyer et al., 2014). While we do not possess comprehensive vegetation data for all of the sites examined in this study, the sites range from predominantly C_3 to a mixture of C_3 and C_4 plants based on the bulk $\delta^{13}C_{org}$ from the soil surface and A horizons. The fact that most of the sites described herein dry out early in the year lends some credence to their findings. However, recent work from Central Argentina did not identify evidence for different seasons of carbonate formation between predominantly C_3 and mixed (C_3/C_4) vegetation sites (Ringham et al., 2016).

Excess ground heating has been shown to affect the Δ_{47} values of pedogenic carbonate forming in both the southwestern United States and the vegetation-poor Tibetan Plateau (Quade et al., 2013); however, the generally colder nature of the Δ_{47} temperatures suggests that excess ground heating is not as significant of a factor in sites described herein. The reduced impact of excessive ground heating could be because the sites with the least amount of vegetative cover tend to become water limited at an early point in the year when total radiation values are still relatively low. The South Dakota soils do not dry out until the middle of the year; however, these sites also have the thickest vegetative cover, potentially limiting ground heating.

2.5.3 Δ_{47} temperature and the $\delta^{18}O$ of precipitation

Another product of measuring the Δ_{47} values of pedogenic carbonate is that the calculated formation temperature can be used along with the measured $\delta^{18}O_{carb}$ to calculate the isotopic composition of the soil water ($\delta^{18}O_{sw}$) at the time of formation (Ghosh et al., 2006b; Quade et al., 2007; Hough et al. 2014). Relating $\delta^{18}O_{sw}$ to the $\delta^{18}O$ of precipitation ($\delta^{18}O_{precip}$) is complicated by sizable seasonal variation in $\delta^{18}O_{precip}$. According to the Online Isotopes in Precipitation Calculator (OIPC), which interpolates a global dataset of precipitation stable isotope data, seasonal $\delta^{18}O_{precip}$ variability at these sites can be as much as 13.8‰ (Bowen and Revenaugh, 2003; Bowen, 2014). As meteoric water moves through a soil, it can mix with soil water held near the surface that has been evaporatively enriched in ^{18}O; but, it can also move relatively rapidly to depth with less mixing due to the existence of coarse fragments or macropores (Mathieu and Bariac, 1996).

Calculating $\delta^{18}O_{sw}$ offers an opportunity to assess changes in hydrology, even when local environmental factors (e.g. vegetative shading) can cause soil temperature variations. As the results from the separate pits at the Plughat site suggest (Table 2), $\delta^{18}O_{sw}$ can be faithfully

recorded even if there are local variations in soil carbonate formation temperature. However, it remains unclear whether $\delta^{18}O_{sw}$ values record an integrated signal of precipitation received year-round, or if they are biased towards certain seasonal contributions. To assess this point, $\delta^{18}O_{sw}$ values can be compared to OIPC sourced monthly $\delta^{18}O_{precip}$ values. The calculated $\delta^{18}O_{sw}$ values are plotted against a weighted average of monthly $\delta^{18}O_{precip}$ values in Fig. 2.7, where each monthly OIPC $\delta^{18}O$ value was weighted according to the fraction of total precipitation received during that month. The three precipitation scenarios plotted in Fig. 2.7 exhibit the best agreement with the calculated $\delta^{18}O_{sw}$ values. Fig.2.7A includes all precipitation received year-round, Fig.2.7B considers only the first month without soil water storage, and Fig. 2.7C plots a weighted average of the three wettest months. A number of additional scenarios were explored (e.g. driest month, months when $P>ET_0$, etc.) and are shown in Fig. A.1. To assess how well the data compare to the 1:1 line, a modified standard error was calculated for Fig. 2.7, using the 1:1 line instead of a best-fit regression line.

In addition to complications introduced by seasonal variations in $\delta^{18}O_{precip}$, the isotopic composition of soil water can deviate significantly from meteoric water, becoming higher with evaporative loss before the water percolates deeper into the soil, especially in finer-textured soils (Cerling and Quade, 1993). It is important to note that scenarios where $\delta^{18}O_{sw} > \delta^{18}O_{precip}$ are much easier to explain (via evaporative loss) than scenarios where $\delta^{18}O_{sw} < \delta^{18}O_{precip}$. Two sites, Witt and Clamo, consistently appear excessively ^{18}O-enriched, as compared to the remaining sites (Fig. 2.7). The Witt and Clamo soil series are unique amongst our sites in that they are described as having a moderately-slow to slow permeability. Slow permeability in these two soils would explain the observed ^{18}O-enrichment as precipitation will percolate slowly into the soil, thereby increasing the time available for evaporative loss near the soil surface.

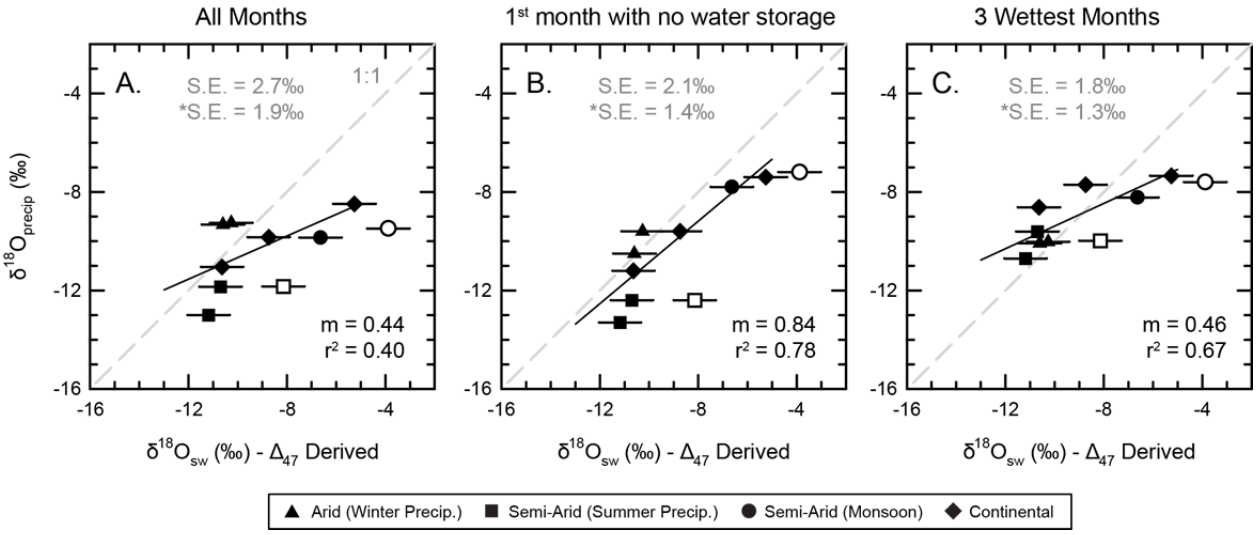

Figure 2.7

Calculated $\delta^{18}O$ values of the soil water ($\delta^{18}O_{sw}$) at the time of pedogenic carbonate formation plotted against OIPC-derived $\delta^{18}O$ values of precipitation ($\delta^{18}O_{precip}$). Fig. 7A plots a weighted average of OIPC values from all months. Fig. 7B includes only the precipitation that falls during the first month where the soil water storage model goes to 0. Fig 7C plots the weighted average of the three wettest months. For Figs. 7A and 7C the monthly $\delta^{18}O_{precip}$ were weighted according to the fraction of annual precipitation received that month. A modified standard error (S.E.) is calculated based on deviation from the 1:1 line considering all 10 sites. The two sites (Clamo and Witt) that are consistently the most ^{18}O-enriched relative to the 1:1 line are shown as white symbols, and a separate standard error (*S.E.) is shown considering only the 8 remaining sites. Also plotted as a solid black line, is a linear regression that excludes the Clamo and Witt sites along with its slope (m) and coefficient of determination (r^2).

Of the many scenarios examined, annually integrated $\delta^{18}O_{precip}$ values produce one of the better relationships with calculated $\delta^{18}O_{sw}$ values, with a S.E. of 2.7‰ (Fig. 2.7A). However stronger relationships are observed when only the first month with no soil water storage (Fig. 2.7B; S.E = 2.1‰) or the three wettest months are considered (Fig. 2.7C; S.E = 1.8‰). Although the latter scenario has a slightly smaller S.E., a number of the $\delta^{18}O_{sw}$ values are more negative than $\delta^{18}O_{precip}$, which is difficult to explain. In contrast, all of the $\delta^{18}O_{sw}$ values exceed $\delta^{18}O_{precip}$ when only precipitation from the month where the soil water balance is considered, with the one exception being the Muroc site (although it is within error of the 1:1 line). Furthermore, a linear regression through the data that excludes the strongly ^{18}O-enriched Clamo and Witt sites has a slope subparallel to the 1:1 line with a fairly strong coefficient of determination ($r^2 = 0.78$).

These results suggest that the $\delta^{18}O_{carb}$ value of pedogenic carbonate will most directly reflect the $\delta^{18}O$ composition of seasonal precipitation falling close to the time of carbonate formation

It is important to note that mixing of soil water under seasonally variable precipitation regimes is a complex process. For example, it has been shown in wet environments characterized by strong seasonal variation in precipitation that tightly bound water can remain isolated in small pores and not mix with subsequent precipitation (Brooks et al., 2010). However in water-limited environments, our results suggest that soil water is less likely to remain unutilized in sizeable quantities across seasons. Although the soils likely do not dry out completely, the water content remains low enough that the $\delta^{18}O_{sw}$ value will be set by recent precipitation. Soil hydrology can be further complicated by overlying vegetation. Variations in rooting depths suggest that woody and herbaceous plants may rely on water uptake from different soil depths in drier environments, and individual plants have been shown to access pools of water at varying depths during different seasons (Dawson and Pate, 1996; Schenk and Jackson, 2002). Variation in vegetation between the sites as well as fluctuations in soil pH may explain some of the variability observed in the calculated $\delta^{18}O_{sw}$ data.

Considering all of the complicating factors, it is encouraging that such a strong relationship exists between the calculated $\delta^{18}O_{sw}$ values and the $\delta^{18}O$ of precipitation that falls during the modeled month of soil water depletion. This overall agreement lends further support to the effectiveness of the soil water balance model results and the conclusion that seasonal fluctuations in soil water balance are controlling the timing of carbonate formation. Additional detailed studies are required from a wider array of sites (across a range of moisture regimes) to examine thoroughly the integration of $\delta^{18}O_{sw}$ and $\delta^{18}O_{precip}$ during pedogenic carbonate

formation. Caution should be taken when interpreting changes in $\delta^{18}O_{carb}$ values for they may be reflective of shifts in local hydrology rather than temperature.

2.5.4 Implications for clumped isotope studies of paleosol carbonates and future directions

It is evident that annual fluctuations in soil water content can control the annual timing of pedogenic carbonate formation. As outlined above, variations in precipitation, evapotranspiration and antecedent water storage control soil water content, and in turn, the timing of pedogenic carbonate formation. Therefore, when interpreting clumped isotope temperature results from a stacked sequence of paleosols, it should be considered whether recorded temperature variations are driven primarily by change in air temperature or a shift in soil hydrology, which may be independent of climate. However, these variables are difficult to constrain directly when evaluating clumped isotope results of paleosol carbonate. An in-depth characterization of paleosols can help to elucidate the primary driver of changes in a particular paleosol clumped isotope record. For example, changes in paleosol texture (grain size) throughout a sequence should be evaluated, as this will partially control water storage outside of the growing season. Reconstructions of paleovegetation from phytolith assemblages, organic matter $\delta^{13}C$, or pedogenic carbonate $\delta^{13}C$ are important, as different plant phenotypes will have different water-uptake strategies and provide variable amounts of shade (e.g. Cerling, 1984; Strömberg and McInerney, 2011). Paleosol climate proxies that reconstruct MAT and MAP independent of pedogenic carbonate can also be used to suggest if a change in air temperature or precipitation regime is more likely (e.g. Sheldon et al., 2002; Sheldon and Tabor, 2009; Nordt and Driese, 2010; Hyland et al., 2015).

Further work is needed on modern pedogenic carbonates, specifically to consider the effects of soil texture and vegetation. Most clumped isotope studies of modern soils have focused

on sandy soils or those with coarse clasts capable of developing carbonate undercoatings. However, the majority of paleosols used for paleoclimatic reconstructions tend to be more developed, with nodular carbonate that represents both longer formation times and potentially different modes of carbonate formation. Most of the soils examined as part of this study were fine-grained and capable of storing sizable volumes of antecedent water, and future work should directly assess the different soil textures under similar climate regimes. The predominantly cooler-nature of our Δ_{47} results may be, in part, attributable to differences in how pedogenic carbonate nodules versus clast undercoatings form over time. Soils examined herein all included nodular horizons that may preserve a longer, more time integrative climate signal of regular seasonal patterns than previous studies that focus on carbonate undercoatings. Importantly, the majority of pedogenic carbonates preserved in the geologic record and those used in paleo-reconstructions are well-formed nodules rather than undercoatings. Thus, the new results herein may reflect a better interpretive structure for understanding Δ_{47} results going forward. The effect different vegetation phenotypes have on pedogenic carbonate formation temperatures still needs to be tested directly. For example, C_3 and C_4 plant productivity can be favored at different points during the year, which may, in turn, affect the seasonality of pedogenic carbonate formation (Ode, et al., 1980; Meyer, et al. 2014).

Considering soil hydrology when discussing clumped isotope results of pedogenic carbonate is especially relevant to paleoelevation studies, because regional uplift can drive changes in regional climate that affect paleoelevation proxies (Ehlers and Poulsen, 2009; Fiorella et al., 2015). As noted above, Δ_{47} temperatures of pedogenic carbonate were notably affected along an elevation transect in the Andes where the seasonality of rainfall varies as a function of elevation. We agree with findings of Peters et al (2013) that the annual timing of precipitation

needs to be considered, because it is the primary input of water into a soil. We also stress that other factors should also be considered including other climatic variables that affect evapotranspiration (e.g. temperature variability and humidity), soil texture, and plant water uptake strategies. The fine-grained nature of most of the soils examined herein highlights the importance of considering soil water storage, because it could allow carbonate formation to lag well-behind precipitation events.

2.6. Conclusions

Our results provide additional credence to the observation that carbonate sourced from modern soils is not always biased towards warm-season temperatures. Clumped isotope temperatures that fall at or below MAT may be less of an exception than published results of modern pedogenic carbonate have documented. When considering clumped isotope derived temperatures of carbonate preserved in paleosols, it is necessary to consider that reconstructed changes in temperature may be indicative of changes in hydrology and vegetation rather than exclusively changes in air temperature.

Clumped isotope temperature variability in modern pedogenic carbonate can be explained by considering a monthly soil water model that accounts for precipitation, evapotranspiration, and soil water storage. Results from this study agree with previous research that suggested the timing of annual precipitation can bias the timing and temperature of pedogenic carbonate formation. The effects of water loss via plant water uptake need to be considered in order to explain all of the sites examined in this study, especially those that lack an excessively dry period during the spring or summer (e.g. the South Dakota sites).

Systematic differences in Δ_{47} results between different soil taxonomic orders were not observed, as it appears that precipitation, evapotranspiration, and antecedent soil water storage are primary controls on the timing of pedogenic carbonate formation. Whereas most previously published clumped isotope studies demonstrated a warm season bias in pedogenic carbonate, the majority of our sites fall at or slightly below MAT. Only the two South Dakota soils that developed under a continental climate were biased well above MAT. The seasonal timing of soil water depletion explains the differences in formation temperatures recorded at our sites. Additionally, the Δ_{47} derived $\delta^{18}O_{sw}$ results suggest that the $\delta^{18}O$ value of the pedogenic carbonate will be seasonally biased towards seasonal precipitation $\delta^{18}O$ values when soil water content is depleted. Future research should investigate the possibility that differences exist in seasonal formation patterns of pedogenic nodules and clast undercoatings, and therefore the environmental data they record. This point is particularly important because most studies of the geologic record rely on nodular carbonate (as examined herein), rather than undercoatings, which have been the focus of most modern clumped isotope calibration studies. The remaining uncertainty does not preclude the use of this approach on paleosol carbonates in order to assess relative changes in local hydrology, but caution must be taken when interpreting the results in light of climatic or tectonic changes.

2.7 References

Allen, R. G., Pereira, L. S., Raes, D., and Smith, M. (1998) Crop evapotranspiration: guidelines for computing crop water requirements. *FAO irrigation and drainage paper* **56**, 300.

Amundson, R., Chadwick, O., Kendall, C., Wang, Y., and DeNiro, M. (1996) Isotopic evidence for shifts in atmospheric circulation patterns during the late Quaternary in mid-North America. *Geology* **24**, 23-26.

Arguez, A., Durre, I., Applequist, S., Vose, R. S., Squires, M. F., Yin, X., Heim, R. R., Jr., and Owen, T. W. (2012) NOAA'S 1981-2010 U.S. climate normals: an overview. *Bulletin of the American Meteorological Society* **93**, 1687-1697.

Arkley, R. J. (1963) Calculation of carbonate and water movement in soil from climatic data. *Soil Sci* **96**, 239-248.

Baldwin, D. S., Rees, G. N., Wilson J. S., Colloff, M. J., Whitworth, K. L., Pitman, T. L., and Wallace, T. A. (2013) Provisioning of bioavailable carbon between the wet and dry phases in a semi-arid floodplain. *Oecologia* **172**, 539-550.

Beatley, J. C. (1974) Phenological events and their environmental triggers in Mojave Desert ecosystems. *Ecology* **55**, 856-863.

Birkeland, P. W. (1974) *Pedology, weathering, and geomorphological research*. Oxford University Press, New York.

Bowen, G. J. (2014) The Online Isotopes in Precipitation Calculator, version 2.2.

Bowen, G. J. and Revenaugh, J. (2003) Interpolating the isotopic composition of modern meteoric precipitation. *Water Resources Research* **39**.

Breecker, D. O., Sharp, Z. D., and McFadden, L. D. (2009) Seasonal bias in the formation and stable isotopic composition of pedogenic carbonate in modem soils from central New Mexico, USA. *Geol. Soc. Am. Bull.* **121**, 630-640.

Brooks, J. R., Barnard, H. R., Coulombe, R., and McDonnell, J. J. (2010) Ecohydrologic separation of water between trees and streams in a Mediterranean climate. *Nat. Geosci.* **3**, 100-104.

Buol, S. W., Southard, R. J., Graham, R. C., and McDaniel, P. A. (2011) *Soil genesis and classification*. Wiley-Blackwell, Chichester, West Sussex ; Ames, Iowa.

Capo, R. C. and Chadwick, O. A. (1999) Sources of strontium and calcium in desert soil and calcrete. *Earth Planet. Sci. Lett.* **170**, 61-72.

Cerling, T. E. (1984) The stable isotopic composition of modern soil carbonate and its relationship to climate. *Earth Planet. Sci. Lett.* **71**, 229-240.

Cerling, T. E. (1991) Carbon dioxide in the atmosphere: evidence from Cenozoic and Mesozoic paleosols. *American Journal of Science* **291**, 377-400.

Cerling, T. E. and Quade, J. (1993) Stable Carbon and Oxygen Isotopes in Soil Carbonates. In: Swart, P. K., Lohmann, K. C., Mckenzie, J., and Savin, S. Eds.), *Climate Change in Continental Isotopic Records*. American Geophysical Union Geophysical Monograph.

Cleveland, D. M., Nordt, L. C., Dworkin, S. I., and Atchley, S. C. (2008) Pedogenic carbonate isotopes as evidence for extreme climatic events preceding the Triassic-Jurassic boundary: Implications for the biotic crisis? *Geol. Soc. Am. Bull.* **120**, 1408-1415.

Cotton, J. M., Jeffery, M. L., and Sheldon, N. D. (2013) Climate controls on soil respired CO2 in the United States: Implications for 21st century chemical weathering rates in temperate and arid ecosystems. *Chemical Geology* **358**, 37-45.

Cotton, J. M. and Sheldon, N. D. (2012) New constraints on using paleosols to reconstruct atmospheric pCO(2). *Geol. Soc. Am. Bull.* **124**, 1411-1423.

Dawson, T. E. and Pate, J. S. (1996) Seasonal water uptake and movement in root systems of Australian phraeatophytic plants of dimorphic root morphology: A stable isotope investigation. *Oecologia* **107**, 13-20.

DeCelles, P. G., Quade, J., Kapp, P., Fan, M., Dettman, D. L., and Ding, L. (2007) High and dry in central Tibet during the Late Oligocene. *Earth Planet. Sci. Lett.* **253**, 389-401.

Defliese, W. F., Hren, M. T., and Lohmann, K. C. (2015) Compositional and temperature effects of phosphoric acid fractionation on Δ_{47} analysis and implications for discrepant calibrations. *Chemical Geology* **396**, 51-60.

Dennis, K. J., Affek, H. P., Passey, B. H., Schrag, D. P., and Eiler, J. M. (2011) Defining an absolute reference frame for 'clumped' isotope studies of CO_2. *Geochimica Et Cosmochimica Acta* **75**, 7117-7131.

Dennis, K. J. and Schrag, D. P. (2010) Clumped isotope thermometry of carbonatites as an indicator of diagenetic alteration. *Geochimica Et Cosmochimica Acta* **74**, 4110-4122.

Deutz, P., Montanez, I. P., and Monger, H. C. (2002) Morphology and stable and radiogenic isotope composition of pedogenic carbonates in late quaternary relict soils, New Mexico, USA: An integrated record of pedogenic overprinting. *Journal of Sedimentary Research* **72**, 809-822.

Deutz, P., Montanez, I. P., Monger, H. C., and Morrison, J. (2001) Morphology and isotope heterogeneity of Late Quaternary pedogenic carbonates: Implications for paleosol

carbonates as paleoenvironmental proxies. *Paleogeogr. Paleoclimatol. Paleoecol.* **166**, 293-317.

Dworkin, S. I., Nordt, L., and Atchley, S. (2005) Determining terrestrial paleotemperatures using the oxygen isotopic composition of pedogenic carbonate. *Earth Planet. Sci. Lett.* **237**, 56-68.

Eagle, R. A., Eiler, J. M., Tripati, A. K., Ries, J. B., Freitas, P. S., Hiebenthal, C., Wanamaker, A. D., Jr., Taviani, M., Elliot, M., Marenssi, S., Nakamura, K., Ramirez, P., and Roy, K. (2013) The influence of temperature and seawater carbonate saturation state on C-13-O-18 bond ordering in bivalve mollusks. *Biogeosciences* **10**, 4591-4606.

Ehlers, T. A. and Poulsen, C. J. (2009) Influence of Andean uplift on climate and paleoaltimetry estimates. *Earth Planet. Sci. Lett.* **281**, 238-248.

Eiler, J. M. (2011) Paleoclimate reconstruction using carbonate clumped isotope thermometry. *Quaternary Science Reviews* **30**, 3575-3588.

Ekart, D. D., Cerling, T. E., Montanez, I. P., and Tabor, N. J. (1999) A 400 million year carbon isotope record of pedogenic carbonate: Implications for paleoatmospheric carbon dioxide. *American Journal of Science* **299**, 805-827.

ESRL-PSD (2014) NCEP North American Regional Reanalysis (NARR), Boulder, CO. http://www.esrl.noaa.gov/psd/data/gridded/data.narr.html. Accessed December 2014.

Fan, M., Hough, B. G., and Passey, B. H. (2014) Middle to late Cenozoic cooling and high topography in the central Rocky Mountains: Constraints from clumped isotope geochemistry. *Earth Planet. Sci. Lett.* **408**, 35-47.

Fiorella, R. P., Poulsen, C. J., Pillco Zola, R. S., Jeffery, M. L., and Ehlers, T. A. (2015) Modern and long-term evaporation of central Andes surface waters suggests paleo archives underestimate Neogene elevations. *Earth Planet. Sci. Lett.* **432**, 59-72.

Fox, D. L. and Koch, P. L. (2003) Tertiary history of C-4 biomass in the Great Plains, USA. *Geology* **31**, 809-812.

Fox, D. L. and Koch, P. L. (2004) Carbon and oxygen isotopic variability in Neogene paleosol carbonates: constraints on the evolution of the C-4-grasslands of the Great Plains, USA. *Paleogeogr. Paleoclimatol. Paleoecol.* **207**, 305-329.

Friedman, I. and O'Neil, J. R. (1977) Compilation of stable isotope fractionation factors of geochemical interest. In: Fleischer, M. (Ed.), *Data of Geochemistry*. USGS.

Garzione, C. N., Auerbach, D. J., Smith, J. J.-S., Rosario, J. J., Passey, B. H., Jordan, T. E., and Eiler, J. M. (2014) Clumped isotope evidence for diachronous surface cooling of the Altiplano and pulsed surface uplift of the Central Andes. *Earth Planet. Sci. Lett.* **393**, 173-181.

Garzione, C. N., Dettman, D. L., Quade, J., DeCelles, P. G., and Butler, R. F. (2000) High times on the Tibetan Plateau: Paleoelevation of the Thakkhola graben, Nepal. *Geology* **28**, 339-342.

Ghosh, P., Adkins, J., Affek, H., Balta, B., Guo, W. F., Schauble, E. A., Schrag, D., and Eller, J. M. (2006a) ^{13}C-^{18}O bonds in carbonate minerals: A new kind of paleothermometer. *Geochimica Et Cosmochimica Acta* **70**, 1439-1456.

Ghosh, P., Eiler, J., Campana, S. E., and Feeney, R. F. (2007) Calibration of the carbonate 'clumped isotope' paleothermometer for otoliths. *Geochimica Et Cosmochimica Acta* **71**, 2736-2744.

Ghosh, P., Garzione, C. N., and Eiler, J. M. (2006b) Rapid uplift of the Altiplano revealed through C-13-O-18 bonds in paleosol carbonates. *Science* **311**, 511-515.

Gile, L. H., Peterson, F. F., and Grossman, R. B. (1966) Morphological and genetic sequences of carbonate accumulation in desert soils. *Soil Science* **101**, 347-360.

Grauel, A.-L., Schmid, T.W., Hu, B., Bergami, C., Capotondi, L., Zhou, L., and Bernasconi, S.M., 2013. Calibration and application of the 'clumped isotope' thermometer to foraminifera for high-resolution climate reconstructions. *Geochimica Et Cosmochimica Acta* **108**, 125-140.

Henkes, G. A., Passey, B. H., Wanamaker, A. D., Jr., Grossman, E. L., Ambrose, W. G., Jr., and Carroll, M. L. (2013) Carbonate clumped isotope compositions of modern marine mollusk and brachiopod shells. *Geochimica Et Cosmochimica Acta* **106**, 307-325.

Hillel, D. (1980) *Fundamentals of soil physics*. Academic Press, New York.

Hough, B. G., Fan, M., and Passey, B. H. (2014) Calibration of the clumped isotope geothermometer in soil carbonate in Wyoming and Nebraska, USA: Implications for paleoelevation and paleoclimate reconstruction. *Earth Planet. Sci. Lett.* **391**, 110-120.

Hren, M. T., Sheldon, N. D., Grimes, S. T., Collinson, M. E., Hooker, J. J., Bugler, M., and Lohmann, K. C. (2013) Terrestrial cooling in Northern Europe during the Eocene-Oligocene transition. *Proceedings of the National Academy of Sciences of the United States of America* **110**, 7562-7567.

Huntington, K. W., Eiler, J. M., Affek, H. P., Guo, W., Bonifacie, M., Yeung, L. Y., Thiagarajan, N., Passey, B., Tripati, A., Daeron, M., and Came, R. (2009) Methods and limitations of 'clumped' CO(2) isotope (Delta(47)) analysis by gas-source isotope ratio mass spectrometry. *Journal of Mass Spectrometry* **44**, 1318-1329.

Huntington, K. W., Saylor, J., Quade, J., and Hudson, A. M. (2015) High late Miocene-Pliocene elevation of the Zhada Basin, southwestern Tibetan Plateau, from carbonate clumped isotope thermometry. *Geol. Soc. Am. Bull.* **127**, 181-199.

Huxman, T. E., Snyder, K. A., Tissue, D., Leffler, A. J., Ogle, K., Pockman, W. T., Sandquist, D. R., Potts, D. L., and Schwinning, S. (2004) Precipitation pulses and carbon fluxes in semiarid and arid ecosystems. *Oecologia* **141**, 254-268.

Hyland, E. G., Sheldon, N. D., Van der Voo, R., Badgley, C., and Abrajevitch, A. (2015) A new paleoprecipitation proxy based on soil magnetic properties: Implications for expanding paleoclimate reconstructions. *Geol. Soc. Am. Bull.*

Knight, W. G. (1991) Chemistry of arid region soils. In: Skujiņš, J. (Ed.),*Semiarid lands and deserts*. Marcel Dekker, New York.

Lechler, A. R., Niemi, N. A., Hren, M. T., and Lohmann, K. C. (2013) Paleoelevation estimates for the northern and central proto-Basin and Range from carbonate clumped isotope thermometry. *Tectonics* **32**, 295-316.

Leier, A., McQuarrie, N., Garzione, C., and Eiler, J. (2013) Stable isotope evidence for multiple pulses of rapid surface uplift in the Central Andes, Bolivia. *Earth Planet. Sci. Lett.* **371**, 49-58.

Levin, N. E., Quade, J., Simpson, S. W., Semaw, S., and Rogers, M. (2004) Isotopic evidence for Plio-Pleistocene environmental change at Gona, Ethiopia. *Earth Planet. Sci. Lett.* **219**, 93-110.

Lhomme, J. P. (1997) Towards a rational definition of potential evaporation. *Hydrology and Earth System Sciences* **1**, 257-264.

Liu, X. Z., Wan, S. Q., Su, B., Hui, D. F., and Luo, Y. Q. (2002) Response of soil CO2 efflux to water manipulation in a tallgrass prairie ecosystem. *Plant and Soil* **240**, 213-223.

Luo, Y. and Zhou, X. (2006) *Soil respiration and the environment*. Academic Press, Burlington.

Machette, M. N. (1985) Calcic soils of the southwestern United States. In: Weide, D. L. (Ed.),*Geological Society of America Special Paper 203*.

Mathieu, R. and Bariac, T. (1996) An isotopic study (H-2 and O-18) of water movements in clayey soils under a semiarid climate. *Water Resources Research* **32**, 779-789.

Mesinger, F., DiMego, G., Kalnay, E., Mitchell, K., Shafran, P. C., Ebisuzaki, W., Jovic, D., Woollen, J., Rogers, E., Berbery, E. H., Ek, M. B., Fan, Y., Grumbine, R., Higgins, W., Li, H., Lin, Y., Manikin, G., Parrish, D., and Shi, W. (2006) North American regional reanalysis. *Bulletin of the American Meteorological Society* **87**, 343-+.

Meyer, N. A., Breecker, D. O., Young, M. H., and Litvak, M. E. (2014) Simulating the Effect of Vegetation in Formation of Pedogenic Carbonate. *Soil Sci. Soc. Am. J.* **78**, 914-924.

Montanez, I. P. (2013) Modern soil system constraints on reconstructing deep-time atmospheric CO2. *Geochimica Et Cosmochimica Acta* **101**, 57-75.

Monteith, J. L. (1981) Evapotranspiration and surface temperature. *Quarterly Journal of the Royal Meteorological Society* **107**, 1-27.

NCDC (2012) 1981-2010 U.S. Climate Normals. http://www.ncdc.noaa.gov/data-access/land-based-station-data/land-based-datasets/climate-normals/1981-2010-normals-data. Accessed December 2014.

Nordt, L. C. and Driese, S. D. (2010) New weathering index improves paleorainfall estimates from Vertisols. *Geology* **38**, 407-410.

Noy-Meir, I. (1973) Desert ecosystems: environment and producers. *Annual Review of Ecology and Systematics* **4**, 25-51.

NRCS (2016) Soil Climate Analysis Network. http://www.wcc.nrcs.usda.gov/scan/. Accessed Jan 15, 2016.

Ode, D. J., Tieszen, L. L., and Lerman, J. C. (1980) The seasonal contribution of C_3 and C_4 plant species to primary production in a mixed prairie. *Ecology* **61**, 1304-1311.

Passey, B. H., Levin, N. E., Cerling, T. E., Brown, F. H., and Eiler, J. M. (2010) High-temperature environments of human evolution in East Africa based on bond ordering in paleosol carbonates. *Proceedings of the National Academy of Sciences of the United States of America* **107**, 11245-11249.

Peters, N. A., Huntington, K. W., and Hoke, G. D. (2013) Hot or not? Impact of seasonally variable soil carbonate formation on paleotemperature and O-isotope records from clumped isotope thermometry. *Earth Planet. Sci. Lett.* **361**, 208-218.

Petersen, S.V., Winkelstern, I.Z., Lohmann, K.C., and Meyer, K.W., 2016. The effects of Porapak (TM) trap temperature on delta O-18, delta C-13, and Delta(47) values in preparing samples for clumped isotope analysis. *Rapid Communications in Mass Spectrometry* **30**, 199-208.

Petrizzo, D.A., Young, E.D., and Runnegar, B.N., 2014. Implications of high-precision measurements of C-13-O-18 bond ordering in CO2 for thermometry in modern bivalved mollusc shells. *Geochimica Et Cosmochimica Acta* **142**, 400-410.

Prism Climate Group, O. S. U. (2015) 30-Year Normals: precipitation at 4km resolution, 1980-2010. http://www.prism.oregonstate.edu/normals/. Accessed January 2015.

Quade, J., Breecker, D. O., Daeron, M., and Eiler, J. (2011) The paleoaltimetry of tibet: An isotopic perspective. *American Journal of Science* **311**, 77-115.

Quade, J. and Cerling, T. E. (1995) Expansion of C_4 grasses in the Late Miocene of Northern Pakistan: evidence from stable isotopes in paleosols. *Paleogeogr. Paleoclimatol. Paleoecol.* **115**, 91-116.

Quade, J., Eiler, J., Daeron, M., and Achyuthan, H. (2013) The clumped isotope geothermometer in soil and paleosol carbonate. *Geochimica Et Cosmochimica Acta* **105**, 92-107.

Quade, J., Garzione, C., and Eiler, J. (2007) Paleoelevation reconstruction using pedogenic carbonates. *Paleoaltimetry: Geochemical and Thermodynamic Approaches* **66**, 53-87.

Retallack, G. J. (1994) The environmental factor appraoch to the interpretation of paleosols. In: Amundson, R., Harden, J., and Singer, M. Eds.), *Factors of Soil Formation: A Fiftieth Anniversary Retrospective*. Soil Science Society of America Special Publication.

Retallack, G. J. (2005) Pedogenic carbonate proxies for amount and seasonality of precipitation in paleosols. *Geology* **33**, 333-336.

Reynolds, J. F., Kemp, P. R., Ogle, K., and Fernandez, R. J. (2004) Modifying the 'pulse-reserve' paradigm for deserts of North America: precipitation pulses, soil water, and plant responses. *Oecologia* **141**, 194-210.

Ringham, M. C., Hoke, G. D., Huntington, K. W., and Aranibar, J. N. (2016) Influence of vegetation type and site-to-site variability on soil carbonate clumped isotope records, Andean piedmont of Central Argentina (32-34°S). *Earth Planet. Sci. Lett.* **440**, 1-11.

Royer, D. L. (1999) Depth to pedogenic carbonate horizon as a paleoprecipitation indicator? *Geology* **27**, 1123-1126.

Schenk, H. J. and Jackson, R. B. (2002) Rooting depths, lateral root spreads and below-ground/above-ground allometries of plants in water-limited ecosystems. *Journal of Ecology* **90**, 480-494.

Seyfried, M. S., Grant, L. E., Du, E., and Humes, K. (2005) Dielectric loss and calibration of the Hydra Probe soil water sensor. *Vadose Zone Journal*, 1070-1079.

Sheldon, N. D., Retallack, G. J., and Tanaka, S. (2002) Geochemical climofunctions from North American soils and application to paleosols across the Eocene-Oligocene boundary in Oregon. *J. Geol.* **110**, 687-696.

Sheldon, N. D., Tabor, N. J., 2009. Quantitative paleoenvironmental and paleoclimatic reconstruction using paleosols. *Earth-Science Reviews* **95**, 1-52.

Shukla, M. K. (2014) *Soil Physics: An Introduction*. CRC Press, Boca Raton, FL.

Snell, K. E., Thrasher, B. L., Eiler, J. M., Koch, P. L., Sloan, L. C., and Tabor, N. J. (2013) Hot summers in the Bighorn Basin during the early Paleogene. *Geology* **41**, 55-58.

Soil Survey Staff (2014) *Keys to Soil Taxonomy*. USDA-Natural Resources Conservation Service, Washington, DC.

Strömberg, C. A. E. and McInerney, F. A. (2011) The Neogene transition from C-3 to C-4 grasslands in North America: assemblage analysis of fossil phytoliths. *Paleobiology* **37**, 50-71.

Swart, P. K., Burns, S. J., and Leder, J. J. (1991) Fractionation of the stable isotopes of oxygen and carbon in carbon-dioxide during the reaction of calcite with phosphoric-acid as a function of temperature and technique. *Chem. Geol.* **86**, 89-96.

Tabor, N. J., Myers, T. S., Gulbranson, E., Rasmussen, C., and Sheldon, N. D. (2013) Carbon stable isotope composition of modern calcareous soil profiles in California: implications for CO_2 reconstructions from calcareous paleosols. In: Driese, S. G. and Nordt, L. C. Eds.), *New Frontiers in Paleopedology and Terrestrial Paleoclimatology: Paleosols and Soil Surface Analog Systems*.

Tang, J., Dietzel, M., Fernandez, A., Tripati, A. K., and Rosenheim, B. E. (2014) Evaluation of kinetic effects on clumped isotope fractionation (Delta(47)) during inorganic calcite precipitation. *Geochimica Et Cosmochimica Acta* **134**, 120-136.

Thiagarajan, N., Adkins, J., and Eiler, J. (2011) Carbonate clumped isotope thermometry of deep-sea corals and implications for vital effects. *Geochimica Et Cosmochimica Acta* **75**, 4416-4425.

Tripati, A. K., Eagle, R. A., Thiagarajan, N., Gagnon, A. C., Bauch, H., Halloran, P. R., and Eiler, J. M. (2010) ^{13}C-^{18}O isotope signatures and 'clumped isotope' thermometry in foraminifera and coccoliths. *Geochimica Et Cosmochimica Acta* **74**, 5697-5717.

VanDeVelde, J. H., Bowen, G. J., Passey, B. H., and Bowen, B. B. (2013) Climatic and diagenetic signals in the stable isotope geochemistry of dolomitic paleosols spanning the Paleocene-Eocene boundary. *Geochimica Et Cosmochimica Acta* **109**, 254-267.

Wacker, U., Fiebig, J., Toedter, J., Schoene, B.R., Bahr, A., Friedrich, O., Tuetken, T., Gischler, E., and Joachimski, M.M., 2014. Empirical calibration of the clumped isotope paleothermometer using calcites of various origins. *Geochimica Et Cosmochimica Acta* **141**, 127-144.

Wanner, H., Beer, J., Buetikofer, J., Crowley, T.J., Cubasch, U., Flueckiger, J., Goosse, H., Grosjean, M., Joos, F., Kaplan, J.O., Kuettel, M., Mueller, S.A., Prentice, I.C., Solomina, O., Stocker, T.F., Tarasov, P., Wagner, M., and Widmann, M., 2008. Mid- to Late Holocene climate change: an overview. *Quaternary Science Reviews* **27**, 1791-1828.

Zaarur, S., Affek, H. P., and Brandon, M. T. (2013) A revised calibration of the clumped isotope thermometer. *Earth Planet. Sci. Lett.* **382**, 47-57.

CHAPTER 3

The effect of seasonally fluctuating soil environments on temperature reconstructions from paleosols

3.0 Abstract

Accurate reconstructions of surface air temperatures from paleosols depend on understanding the processes that cause the soil environment to deviate from the surface climate. A number of proxies have been developed that use the geochemistry of soil minerals to reconstruct surface climate. In order to constrain the temperature biases likely to be recorded by paleosol proxies better, soil moisture and temperature data are compiled from 218 modern soils within the Soil Climate Analysis Network. These data are compared to mean annual air temperature as well as to seasonal air temperature fluctuations in order to quantify the biases between the two datasets. Reduced temperature seasonality in soils occurs at sites where cold season air temperatures fall below freezing, with minimum monthly temperature corresponding to the scale of the reduction in soil temperature seasonality. This phenomenon produces mean annual and warm season soil temperatures warmer than the corresponding air temperature values, with mean annual soil temperatures (MAST) being more severely affected. When considering all of the SCAN sites, the average offset between MAST and mean annual air temperature is +1.9 °C. We also assess temperature biases that are likely to be recorded by pedogenic carbonate. Given that pedogenic carbonate likely forms seasonally during periods of

declining soil moisture content, pedogenic carbonate is more likely to record a temperature that is biased warm relative to mean annual air temperature. If the largest 30-day decline in soil moisture accurately predicts the seasonal timing of pedogenic carbonate formation, >75% of the sites would record a warm bias relative to MAAT, with an average bias of about +4 °C. Additionally, temperatures recorded in pedogenic carbonate greater than 12−14 °C above MAAT are considered unlikely at depths > 50 cm. Many soils are also characterized by distinct seasonal soil moisture fluctuations at different depths, suggesting that the depth at which pedogenic carbonate formed in soils may record substantially different temperatures biases. Therefore, careful characterization of whole paleosol profiles and of post-burial processes (e.g., compaction) need to be taken into account when using clumped isotope measurements of pedogenic carbonates to reconstruct paleoclimatic or paleoenvironmental conditions.

3.1 Introduction

Because climate plays a primary role in shaping the physical and chemical development of soils (Jenny, 1941), the geochemistry of paleosols can be used to reconstruct climate variables in the geologic past (Sheldon and Tabor, 2009). Accurate reconstructions of air temperature are required to address questions surrounding climate sensitivity and the evolution of the Earth's climate system. Temperature records are also important for a broad range of geologic applications, including regional paleoelevation reconstructions required to test hypotheses of continental tectonics (Clark, 2007). Proxies developed for reconstructing temperature from paleosols include "pedo-transfer functions," which relate the degree of chemical weathering, as reflected by the bulk elemental geochemistry of paleosols, to mean annual air temperature (MAAT; Sheldon et al., 2002; Gallagher and Sheldon, 2013). Other approaches for

reconstructing temperatures are based on the stable isotopic geochemistry of particular minerals that formed in-situ in paleosols, including carbonate (Dworkin et al., 2005), clay minerals (Delgado and Reyes, 1996; Tabor and Montañez, 2005), as well as iron oxides and hydroxides (Yapp, 1987; Yapp, 2000; Tabor and Yapp, 2005).

These paleosol temperature proxies depend on certain assumptions, including uncertainty about the formation time of individual paleosols, potential evaporative enrichment of ^{18}O in soil water (Tabor et al., 2013), or the stability of the meteoric water line in the geologic past (Sheldon and Tabor, 2009). Unlike previous approaches, the advent of clumped isotope thermometry allows for the direct assessment of temperature in carbonate-bearing paleosols, because the abundance of doubly substituted rare isotopes in carbonate minerals is controlled only by formation temperature (Ghosh et al., 2006; Eiler, 2011). Although the clumped isotope composition of pedogenic carbonate provides a direct measurement of temperature, uncertainties exist about the potential for a bias imparted by seasonal timing of carbonate formation. The traditional assumption held that pedogenic carbonate formed during mean growing season conditions, and therefore would reflect the climate of the growing season (Cerling and Quade, 1993). However, it was subsequently demonstrated that carbonate can form in soils during particularly dry and hot periods that differ significantly from the mean growing season (Breecker et al., 2009).

The earliest clumped isotope analyses of pedogenic carbonate from modern soils in East Africa produced temperatures that were generally reflective of warm season air temperatures (Passey et al., 2010). A warm season temperature bias was further documented by clumped isotope studies of modern soils in North America, Asia, and South America (Quade et al., 2013; Hough et al., 2014; Ringham et al., 2016). However, a warm season formation bias cannot be

universally assumed for pedogenic carbonate. Studies of pedogenic carbonate along elevation transects in the Andes documented warm-season temperatures at lower elevation sites that receive the bulk of precipitation during the summer, whereas higher elevation sites that receive the bulk of precipitation during the winter months produced temperatures close to MAAT (Peters et al., 2013; Burgener et al., 2016). Clumped isotope temperatures close to MAAT were also recorded at sites from the southwestern United States, where model results predict that the soils tend to dry out in the late winter to early spring (Gallagher and Sheldon, 2016).

Accurate temperature reconstructions from paleosols depend on a thorough understanding of how the soil environment relates to surface climate variables. To address this need, we compiled instrumental soil temperature and moisture data from the Soil Climate Analysis Network (SCAN) and compared it to surface climate normals. Seasonal temperature variations are evaluated across multiple soil depths and compared to normal air temperature fluctuations in order to quantify systematic differences and the prevalence of a warm soil temperature bias relative to MAAT. Seasonal fluctuations in soil moisture data are also assessed to determine points of the year during which pedogenic carbonate formation is likely favored. Finally, soil temperatures during these periods of soil water depletion are compared to MAAT in order to determine the magnitude of the offset between the temperature presumably recorded by pedogenic carbonate and MAAT.

3.2 Factors affecting soil temperature and pedogenic carbonate formation

Fluctuations in soil temperature are primarily controlled by changes in radiant, thermal, and latent energy exchange at the soil surface, which are then propagated down into the soil via conduction (Hillel, 1980). Conduction of heat in a soil depends on both the volumetric heat

capacity and thermal conductivity of the soil, which vary depending on the density and physical composition of the soil. For example, the organic content of a soil can alter its thermal properties because organic matter tends to have a higher heat capacity and lower thermal conductivity than most minerals (Hillel, 1980). It is also important to note that the depth to which surface soil temperature fluctuations will be propagated into a soil is not only a function of the physical properties of a soil, but also the frequency of the temperature fluctuation. A temperature fluctuation with a longer duration will be propagated deeper into the soil, which explains why diurnal temperature fluctuations tend to be largely damped out by 50 cm (Buol et al., 2012), whereas seasonal temperatures fluctuations are propagated many meters down into a soil.

Although the seasonal temperature fluctuation of the soil surface generally tracks air temperature fluctuations, it is important to note that other factors can cause significant deviations from this pattern. In areas where there is limited vegetative cover, the soil surface is exposed directly to solar radiation, which allows soil surface temperature to exceed air temperature. During the winter, persistent snow cover can allow the soil surface to remain warmer than air temperatures by providing insulation. In contrast to these processes, high levels of soil water content in the soil can have a cooling effect of soil surface by raising the total heat capacity of the soil and increasing the thermal conductivity of the soil (Hillel, 1980). Evaporative loss of water from the soil will also have a net cooling effect on the soil (Hillel, 1980).

Because seasonal temperature fluctuations are propagated deep into soils, the exact timing of pedogenic carbonate formation during the year could significantly affect the temperature recorded within the carbonate. The relative impact of the various environmental factors that control the seasonal timing of pedogenic carbonate formation remains uncertain. Understanding the formation of pedogenic carbonate is further complicated because it does not

necessarily form every year, and in some settings it may only form in response to shorter-term anomalous weather events (e.g. droughts; Hough et al., 2014). With all other factors being equal, formation during warmer periods is thought to be more likely because carbonate saturation is favored at higher temperatures (Breecker et al., 2009; Cotton et al., 2013). This interpretation is supported by the predominance of warm-season temperatures produced by clumped isotope studies of pedogenic carbonate (e.g., Passey et al., 2010; Quade et al., 2013; Hough et al., 2014). Furthermore, kinetic limitations begin to preclude carbonate formation under equilibrium conditions when temperatures approach freezing, as evidenced by anomalously warm clumped isotope temperatures from a high elevation site in the Andes (Burgener et al., 2016).

Seasonal fluctuations in soil moisture content may supersede temperature as a primary control on pedogenic carbonate formation in water-limited environments (Hough et al., 2014; Gallagher and Sheldon, 2016; Burgener et al., 2016). Carbonate formation could be favored during drier periods, because the activity of Ca^{2+} increases as soils dry out and soil pCO_2 will decrease as soil respiration rates slow (Cotton et al., 2013). If the timing of soil water depletion occurs during a cooler part of the year, it explains clumped isotope results that record temperatures at or below MAT (Gallagher and Sheldon, 2016; Burgener et al., 2016). It is important to note that relating soil moisture fluctuations to surface climate variables is not straightforward. In addition to precipitation and evapotranspiration, soil moisture is affected by physical properties of soils, such as texture and drainage, which control the infiltration and retention of water (Noy-Meir, 1973; Tabor et al., 2013).

The composition and density of overlying vegetation can also affect absolute soil temperatures and soil moisture fluctuations, thereby influencing pedogenic carbonate formation. As stated above, reduced vegetative cover can allow soil temperatures to exceed overlying air

temperatures. This phenomenon, known as ground heating, has been invoked to explain elevated clumped isotope temperatures recorded in pedogenic carbonate in sparsely vegetated environments (Quade et al., 2013). Different plants also have various rooting depths and growth strategies, which can affect the timing of soil water depletion and, therefore, also the timing of pedogenic carbonate formation. Modeling results have suggested that calcite may form at hotter temperatures when overlain by C_4 vegetation rather than C_3 plants (Meyer et al., 2014). However, pedogenic carbonate clumped isotope results from two nearby sites in central Argentina overlain by C_3 and C_4 vegetation, respectively, produced similar temperatures (Ringham et al., 2016).

3.3 Methods

Instrumental soil temperature and moisture data were compiled from 218 sites within the Soil Climate Analysis Network (SCAN) located across the contiguous United States, Alaska, Hawaii, Puerto Rico and the US Virgin Islands (NRCS, 2015). Because the goal of this study is to investigate regular seasonal variations in soil temperature and moisture, an average daily value was calculated for each calendar day during the year (1−365). The soil data measured at midnight each day were averaged with the corresponding days from every year, beginning when soil data became available through the end of 2015. Soil temperature data were only examined for 51 and 102 cm depth because diurnal temperature fluctuations are largely damped out below 30 cm (Hillel, 1980).

It should be noted that not all of the SCAN sites had sensors installed at the depths of interest (51 and 102 cm for soil temperature; 20, 51, and 102 cm for soil moisture). Additionally, records from particular sites or specific depths within a site were excluded if there were any

calendar days for which no data existed during the entire study interval. Clearly erroneous sensor data was removed ahead before computing daily averages. Depths excluded for missing or erroneous data are detailed in Appendix 1 along with specific data that was manually removed.

Surface climate data (temperature and precipitation) was taken from the 1981–2010 US Climate Normal dataset (Arguez et al., 2012; NCDC, 2012). For each SCAN site, climate data from the closest normal station was used except in situations where the elevation difference between the SCAN station and normal station was greater than ± 250 m. If no climate stations existed within 75 km of the particular SCAN site that met these criteria, then that SCAN site was excluded (14 sites).

3.4 Results and Discussion

3.4.1 Soil temperature seasonality

As stated above, surface soil temperatures are able to exceed air temperatures in situations where the soil surface is directly exposed to solar radiation. This phenomenon is likely of greater importance in areas where there is a low density of vegetation, such as arid ecosystems. This phenomenon raises the possibility that the total amplitude of seasonal soil temperature variation can exceed that of the air. To evaluate how the seasonal amplitudes of air and soil temperature compare, the difference between the maximum and minimum monthly temperatures for each site are plotted in Fig. 3.1. It is important to note that the amplitude of seasonal soil temperature variation cannot be directly compared to seasonal air temperature variation, because the oscillation will be damped with depth in the soil.

The extent to which seasonal temperature fluctuations will be damped at depth can be estimated using the following equation from Hillel (1980):

$$T(z,t) = T_{avg} + \frac{A_0\left[\sin\left(\omega t - \frac{z}{d}\right)\right]}{e^{z/d}} \quad (1)$$

where T_{avg} is the average annual temperature, A_0 is the amplitude of seasonal surface temperature fluctuation, ω is the radial frequency (2π/365), z is the depth in the soil, and d is the damping depth. The damping depth is a function of the physical properties of the soil and can be calculated using the equation:

$$d = \sqrt{\frac{2\kappa}{C_v \omega}} \quad (2)$$

where κ is the thermal conductivity and C_v is the volumetric heat capacity. Using values of 1.09 ($w°K^{-1}m^{-1}$) for κ and 1.98 ($J°K^{-1}m^{-3}$) for C_v (Shukla, 2014), the amplitude of seasonal temperature variation at 51 and 102 cm would be approximately 81% and 65% of the surface temperature variation, respectively.

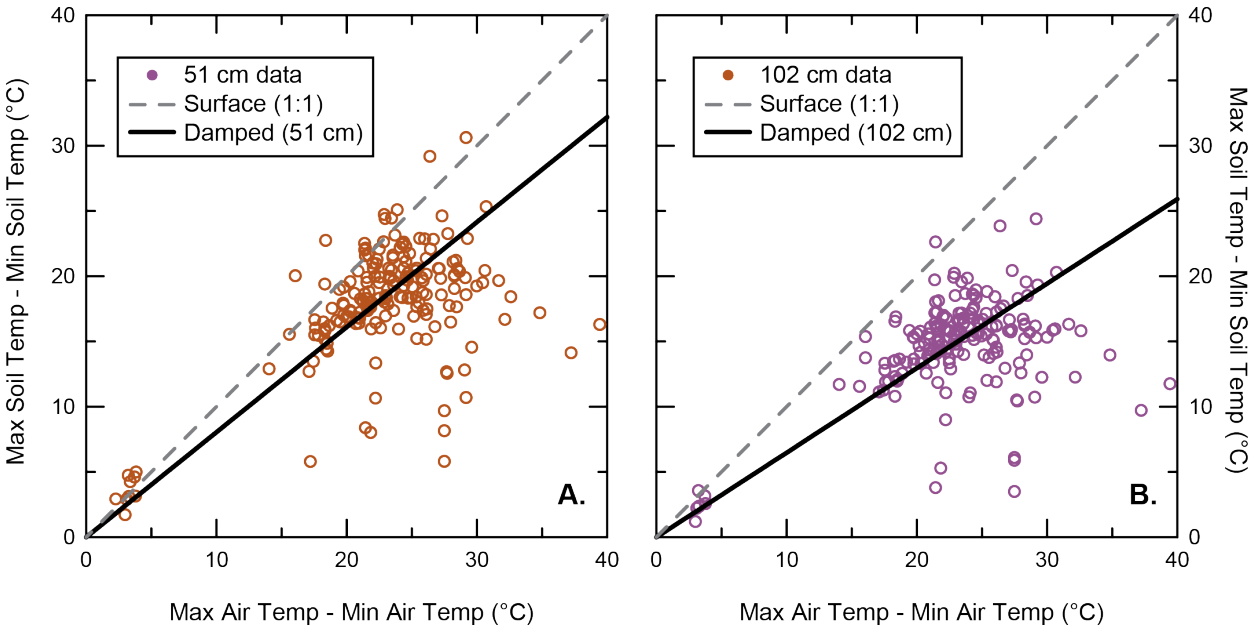

Figure 3.1

Air temperature seasonality compared to soil temperature seasonality at depths of (A) 51 cm and (B) 102 cm. Minimum monthly average soil and air temperatures were subtracted from maximum monthly average temperature values. The gray dashed line line is a 1:1 line. The black solid line is the damped seasonality estimated at depth in the soil.

At 51 and 102 cm depth in the soil, the seasonal soil temperature variation falls at or above the damped surface air temperature at 59 and 62% of the sites, respectively (Fig. 3.1). The sites where the amplitude of seasonal soil temperature variation exceeds that of the air can be explained, at least in part, by excess ground heating. It is important to note that ground heating will only affect the amplitude of seasonal temperature fluctuations at sites with sizable seasonal variations in solar radiation (e.g. greater in the summer, lower in the winter).

The sites where temperature seasonality is reduced in the soil as compared to the calculated damped air temperature seasonality require a different explanation. Sites at which the average air temperature during the coldest month falls below -2 °C exhibit a moderately strong relationship between that month's air temperature and the extent to which the soil temperature variation falls below values predicted by the damped air temperature variation (Fig. 3.2). Put another way, colder air temperatures during the coldest month correspond to a greater reduction in soil temperature seasonality. The reduction in soil temperature amplitude is likely due to a combination of factors associated with freezing temperatures. Consistent snowpack will insulate

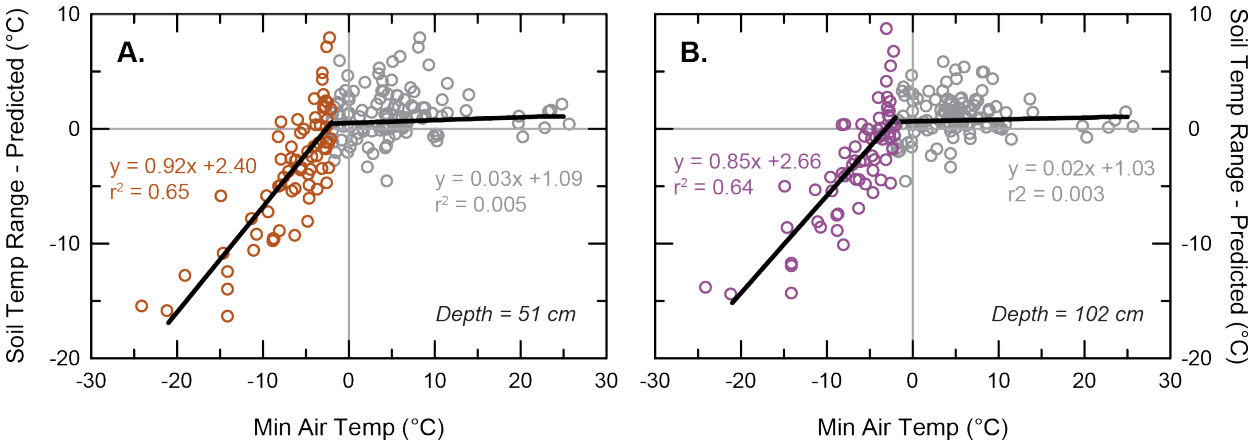

Figure 3.2

Minimum monthly air temperatures compared to the difference between the observed range in monthly seasonal soil temperatures and the damped estimate of temperature range derived from monthly air temperature seasonality.

the soil surface, preventing the soil from reaching temperatures as cold as the overlying air (Smith et al., 1964; Decker et al., 2003). Latent heat transfer associated with the freezing and thawing of H_2O in the soil may also diminish the overall temperature change observed in the soils by consuming energy that would otherwise result in a temperature change (Hillel, 1980). Soils where the coldest monthly average temperature is warmer than -2 °C do not exhibit any correlation with the deviation in soil seasonality (Fig. 3.2).

A reduction in the amplitude of seasonal temperature variations restricts the maximum amount that both cold and warm season soil temperatures can deviate from mean annual soil temperature (MAST). In colder settings such as described above, where cold month soil surface temperatures are warmer than air temperature and the warm month soil surface temperature is similar to or greater than air temperature, MAST will be warmer than MAAT. Based on the relationship identified in Fig. 3.2, where the amplitude of seasonal soil temperature decreases as cold month air temperatures fall further below -2 °C, the difference between MAST and MAAT would be expected to increase at colder sites.

Although insulating the soil against cold air temperatures alone will increase both MAST and warm season soil temperatures at depth, MAST will shift by a greater amount. Therefore, this phenomenon would likely have a greater effect on paleosol proxies that reconstruct MAST, as opposed to those that record warm season temperatures, such as pedogenic carbonate. These processes are also most likely to be a complicating factor in continental settings at high latitudes or at high elevations. This bias is likely to be of greater importance during cooler periods of Earth's history, as opposed to greenhouse periods such as the Cretaceous. We would also expect this bias to be less pronounced in regions of extreme water limitation. Well-drained soils will typically be dry in arid settings, which means that less energy will be consumed during phase

changes associated with the freezing and thawing of H_2O (Hillel, 1980). Additionally in settings without significant winter precipitation, snowfall will be limited and the soil will be less insulated against cold air temperatures.

3.4.2 Mean Annual Soil Temperature vs. Mean Annual Air Temperature

Ground heating, snow insulation, and freeze-thaw are all processes that can elevate MAST relative to MAAT. It is generally estimated that MAST will be approximately 1–2 °C greater than MAAT in United States (Buol et al., 2012). A greater offset between the two variables has been observed for certain regions, such as 3−7 °C in Alaska (Smith et al., 1964) and 2.5 °C at tropical latitudes (Van Wambeke, 1985). When considering all of the SCAN sites, the average difference between MAST and MAAT is 1.9 °C, with a fairly even distribution around the mean (Fig. 3.3A-B). Pedogenic carbonate typically only forms in soils at sites where MAP is less than 75 cm (Retallack, 2005). Within only the sites that receive less than 75 cm of precipitation annually, the distribution shifts to slightly higher values with a mean difference of 2.5 °C.

The larger difference between MAST and MAAT values within more arid SCAN sites is consistent with expectations. For example, Murtha and Williams (1986) observed that in Australia MAST is elevated above MAAT by 4 °C in drier regions, as compared to 2 °C characterized by wetter soil regimes. Although a number of local factors complicate the relationship between soil moisture and precipitation, it can be assumed that sites that receive less annual precipitation will have drier soils on average. These drier soils will tend to be slightly warmer than wetter soils, in part because evaporation of soil water will have a net cooling effect on the soil.

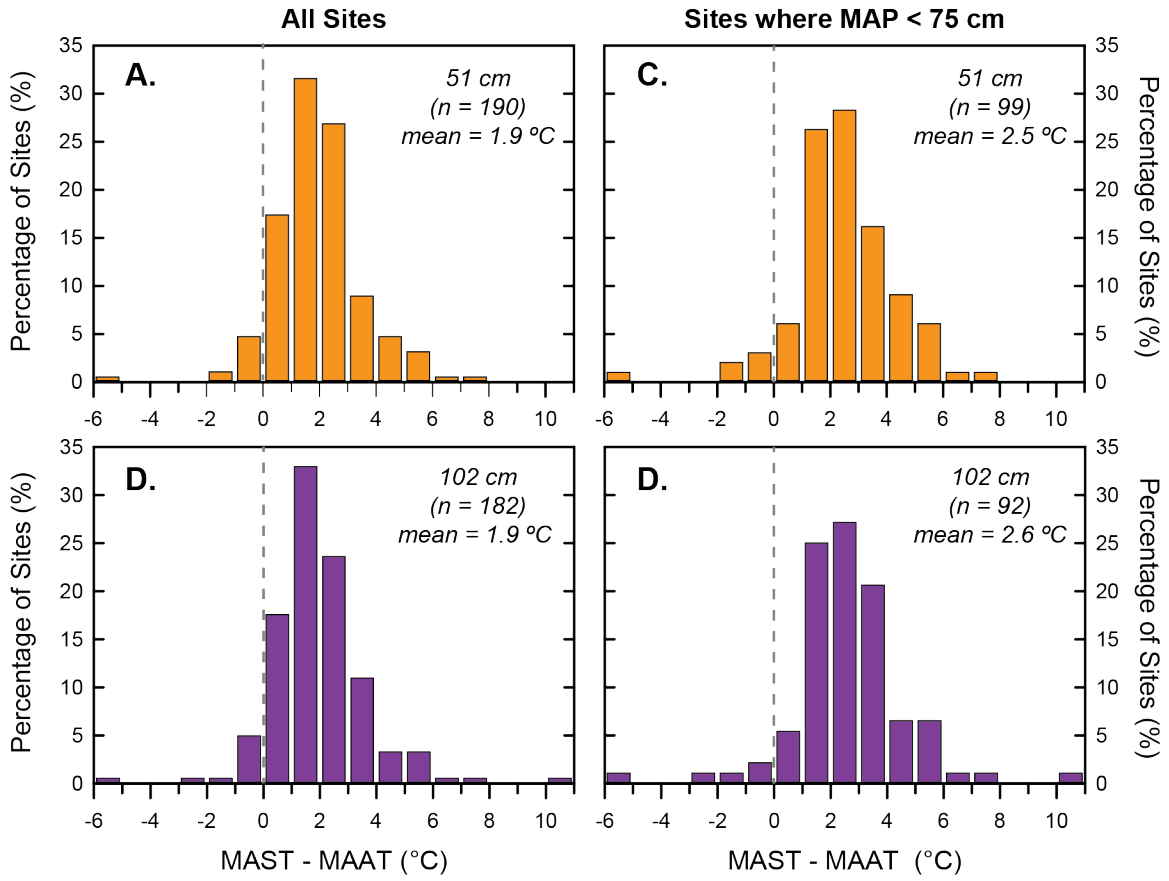

Figure 3.3

Binned site distribution of the difference between mean annual soil temperature (MAST) and mean annual air temperature (MAAT) at (A–B) all sites and (C–D) sites that receive less than 75 cm of mean annual precipitation.

Combining the SCAN data with previous studies of soil temperature, it is clear that a mean warm bias relative to MAAT can generally be assumed for soils and paleosols. However, this bias is generally less than 5 °C (Fig. 3.3). For studies that use minerals that may form in particular seasons, such as pedogenic carbonate, to reconstruct temperature from paleosols, this general tendency for reconstructed soil temperature to exceed MAAT makes a warm bias inherently more likely. Fig. 3.4 plots the percentage of sites where average soil temperature is greater than MAAT during each month. Over half of the sites that receive less than 75 cm in mean annual precipitation are characterized by at least 7 months out of the year where soil temperature exceeds MAAT.

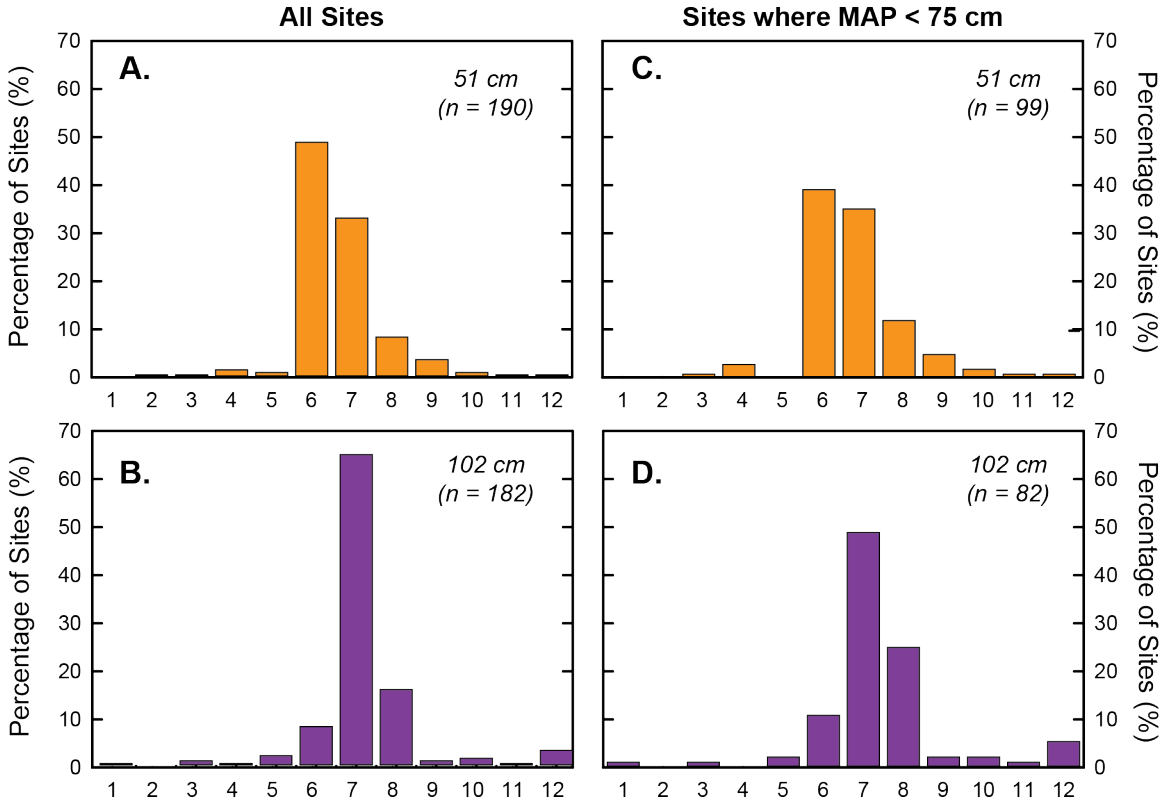

Figure 3.4 Binned site distribution of the number of months where average soil temperature (AST) is greater than mean annual air temperature (MAAT) at (A–B) all sites and (C–D) sites that receive less than 75 cm of mean annual precipitation.

3.4.3 Pedogenic carbonate formation and a warm-season temperature bias?

Pedogenic carbonate is more likely to record a warm bias relative to MAAT if the timing of pedogenic carbonate formation were completely random, because average soil temperature exceeds MAAT at the majority of sites for more than half of the year (Figs 3.4B and D). However as discussed above, pedogenic carbonate formation will be favored under certain environmental conditions, such as periods of soil water depletion. If soil water depletion is assumed to be the primary factor controlling pedogenic carbonate formation, the seasonal timing of pedogenic carbonate formation can be estimated from the instrumental soil moisture record. The soil temperature at the time of soil water depletion can then be compared to MAAT in order

to assess the temperature bias that would be recorded by pedogenic carbonate. For the purpose of this study, two different soil moisture scenarios are considered as the intervals during which soil carbonate formation is most likely to occur: (1) the 30-day period during the year when soil moisture is at its lowest value, and (2) the 30-day period during which there is the largest decline in soil moisture.

For both pedogenic carbonate formation scenarios, the temperature and moisture data from 51 and 102 cm were independently evaluated. Because pedogenic carbonate formation is restricted to more arid sites (Retallack, 2005), only sites that receive less than 75 cm annual precipitation were considered for this portion of the study. The driest period of the year was assessed by calculating the average soil moisture value for consecutive 30-day intervals, and then determining the lowest 30-day value throughout the year. An average soil temperature value during the driest 30-day window was subsequently calculated and compared to MAAT.

In order to determine the time of the year when the soils experienced the most severe decline in soil moisture, a 30 consecutive day window was used again. The average soil moisture was calculated for both the first and last 15 days of the time window, and the average soil moisture value from the last 15 days of the window was subtracted from the average value during the first 15 days. This approach was chosen in order to capture seasonal trends in soil water content more accurately, and to smooth out day to day variability. Similar to the first scenario, the average soil temperature was then calculated for the 30-day period that recorded the largest drop in soil moisture.

At both 51 and 102 cm depth, the driest 30-day period occurs most frequently during the winter months (December−February; Figs. 3.5A and 3.5B). While the seasonal timing of the driest period in the soils is broadly similar at both depths, a slight offset is observable. The driest

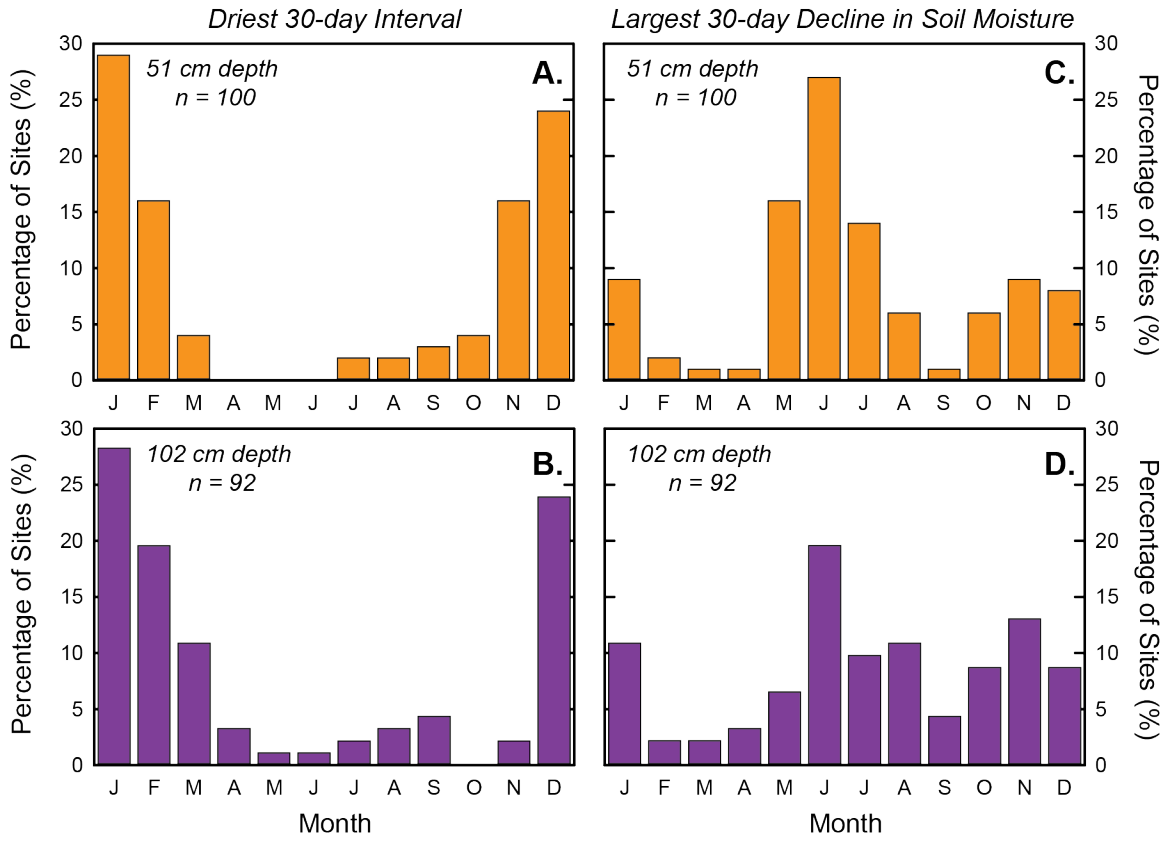

Figure 3.5

Seasonal timing of soil moisture scenarios that considered favorable for pedogenic carbonate formation: (A–B) the driest 30-day interval during the year and (C–D) the largest 30-day decline in soil moisture. Sites are placed are placed in the appropriate bin based on the midpoint of the respective 30-day window.

interval at 51 cm occurs at a number of sites in late fall, but rarely occurs during this time at 102 cm. Instead, a higher percentage of sites reach their driest point during the late winter and early spring. This difference between the distributions is a product of the driest value at 102 cm frequently occurring between one and six weeks after it is reached at 51 cm.

In contrast to a predominantly winter nadir in soil moisture, the seasonal timing of rapid soil moisture decline forms a bimodal distribution at 51 cm. The majority of the sites rapidly dry out during the late spring through summer (May through August), while a smaller number of sites undergo the most severe drop in soil moisture during the winter. The same two peaks in the distribution are visible at 102 cm, but overall the timing of rapid soil water depletion is more

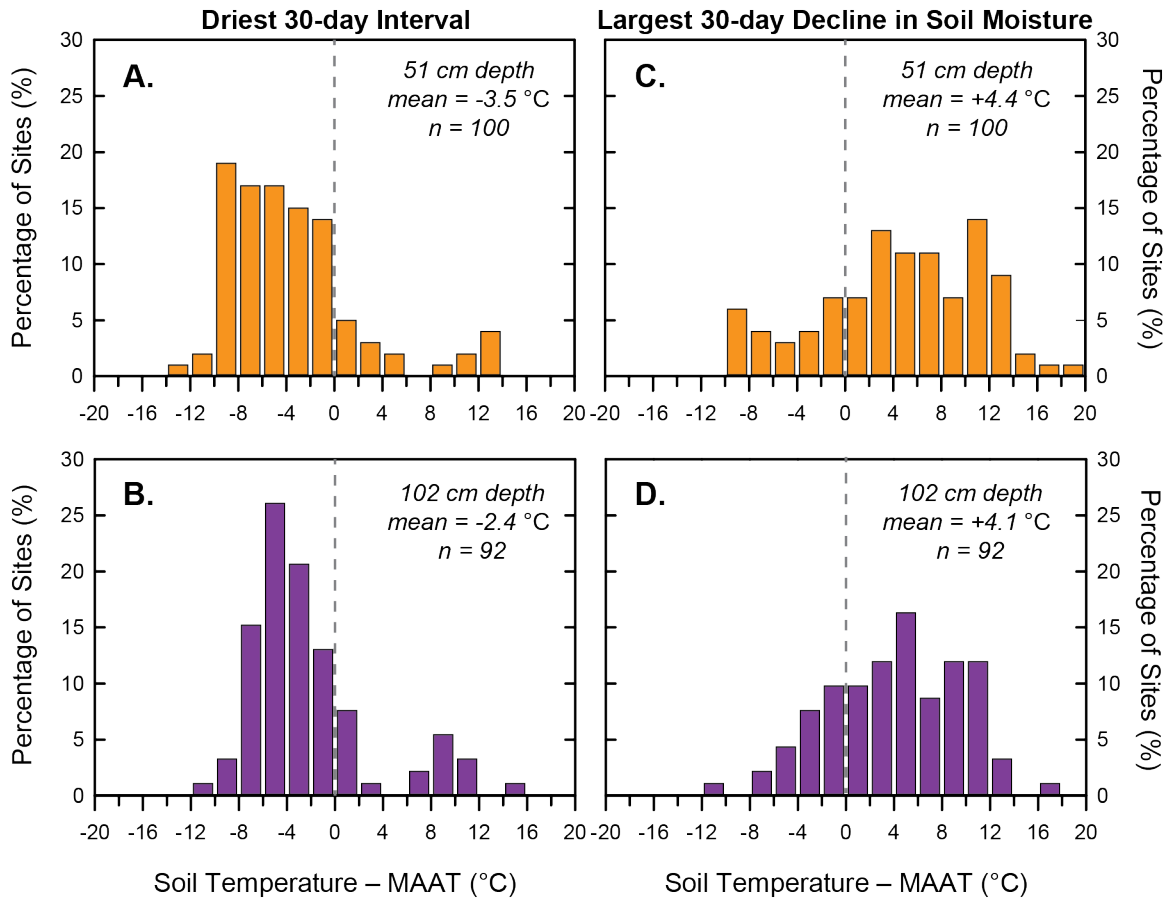

Figure 3.6

Distribution of the temperature biases relative to mean annual air temperature (MAAT) during the corresponding soil moisture scenario: (A-B) the driest 30-day interval during the year and (C-D) the largest 30-day decline in soil moisture.

evenly distributed throughout the year. Unlike the trend described above where the driest 30-day period at 102 cm tends to occur one to six weeks after it occurs at 102 cm, there is not a systematic pattern with respect to the timing of rapid soil water depletion. At many sites, the most abrupt decline in soil moisture occurs nearly synchronously at both 51 and 102 cm depth. A number of sites also record rapid soil water depletion at 102 cm significantly before 51 cm.

The clear differences in seasonal timing between the two soil moisture scenarios considered would result in pedogenic carbonate recording significantly different temperature biases relative to MAAT. Because the driest 30-day interval occurs most frequently during the

winter months, the coeval soil temperature typically falls below MAAT (Figs. 3.6A and 3.6B). Under this scenario, 79−84% of the sites would record a temperature below MAAT (Fig. 3.7). The average cold biases expected at depths of 51 and 102 cm under this scenario are -3.5 and -2.4 °C, respectively. These results starkly contrast with the temperature bias that would be expected under the second soil moisture scenario. If the largest 30-day decline in soil moisture more accurately predicts the seasonal timing of pedogenic carbonate formation, 75−76% of the sites would record a warm bias relative to MAAT, with an average bias of about +4 °C (Figs. 3.6C, 3.6D, 3.8). As discussed above, the majority of carbonate clumped isotope studies examining modern pedogenic carbonate have documented a warm temperature bias relative to MAAT. This warm bias tendency suggests that the seasonal timing of rapid soil moisture depletion more effectively captures the seasonal timing of pedogenic carbonate formation. A systematic cold bias, as suggested by the driest 30-day scenario, is furthermore considered less likely because soil temperatures during the winter months approach 0 °C at many of these sites, and kinetic limitations would likely inhibit carbonate formation.

Although the results from the rapid drying out scenario indicate that a warm season bias is more likely, the magnitude of that bias is difficult to predict. The percentage of SCAN sites are distributed fairly evenly between 0 and +14 °C at 51 cm depth and between 0 and +12 °C at 102 cm (Figs. 3.6C and 3.6D). The absence of a clear trend in the magnitude of the warm-season bias makes it difficult to interpret the seasonal temperature bias recorded by pedogenic carbonate in paleosols. However, the results suggest that warm biases greater than +12–14 °C relative to MAAT are unlikely to occur.

Evaluating the temperature bias results from the rapid soil moisture depletion scenario from a spatial perspective highlights the difficulties encountered when trying to evaluate regional

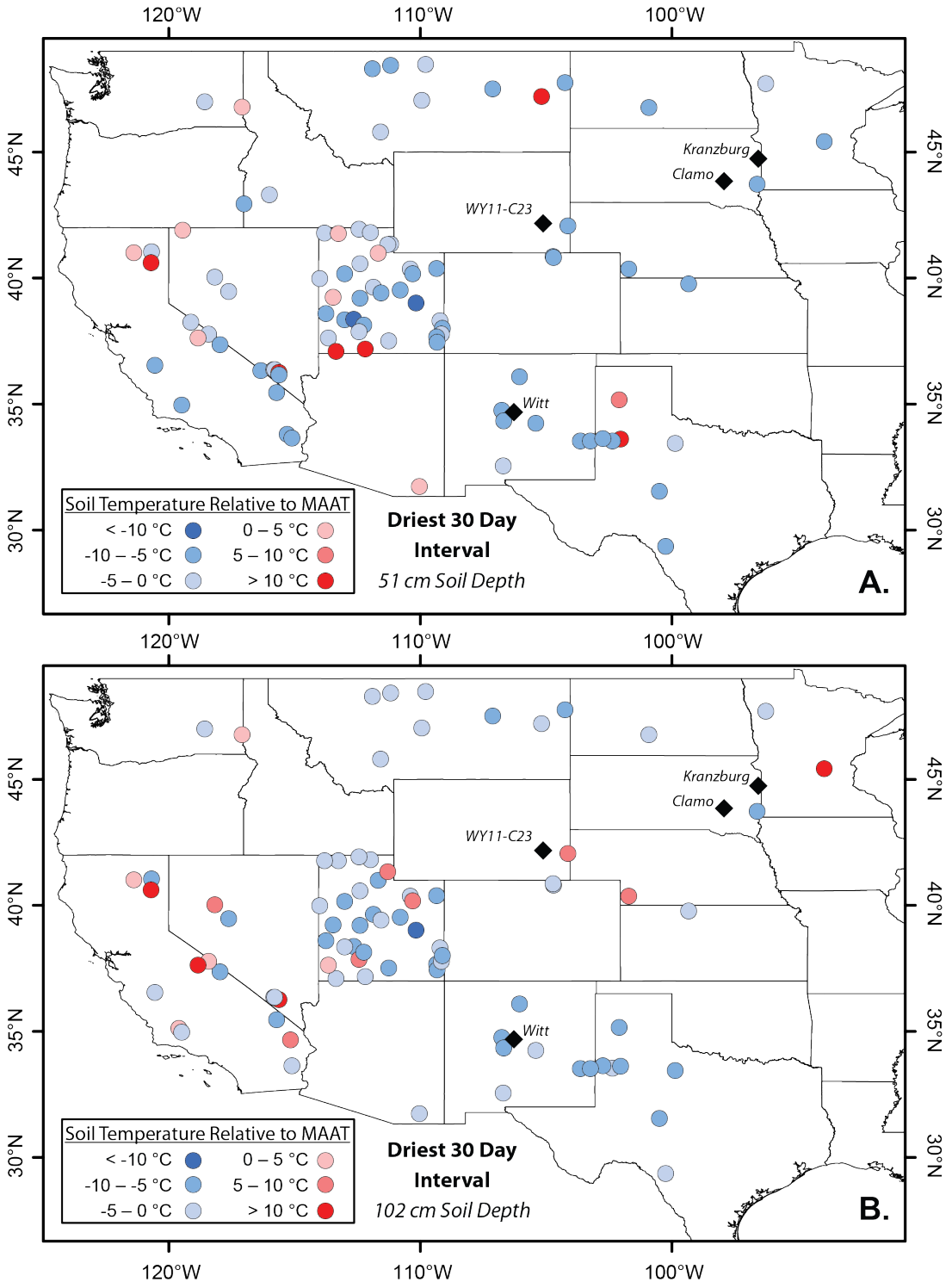

Figure 3.7

Spatial distribution of soil temperatures relative to mean annual air temperature during the driest 30-day interval at (A) 51 cm and (B) 102 cm. and (B) the largest 30-day decline in soil moisture. Black diamonds indicate sites with previously published clumped isotope data from modern pedogenic carbonate samples.

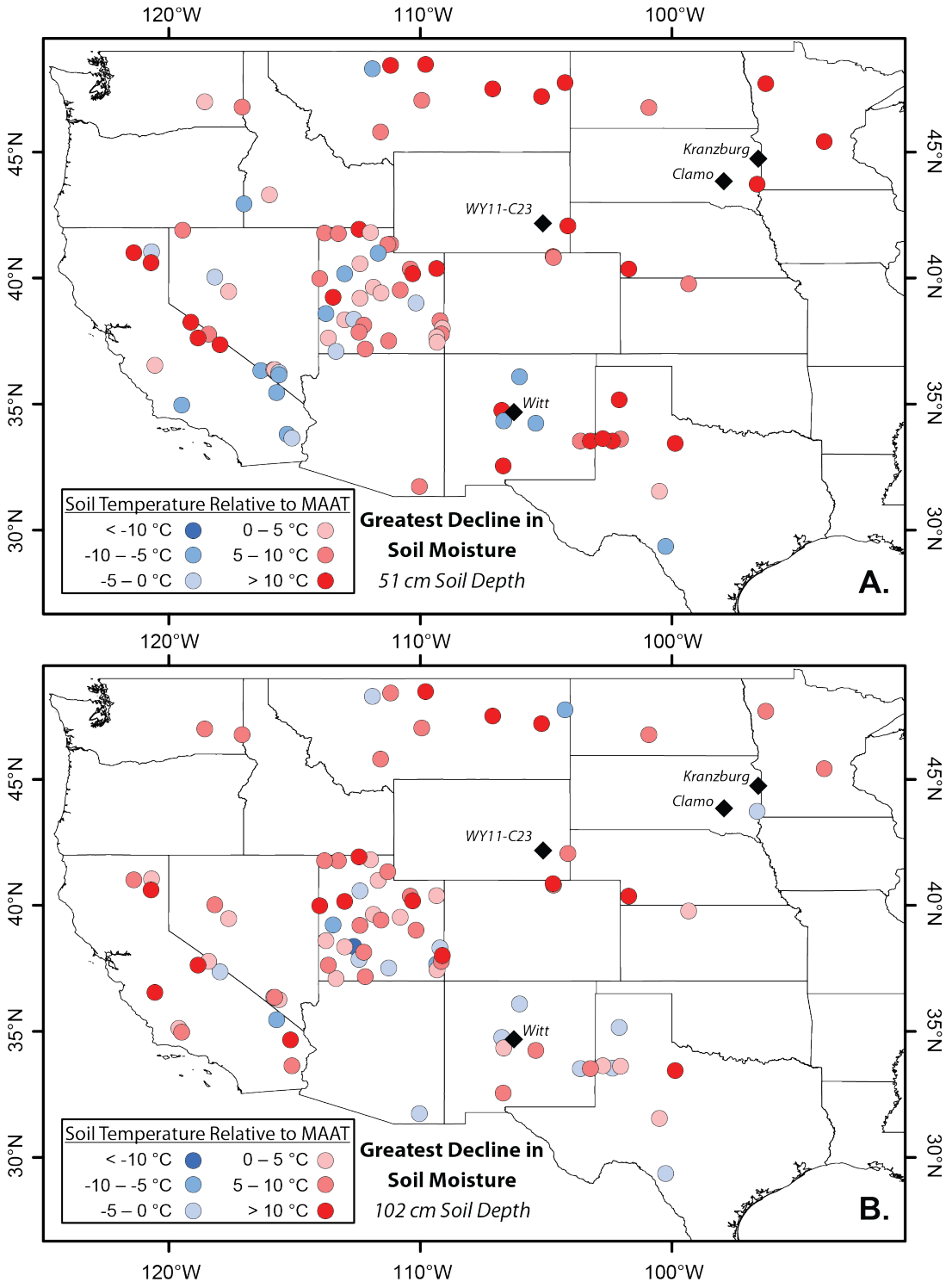

Figure 3.8

Spatial distribution of soil temperatures relative to mean annual air temperature during the larges 30-day decline in soil moisture at (A) 51 cm and (B) 102 cm. and (B) the largest 30-day decline in soil moisture. Black diamonds indicate sites with previously published clumped isotope data from modern pedogenic carbonate samples.

climate from discrete soils. While all of the soils will be affected by trends in regional climate patterns and elevation, individual soil temperature and moisture profiles will be further shaped by local factors such as soil texture, drainage, slope, aspect, and vegetation. The soil temperature bias relative to MAAT at the time of greatest decline in soil moisture is plotted in Figure 3.7 for each SCAN site within the contiguous United States where MAP < 75 cm.

General regional trends in seasonal moisture depletion are apparent at 51 cm (Fig. 3.8A). For example, the sites east of the Rocky Mountain region are consistently characterized by a warm-season bias. These sites are characterized by a continental climate regime, with precipitation peaking during the summer months. The seasonal decline in soil moisture co-occurs with elevated rainfall totals and is likely explained by high evapotranspiration rates during the summer months. Another spatial trend apparent from the 51 cm data is that sites located in the Mojave and northwestern Sonoran deserts are generally characterized by a cool-season bias at 51 cm. These sites are among the most arid evaluated as part of this study, and what little precipitation these sites receive generally falls during the winter, thereby restricting carbonate formation to the cooler seasons.

These two regional trends become less apparent when evaluating data from 102 cm (Fig. 3.8B). At this depth, sites east of the Rocky Mountain region are no longer consistently biased warm, and the sites in the Mojave and Sonoran deserts are no longer predominantly biased cold. These results highlight that a similar season pedogenic carbonate formation cannot be presumed for all depths within a soil. Based on clumped isotope analyses and soil instrumental data from Andean soils, Ringham et al. (2016) observed that pedogenic carbonate formation above 50 cm was likely forced by seasonal precipitation trends, while below 50 cm only the largest rainstorms were able to affect soil moisture content. Our results suggest that this is a common issue at

multiple depths in the soil and therefore complex temperature profiles would be expected from pedogenic carbonate samples collected at multiple depths within the same soil.

Comparing previously published clumped isotope results from pedogenic carbonate to the SCAN data is difficult because few samples were collected close to SCAN sections without major elevation differences or topographic boundaries separating them. However, published clumped isotope data exists relatively close to SCAN stations. Three of these sites produced clumped isotope temperatures that were warmer than MAAT and one site produced temperatures cooler than MAAT (Table 3.1; Hough et al, 2014; Gallagher and Sheldon, 2016). Although the samples were collected slightly above or below 50 cm, the clumped isotope data compare favorably with the temperature bias during the greatest 30-day decline in soil moisture. The warm biased clumped isotope data from Wyoming and South Dakota are within error of the temperature bias predicted by the rapid decline in soil moisture at from the SCAN sites.

While a cold bias relative to MAAT is recorded by pedogenic carbonate from the Witt site in New Mexico (-1.6 ± 3 °C), the corresponding SCAN site suggests that the cold bias should be more extreme (-5.8 °C). These results do not necessarily contradict each other, because the soil moisture data from 102 cm is distinct from the 51 cm data, and instead predict a warm bias of +6.1 °C. The clumped isotope sample was collected at 70 cm. Therefore, a clumped isotope temperature that falls between the two temperatures predicted from the soil moisture data

Table 3.1 Comparison to clumped isotope data

Clumped Isotope Site	State	Sample Depth (cm)	Δ_{47}-derived Temperature (°C)	Uncertatinty ±1 S.E. (°C)	Clumped Isotope Site MAAT (°C)	MAAT – Δ_{47} Temperature (°C)	SCAN Site #	51 cm Temperature Bias[a]
WY11-C23[b]	WY	60	23	3	9.8[c]	13.2	2018	10.2
Clamo[d]	SD	40	22	4	8.5	13.5	2072	10.6
Kranzburg[d]	SD	40	13	4	6.2	6.8	2072	10.6
Witt[d]	NM	70	9	3	10.6	-1.6	2015	-5.8

[a]MAAT – Soil Temperature during the largest 30-day decline in soil moisture
[b]Clumped isotope data from Hough et al. (2014)
[c]Wheatland 4 N Normal Station (USC00489615)
[d]Clumped isotope data from Gallagher and Sheldon (2016)

at 51 and 102 cm is logical for a sample collected at an intermediate depth.

Although there are only four points of comparison, previously published clumped isotope data does support the approach of using the 30-day interval of most rapid soil water depletion to predict the timing of soil carbonate formation. The clumped isotope data also does fall within the upper limit (+14 °C) of warm biases predicted for soils at 50 cm. Future work is required to pair long-term soil moisture and temperature records with clumped isotope data of pedogenic carbonate.

3.5 Conclusions

Sites characterized by winter air temperatures below freezing experience reduced seasonal temperature fluctuations in the soils, likely due to insulation from snow and latent heat processes associated with the freezing and thawing of water. Soils characterized by progressively colder winter air temperatures experience a greater reduction in soil temperature seasonality. A reduction in soil temperature seasonality due to these cold season processes will elevate both MAST and warm season soil temperatures relative to corresponding air temperatures, with MAST more severely affected. Because a reduction in soil temperature seasonality will affect MAST to a greater degree, the biases introduced by winter air temperatures below freezing are of greater concerns for proxies that record MAST. Given that this bias is a function of winter air temperatures dropping below freezing, this phenomenon will be most drastic in proxy applications in continental settings at in mid- to high latitudes and at higher elevations. It is therefore likely that these complications are of lesser concern at low latitudes or during periods of Earth's history characterized by greenhouse climates.

Based on seasonal fluctuations in soil moisture and temperature, pedogenic carbonate formation during the driest 30-day period of the year would be expected to record a systematically cold bias relative to MAAT. In contrast, a warm bias relative to MAAT would be expected if pedogenic formation predominantly occurs when soil moisture declines at the greatest rate. The latter scenario is considered more likely due to a general agreement with modern clumped isotope studies of pedogenic carbonate at sites with nearby instrumental temperature data.

Although a warm-season bias relative to MAAT is considered more likely, the magnitude of this bias is difficult to predict. Temperature biases ranging between -2 and +12 °C appear to be of a similar likelihood. According to data from the SCAN sites, it is unlikely that pedogenic carbonate that forms at or below 51 cm depth would record a temperature more than 12−14 °C warmer than MAAT. Although some broad regional patterns were evident at 51 cm depth, it is difficult to relate the sign and magnitude of the temperature bias to regional climate patterns. Finally, substantially different seasonal fluctuations in soil moisture are observed between 51 and 102 cm depth. This heterogeneity suggests that, at different soil depths, pedogenic carbonate may form during different points of the year. Therefore, carbonate samples from different soil/paleosol depths may not be indicative of the same environmental conditions. When reconstructing temperatures from multiple paleosols, sampling at a consistent depth within the paleosols may minimize complications in interpreting the data.

3.6 References

Arguez, A., Durre, I., Applequist, S., Vose, R.S., Squires, M.F., Yin, X., Heim, R.R., Jr., and Owen, T.W., 2012, NOAA'S 1981-2010 U.S. climate normals: an overview: Bulletin of the American Meteorological Society, v. 93, p. 1687-1697.

Breecker, D.O., Sharp, Z.D., and McFadden, L.D., 2009, Seasonal bias in the formation and stable isotopic composition of pedogenic carbonate in modem soils from central New Mexico, USA: Geological Society of America Bulletin, v. 121, p. 630-640.

Buol, S.W., Southard, R.J., Graham, R.C., and McDaniel, P.A., 2011, Soil genesis and classification: Chichester, West Sussex ; Ames, Iowa, Wiley-Blackwell, xvi, 543 p., 12 p. of col. plates.

Burgener, L., Huntington, K.W., Hoke, G.D., Schauer, A., Ringham, M.C., Latorre, C., and Diaz, F.P., 2016, Variations in soil carbonate formation and seasonal bias over > 4 km of relief in the western Andes (30 degrees S) revealed by clumped isotope thermometry: Earth and Planetary Science Letters, v. 441, p. 188-199.

Cerling, T.E., and Quade, J., 1993, Stable Carbon and Oxygen Isotopes in Soil Carbonates, *in* Swart, P.K., Lohmann, K.C., Mckenzie, J., and Savin, S., eds., Climate Change in Continental Isotopic Records, Volume 78: Geophysical Monograph, American Geophysical Union Geophysical Monograph, p. 217-231.

Clark, M.K., 2007, The significance of paleotopography, *in* Kohn, M.J., ed., Paleoaltimetry: Geochemical and Thermodynamic Approaches, Volume 66: Reviews in Mineralogy & Geochemistry, p. 1-21.

Cotton, J. M., Jeffery, M. L., and Sheldon, N. D., 2013, Climate controls on soil respired CO_2 in the United States: Implications for 21st century chemical weathering rates in temperate and arid ecosystems: Chemical Geology, v. 358, p. 37-45.

Decker, K.L.M., Wang, D., Waite, C., and Scherbatskoy, T., 2003, Snow removal and ambient air temperature effects on forest soil temperatures in Northern Vermont: Soil Science Society of America Journal, v. 67, p. 1234-1242.

Delgado, A., and Reyes, E., 1996, Oxygen and hydrogen isotope compositions in clay minerals: A potential single-mineral geothermometer: Geochimica Et Cosmochimica Acta, v. 60, p. 4285-4289.

Dworkin, S.I., Nordt, L., and Atchley, S., 2005, Determining terrestrial paleotemperatures using the oxygen isotopic composition of pedogenic carbonate: Earth and Planetary Science Letters, v. 237, p. 56-68.

Eiler, J.M., 2011, Paleoclimate reconstruction using carbonate clumped isotope thermometry: Quaternary Science Reviews, v. 30, p. 3575-3588.

Gallagher, T.M., and Sheldon, N.D., 2013, A new paleothermometer for forest paleosols and its implications for Cenozoic climate: Geology, v. 41, p. 647-650.

Gallagher, T.M., and Sheldon, N.D., 2016, Combining soil water balance and clumped isotopes to understand the nature and timing of pedogenic carbonate formation: Chemical Geology, v. 435, p. 79-91.

Ghosh, P., Adkins, J., Affek, H., Balta, B., Guo, W.F., Schauble, E.A., Schrag, D., and Eller, J.M., 2006, ^{13}C-^{18}O bonds in carbonate minerals: A new kind of paleothermometer: Geochimica Et Cosmochimica Acta, v. 70, p. 1439-1456.

Hillel, D., 1980, Fundamentals of soil physics: New York, Academic Press, 413 p.

Hough, B.G., Fan, M., and Passey, B.H., 2014, Calibration of the clumped isotope geothermometer in soil carbonate in Wyoming and Nebraska, USA: Implications for paleoelevation and paleoclimate reconstruction: Earth and Planetary Science Letters, v. 391, p. 110-120.

Jenny, H., 1941, Factors of soil formation; a system of quantitative pedology: New York and London, McGraw-Hill, xii,281 p. p.

Meyer, N.A., Breecker, D.O., Young, M.H., and Litvak, M.E., 2014, Simulating the Effect of Vegetation in Formation of Pedogenic Carbonate: Soil Science Society of America Journal, v. 78, p. 914-924.

NCDC, 2012, 1981-2010 U.S. Climate Normals.

Noy-Meir, I., 1973, Desert ecosystems: environment and producers: Annual Review of Ecology and Systematics, v. 4, p. 25-51.

NRCS, 2015, Soil Climate Analysis Network: Eros Data Center.

Passey, B.H., Levin, N.E., Cerling, T.E., Brown, F.H., and Eiler, J.M., 2010, High-temperature environments of human evolution in East Africa based on bond ordering in paleosol carbonates: Proceedings of the National Academy of Sciences of the United States of America, v. 107, p. 11245-11249.

Peters, N.A., Huntington, K.W., and Hoke, G.D., 2013, Hot or not? Impact of seasonally variable soil carbonate formation on paleotemperature and O-isotope records from clumped isotope thermometry: Earth and Planetary Science Letters, v. 361, p. 208-218.

Quade, J., Eiler, J., Daeron, M., and Achyuthan, H., 2013, The clumped isotope geothermometer in soil and paleosol carbonate: Geochimica Et Cosmochimica Acta, v. 105, p. 92-107.

Ringham, M.C., Hoke, G.D., Huntington, K.W., and Aranibar, J.N., 2016, Influence of vegetation type and site-to-site variability on soil carbonate clumped isotope records, Andean piedmont of Central Argentina (32-34°S): Earth and Planetary Science Letters, v. 440, p. 1-11.

Sheldon, N.D., Retallack, G.J., and Tanaka, S., 2002, Geochemical climofunctions from North American soils and application to paleosols across the Eocene-Oligocene boundary in Oregon: Journal of Geology, v. 110, p. 687-696.

Sheldon, N.D., and Tabor, N.J., 2009, Quantitative paleoenvironmental and paleoclimatic reconstruction using paleosols: Earth-Science Reviews, v. 95, p. 1-52.

Shukla, M.K., 2014, Soil Physics: An Introduction: Boca Raton, FL, CRC Press, 458 p.

Smith, G.D., Newhall, F., and Robinson, L.H., 1964, Soil-temperature regimes their characteristics and predictability, USDA - Soil Conservation Service, 14 p.

Tabor, N.J., and Montanez, I.P., 2005, Oxygen and hydrogen isotope compositions of Permian pedogenic phyllosilicates: Development of modem surface domain arrays and implications for paleotemperature reconstructions: Palaeogeography Palaeoclimatology Palaeoecology, v. 223, p. 127-146.

Tabor, N.J., and Yapp, C.J., 2005, Coexisting goethite and gibbsite from a high-paleolatitude (55 degrees N) Late Paleocene laterite: Concentration and C-13/C-12 ratios of occluded CO2 and associated organic matter: Geochimica Et Cosmochimica Acta, v. 69, p. 5495-5510.

Tabor, N. J., Myers, T. S., Gulbranson, E., Rasmussen, C., and Sheldon, N. D., 2013, Carbon stable isotope composition of modern calcareous soil profiles in California: implications for CO_2 reconstructions from calcareous paleosols. In: Driese, S. G. and Nordt, L. C. Eds.), *New Frontiers in Paleopedology and Terrestrial Paleoclimatology: Paleosols and Soil Surface Analog Systems*.

Van Wambeke, A., 1985, Calculated Soil Moisture and Temperature Regimes of Asia: Washington, DC, USDA - Soil Conservation Service.

Yapp, C.J., 2000, Climatic implications of surface domains in arrays of SD and delta O-18 from hydroxyl minerals: Goethite as an example: Geochimica Et Cosmochimica Acta, v. 64, p. 2009-2025.

CHAPTER 4

Constraining the thermal history of the North American Midcontinent Rift System using carbonate clumped isotopes and organic thermal maturity indices

4.0 Abstract

The Midcontinent Rift System (MRS) is a Late Mesoproterozoic (~1.1Ga) sequence of volcanic and sedimentary rocks exposed in the Lake Superior Region of North America. The MRS continues to be the focus of much research due to its economic mineral deposits as well as its archive of Precambrian life and tectonic processes. In order to constrain the post-depositional thermal history of the MRS, samples were analyzed for carbonate clumped isotope composition and organic thermal maturity. Clumped isotope values from sedimentary/early-diagenetic samples were partially reset during burial to temperatures between 68 and 75 °C. Solid-state reordering models suggest that maximum temperatures of 138–155 °C would be required to reset the clumped isotope values to the observed temperature range before the onset of regional compression and uplift. Clumped isotope results from late-stage veins in the White Pine Mine encompass a greater temperature range (49–116 °C), suggesting that these veins record spatially variable hydrothermal activity and were emplaced after burial temperatures fell below 100 °C in association with regional uplift. Clumped isotope and organic thermal maturity data indicate no significant spatial differences in thermal history along the MRS. Observed variability in bulk

organic matter composition and biomarker indices are therefore more likely a result of shifts in primary productivity or early-degradation processes. These results demonstrate that the MRS experienced a spatially consistent, relatively mild thermal history (<150–200 °C) and is therefore a valuable archive for understanding the Late Mesoproterozoic environment.

4.1 Introduction

The North American Midcontinent Rift System (MRS) is a sequence of volcanic and clastic sedimentary rocks that were deposited around 1.1 Ga. Rocks from the MRS outcrop along both the northern and southern shorelines of western Lake Superior, with gravity and seismic data revealing vast rift deposits below the lake that continue in the subsurface as far southwest as Kansas (Cannon et al., 1989; 2001). Geologic interest in the rocks of the MRS originated during the mid-19th century due to the discovery of native copper deposits on the Keweenaw Peninsula within the Portage Lake Volcanic Group and within the Nonesuch Formation at White Pine (Fig. 1; White, 1968; Ensign et al., 1968). Large-scale copper mining operations began during the 1950s at the White Pine Mine, and exploration and development work continues throughout the region today (Ensign et al., 1968; Bornhorst and Williams, 2013).

Scientific interest in the MRS broadened with the discovery of biomarkers attributed to Precambrian organisms within a petroleum seep originating from the Nonesuch Formation (Meinschein et al. 1965; Eglinton et al. 1965). Evidence for early terrestrial life preserved within the rocks of the MRS has since expanded to include stromatolites (Elmore, 1983), organic-walled microfossils (Wellman and Strother, 2015; Strother and Wellman, 2016), and microbially induced sedimentary structures (Sheldon, 2012; Wilmeth et al., 2014). Geochemical investigations of lacustrine deposits and paleosols have also yielded insights into the

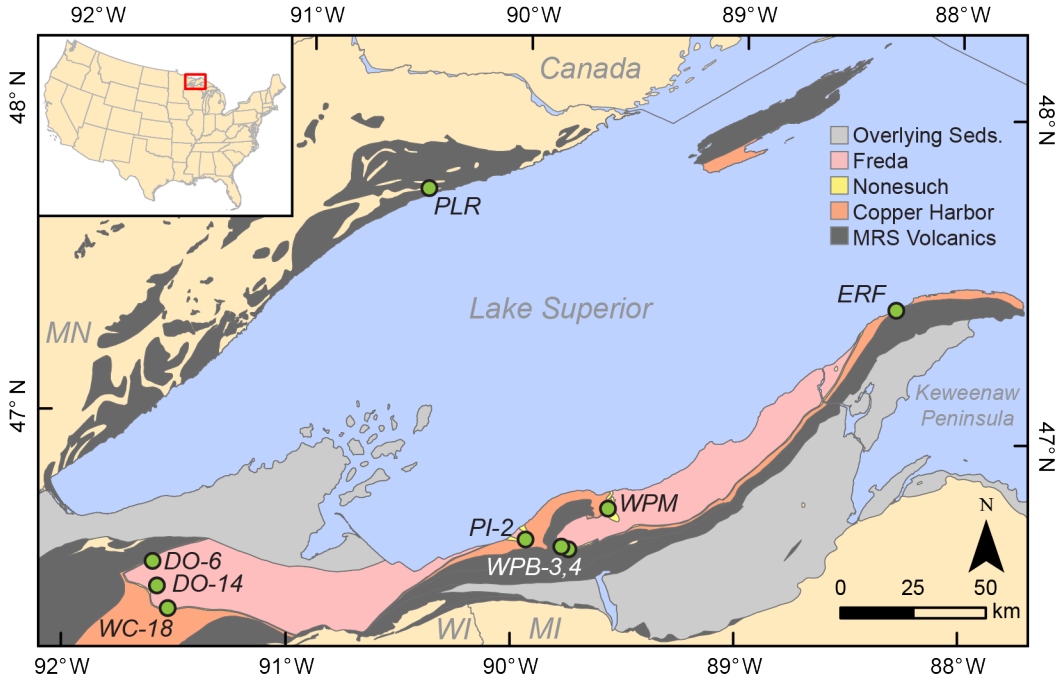

Figure 4.1

Geologic map of surface exposures of the Midcontinent Rift System (MRS) units in the western Lake Superior region. Circles indicate sample localities. MN–Minnesota; WI–Wisconsin; MI–Michigan. ERF–Eagle River Falls; PLR–Pike Lake Road.

Mesoproterozoic atmosphere and other paleoenvironmental variables (Zbinden et al., 1988; Hieshima and Pratt, 1991; Imbus et al., 1992; Mitchell and Sheldon, 2009; 2010; 2016; Cumming et al., 2013; Sheldon, 2013).

The MRS also comprises a well-preserved record of Precambrian tectonics and rift processes. Traditionally the MRS has been characterized as a classic continental rift setting with volcanism driven by a mantle plume (Nicholson et al., 1997), whereas recent work has invoked passive-rifting generated by far-field tension (Levandowski et al., 2015). Failure of the rift has previously been linked to Grenville compression, but is complicated by the cessation of volcanic activity ahead of regional compression (Cannon, 1994; Stein, 2015; Malone et al., 2016). The current understanding of MRS tectonics continues to evolve with recent paleomagnetic data

providing evidence for very rapid plate movement or a possible link to the Laurentia/Amazonia rifting (Swanson-Hysell et al., 2009; Stein et al. 2014).

In order to constrain the paleoenvironmental and tectonic evolution of the MRS accurately, a full understanding of the burial history and diagenetic to metamorphic processes is required. Here we present carbonate clumped isotope and organic thermal maturity data from the MRS in order to evaluate and constrain its diagenetic and burial history. This study primarily focuses on the sedimentary units from the upper peninsula of Michigan and Wisconsin (Fig. 4.1). New thermal data are evaluated in order to assess evidence for a spatially heterogeneous thermal history as well as to constrain better the timing and nature of later hydrothermal activity that produced economically important copper deposits.

4.2 Geologic Setting

4.2.1 Keweenaw Supergroup

The Midcontinent Rift System is a classic rift sequence comprised primarily of more than 1.3×10^6 km^3 of flood basalts and overlying clastic sedimentary units, referred to collectively as the Keweenaw Supergroup (Fig. 4.2; Morey and Green, 1982). Relatively thin sandstone units, including the Bessemer, Puckwunge, and Nopeming Formations, comprise the base of the Keweenaw Supergroup and were likely deposited in a basin that formed in response to early rift subsidence (Ojakangas and Morey, 1982). Igneous activity in the rift began around 1109 Ma and appears to cluster into two episodes of abundant activity (Paces and Miller, 1993). The first pulse (1109–1106 Ma) was characterized by greater eruption rates and includes the Powder Mill Group of Michigan and Wisconsin and the lower units in the North Shore Volcanic Group of Minnesota (Davis and Green, 1997). The second igneous episode extended from 1099 to 1094 Ma and

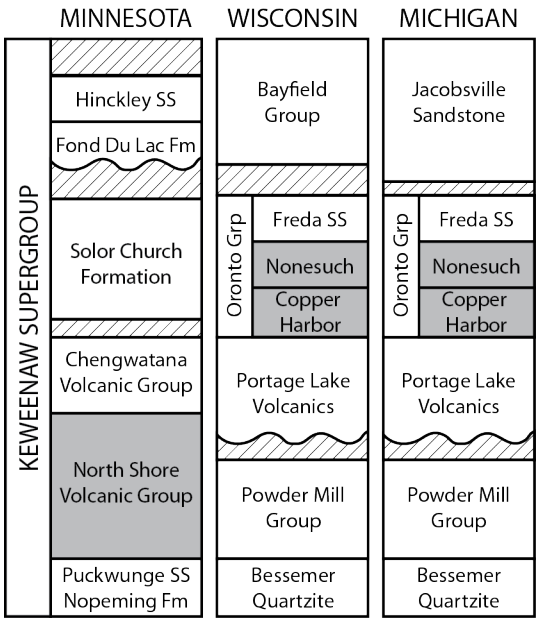

Figure 4.2

Stratigraphic units of the Keweenaw Supergroup in Minnesota, Wisconsin, and Michigan. Units colored in gray were sampled as part of this study. Modified from Cannon and Nicholson (1992) and Ojakangas et al. (2001).

includes the upper units in the North Shore Volcanic Group as well as the Chengwatana Group and Portage Lake Volcanics (Davis and Paces, 1990; Zartman, et al. 1997).

Overlying the volcanic units in Michigan and Wisconsin is the clastic sedimentary Oronto Group, which consists of the Copper Harbor, Nonesuch, and Freda formations (Fig. 4.2). Taken together, these three units represent a continental sequence of alluvial fan, lacustrine, and fluvial depositional systems (Elmore, 1989). The Copper Harbor Formation consists of a fining upward alluvial fan sequence of conglomerates and sandstones that ranges in thickness between 200 and ~2000 m (White and Wright, 1960; Elmore, 1984). The transition from the underlying volcanic rocks into the sedimentary Oronto Group is somewhat gradational because the lower Copper Harbor Formation contains a number of intercalated volcanic deposits (Daniels, 1982). The Nonesuch Formation conformably overlies the Copper Harbor Formation and is comprised predominantly of dark siltstones and shales, and was most likely deposited in a lacustrine

environment (Elmore, 1989; Imbus et al., 1992). The Nonesuch Formation reaches a maximum thickness of around 200 m and its transgressive nature may be explained either by local tectonics or the obstruction of regional drainage patterns (Daniels, 1982). The Nonesuch Formation conformably grades into the red alluvial facies of the Freda Formation, which reaches a thickness of at least 3660 m near the Michigan-Wisconsin border (Daniels, 1982). The Solor Church Formation of Minnesota is thought to be roughly correlative to the Oronto Group (Fig. 4.2); however, it is poorly exposed at the surface and known primarily from drill-cores, which complicates regional correlations (Morey and Ojakangas, 1982). Age constraints on the deposition of the Oronto Group include an andesite flow within the Copper Harbor Formation that yielded a U-Pb age of 1087.2 ± 1.6 Ma (Davis and Paces, 1990). Ages from the Nonesuch Formation include a Pb-Pb isochron age of 1081 ± 9 Ma from a basal carbonate bed in the White Pine Mine area (Ohr, 1993) and a Re-Os age of 1078 ± 24 Ma from the Presque Isle syncline (Cumming et al., 2013).

The Oronto Group is overlain by the Jacobsville sandstone in Michigan and the Bayfield Group in Wisconsin (Fig. 4.2). These units tend to be both texturally and compositionally more mature than Oronto Group sedimentary rocks (Kalliokoski, 1982; Morey and Ojakangas, 1982; Mitchell and Sheldon, 2016). The Jacobsville Formation is estimated to be up to 3,000 m thick based on geophysical data, despite less than 100 m of section exposed at the surface (Kalliokoski, 1982). In contrast, outcrops of the Bayfield group total 815 m (Ojakangas et al., 2001). The exact ages of the Bayfield Group and Jacobsville Formation have proven difficult to constrain. Although the contact between these units and the Oronto Group is not exposed, an unconformity is presumed from seismic data and the contrast between the subhorizontal nature of the Jacobsville Formation and Bayfield group and the steeper dipping beds of the Oronto

Group (Morey and Ojakangas, 1982; Cannon et al. 1989; Ojakangas, et al. 2001). While the Jacobsville has been lithologically correlated to the Bayfield group, paleomagnetic data suggest that the Bayfield Group is younger (Halls and Pesonen, 1982). Detrital zircon $^{207}Pb/^{206}Pb$ dates provide maximum ages of 1059 Ma and 933 Ma for the Bayfield Group and Jacobsville Formation, respectively (Craddock et al., 2013), with most ages for both being younger than 959 ±19 Ma (Malone et al., 2016).

The evolution of the MRS as recorded by the Keweenaw Supergroup can be generally grouped into four stages (Cannon et al., 1989; Ojakangas et al., 2001; Stein et al, 2015). The first stage was characterized by the deposition of the basal sandstone units and the first pulse of rift-filling volcanic rocks between 1109 and 1106 Ma. The next stage corresponds to the second major pulse of volcanic eruptions in the rift (1099–1094 Ma). The deposition of the Oronto Group marks the onset of the third stage, during which volcanism and extension end, and thermal subsidence creates accommodation space. The final stage in the evolution of the MRS consists of regional compression that led to reactivation and reverse movement along the rift-bounding faults (up to 5.5 km; Cannon et al., 1989), followed by the deposition of the Jacobsville Formation and Bayfield Group.

4.2.2 Copper Mineralization

Major copper deposits along the southeastern arm of the MRS include stratiform ore deposits within the basal 1–5 m of the Nonesuch Formation found in the White Pine Mine area (Fig. 4.1). The main stage of copper mineralization in the Nonesuch Formation involved movement of cupriferous fluids though the Copper Harbor Formation into the lower beds of the Nonesuch Formation, where the fluids reacted with organic matter and pyrite to form chalcocite (White, 1971; Brown, 1971; Mauk and Hieshima, 1992; Ho and Mauk, 1996). The main-stage

mineralization is thought to have occurred during relatively early-stage diagenesis, as evidenced by chalcocite-filled fluid escape structures and ore deposits that are cut by high-angle extensional faults (Mauk et al., 1992). Sometime after regional compression began, second-stage copper-bearing fluids migrated along fault conduits located in the southern portion of the mine (Mauk et al., 1992). This second-stage event enriched the copper content through deposition of native copper in the upper Copper Harbor and lower Nonesuch beds, as well as increasing chalcocite accumulation near the top of the mineralization zone (Ho and Mauk, 1996). Although main-stage mineralization is a common feature at the base of the Nonesuch Formation in many places in the MRS, significant second-stage fluid movement and copper enrichment appears to be restricted to the White Pine Mine area (Bornhorst and Williams, 2013).

Native copper deposits are also found within the Keweenaw district in basalts and interbedded conglomerates of the Portage Lake Volcanic Group. Unlike the primary mineralization in the Nonesuch Formation, mineralization in the Keweenaw district likely occurred well after deposition when cupriferous hydrothermal fluids flowed through these units (White, 1971; Jolly, 1974). Based on overlapping age constraints, the possibility exists that second-stage mineralization in the White Pine Mine is related to the mineralization in the Keweenaw Copper district (Mauk et al., 1992). The timing of second stage mineralization in the White Pine Mine is constrained by a Rb/Sr date of 1047 ± 37 Ma on second stage calcite veins (Ruiz et al., 1984). Hydrothermal activity in the Keweenaw district is constrained by Rb/Sr dates on epigenetic amygdule-filling minerals that range between 1060 to 1047 ± 20 Ma (Bornhorst et al., 1988). These ages agree with the timing of regional compression, which is constrained by reset biotite ages of 1060 ± 20 Ma from Archean rocks that were upthrust near the Michigan-Wisconsin border (Cannon et al., 1993).

4.2.3 MRS Thermal History Constraints

Most of the thermal history constraints within the MRS are derived from the Nonesuch Formation. Price and McDowell (1993) assessed variations in clay mineralogy and quantified illite/smectite expandability in core-samples from the Nonesuch and Freda Formations in Michigan and Wisconsin. Clay mineralogy data can be used to estimate a maximum burial temperature, based on the premise that conversion of smectite to illite will be promoted by exposure to elevated burial temperatures (Hower et al., 1976; Hoffman and Hower, 1979). However, the accuracy of smectite-illite clay thermometry is somewhat limited due to uncertainty surrounding the existence of true chemical equilibriums for the associated chemical reactions (Essene and Peacor, 1995). Maximum burial temperatures derived from clay data ranged between 110 and 190 °C, with the hottest temperature recorded at the southwestern margin of the Keweenaw Peninsula. The lowest temperature was recorded in the Iron River Syncline (WPB cores) with intermediate temperatures observed in cores taken from Wisconsin (140 °C) and the White Pine Mine (160 °C).

Examination of organic matter preserved in the Nonesuch formation provides additional constraints on the thermal history of the MRS. Similar to the clay thermometry results, multiple studies observed spatial patterns in the maturity and composition of sedimentary organic matter preserved within the Nonesuch formation. Hieshima and Pratt (1991) analyzed biomarker composition from cores taken along the Southeastern arm of the Midcontinent Rift. They observed spatial trends in the relative abundance of pristane and phytane, which they suggest provides evidence for greater thermal maturity in Wisconsin as compared to Michigan.

Spatial trends in Nonesuch organic matter composition were also observed in organic matter petrography, bulk $\delta\,^{13}C_{org}$ values, and RockEval data (Imbus et al. 1988; 1992). Organic

matter in Michigan samples is predominantly characterized by a filamentous and fluorescent appearance in thin-section, whereas organic matter in Wisconsin has a granular appearance and exhibits little to no fluorescence (Imbus et al. 1988). Further geochemical characterization of the organic matter revealed that there exist small spatial differences in the bulk $\delta^{13}C_{org}$ values and RockEval-derived organic matter composition/maturity. Unlike Hieshima and Pratt (1991), Imbus et al. (1988; 1992) argue that spatial patterns in organic matter composition are more likely attributed to either heterogeneous patterns of primary producer composition or the differential early-diagenetic degradation of organic matter. They argue against different regional thermal histories based primarily on the alternating presence of both organic petrographies (fluorescent vs. non-fluorescent) in a single rock core from Wisconsin.

Using the thermal constraints described above, Price et al. (1996) constructed a best-fit thermal history model for the Nonesuch Formation. Their model suggests that the Nonesuch Formation experienced maximum burial temperatures of around 125 °C after deposition of Freda Formation. The burial temperature decreased in response to regional compression and uplift around 1060 Ma. Modeled burial temperatures increased again after deposition of the Jacobsville Formation/Bayfield Group, but did not return to the previous maximum temperature. A slightly hotter maximum burial temperature of 140–150 °C was estimated by Mauk et al. (1992) by assuming 4 km of overlying sediments.

Thermal constraints on the hydrothermal activity that drove secondary-mineralization processes in the White Pine Mine imply that hydrothermal fluid temperatures were generally < 100 °C (Ho and Mauk, 1996). The best thermal constraint comes from homogenization temperatures of fluid inclusions preserved within second-stage veins that produce temperatures

mostly between 70 and 100 °C (Nishioka, 1983). Monoclinic chalcocite was also observed in some veins, which restricts the formation temperatures to less than 103 °C (Nishioka, 1983).

4.3 Methods

In order to constrain the thermal history of the MRS, samples were collected from different regions of the rift for carbonate clumped isotope and organic thermal maturity analyses (Fig. 4.1). Surface samples were collected from outcrops at Eagle River Falls and Pike Lake Road, while subsurface samples were collected from within the White Pine Mine. Additional samples were taken from six different drill-cores stored at the Northern Michigan Core Repository and the Wisconsin Geological & Natural History Survey Core Repository (Table 4.1). Calcite from surface, drill-cores, and the White Pine Mine was analyzed for clumped isotopes, whereas only drill-core material was analyzed for organic thermal maturity.

Table 4.1 Sample type and locality

Site	Location		Geologic Unit	Sample Type	Calcite Lithology	Geochemical Analyses	
	N (°)	W (°)				Clumped Isotopes	Organic
Minnesota							
PLR	47.747	90.445	NSVG	Hand-Sample	Vesicle Fill	Y	-
Wisconsin							
DO-6	46.554	91.615	Copper Harbor	Core	Cement	Y	Y
DO-14	46.479	91.587	Nonesuch	Core	Limestone	Y	Y
WC-18	46.411	91.532	Nonesuch	Core	Cement	Y	-
Michigan – Presque Isle Syncline							
PI-2	46.674	89.946	Nonesuch	Core	Cement	Y	Y
Michigan – Iron River Syncline							
WPB-3	46.656	89.784	Nonesuch	Core	N/A	-	Y
WPB-4	46.651	89.752	Nonesuch	Core	N/A	-	Y
Michigan – White Pine Mine[a]							
WP-338	46.779	89.579	Nonesuch	Hand-Sample	Late-Stage Vein	Y	-
WP-079	46.779	89.579	Nonesuch	Hand-Sample	Late-Stage Vein	Y	-
WP-148	46.779	89.579	Nonesuch	Hand-Sample	Late-Stage Vein	Y	-
WP-442	46.779	89.579	Nonesuch	Hand-Sample	Limestone	Y	-
Michigan – Keweenaw Peninsula							
ERF	47.412	88.297	Copper Harbor	Hand-Sample	Cement	Y	-

[a]Location information for White Pine Mine samples are approximate

4.3.1 Carbonate Clumped Isotope Geochemistry

Carbonate clumped isotope thermometry is based on the observation that the abundance of carbonate isotopologues containing at least two rare isotopes (e.g. ^{13}C and ^{18}O) increases at lower formation temperatures (Ghosh et al., 2006a). This tool has been applied to help constrain paleoenvironmental changes (e.g. Ghosh et al., 2006b; Passey et al., 2010; Eiler, 2011) as well as the extent and nature of post-depositional processes (e.g. Bristow et al., 2011; Huntington et al., 2011; Ferry et al., 2011; Shenton et al., 2015).

Clumped isotope and simultaneously measured $\delta^{13}C$ and $\delta^{18}O$ data were collected during three separate measurement sessions between September 2014 and February 2016 at the University of Michigan Stable Isotope Laboratory. The laboratory set-up and methodology for clumped isotope analyses are detailed in full by Defliese et al. (2015). For all runs, between 4 and 15 mg of sample was acidified in anhydrous H_3PO_4 held at 75 °C. The resulting CO_2 was purified off-line under vacuum via cryogenic separation and a Porapak-Q filled column. Samples were then analyzed on a Thermo Scientific MAT 253 dual inlet stable isotope mass spectrometer outfitted to collect masses 44–49. Clumped isotope results are reported in Δ_{47} notation, which is defined as:

$$\Delta_{47} = \left[\left(\frac{R^{47}}{R^{47*}} - 1\right) - \left(\frac{R^{46}}{R^{46*}} - 1\right) - \left(\frac{R^{45}}{R^{45*}} - 1\right)\right] \times 1000$$

where R^i is the observed ratio of that particular mass CO_2 to mass-44 CO_2 and R^{i*} is the corresponding stochastic distribution based on the bulk sample composition (Affek and Eiler, 2006).

Reference gasses of varying isotope composition were heated to 1000 °C and analyzed throughout data collection periods in order to account for scale compression and non-linearity effects (Huntington et al., 2009). Measured Δ_{47} values were subsequently normalized to the

absolute reference frame of Dennis et al. (2011) using the heated gasses, CO_2 standards equilibrated with H_2O at 25 °C, and the Carrara Marble interlaboratory standard. Finally, an empirical acid fractionation factor of 0.067‰ was applied to Δ_{47} values for samples reacted at 75 °C (Hren et al., 2013). Average reproducibility of carbonate standards was 0.020‰ (1 sd). Error on individual samples was calculated as the minimum of either 1) the measured standard error on *n* replicates or 2) the standard error calculated for a Carrara Marble with the same number of replicates ($0.020/\sqrt{n}$.)

During the September 2014 measurement session, samples were measured for eight acquisitions comprised of 10 cycles each, as described in Defliese et al. (2015). Analytical methods were slightly modified ahead of the December 2015 run to measure for five acquisitions of 12 cycles each, with the bellows pressure balanced ahead of each acquisition. No statistically significant differences were observed in measured values of interlaboratory or internal standards as a result of this modification. The CO_2 purification procedure was also adjusted ahead of the December 2015 run in response to observed fractionations in $\delta^{13}C$ and $\delta^{18}O$ values associated with the Porapak-Q column temperature (Petersen et al., 2016). During the September 2014 run, the Porapak-Q column was held at -25 °C, whereas it was held between -10 and -15 °C in the latter two runs. Corrections to the September 2014 data were carried out following Petersen et al. (2016).

Discrepancies between empirically derived clumped isotope temperature calibrations have been observed among various laboratory groups. These calibrations generally fall into two broad categories: calibrations developed at laboratories that digest samples at temperatures > 70 °C and those that digest samples at 25 °C (Fernandez et al., 2014). Results herein are presented and discussed using the calibration of Kluge et al. (2015) because it included high temperature

samples (25–250 °C) and is statistically similar to calibrations determined within the University of Michigan Stable Isotope Laboratory (Table 4.2; Defliese et al., 2015). For comparison, clumped isotope temperatures are also presented in Table 4.2 using the theoretical calibration of Schauble et al. (2006) calibration and a 25 °C-digestion calibration (Ghosh et al. 2006a).

Table 4.2 Clumped isotope geochemistry results

Sample	Height (m)[a]	n[b]	$\delta^{13}C$ (‰) VPDB	$\delta^{18}O$ (‰) VPDB	Δ_{47} (‰) ARF[c]	σ (‰)[d]	± 1 S.E. (‰)[e]	Temp (°C) 'Kluge'[f]	± 1 S.E. (°C)	Temp (°C) 'Ghosh'[g]	Temp (°C) 'Schauble'[h]
Minnesota											
PL-12-09	n/a	3	-2.4	-17.0	0.557	0.043	0.025	84	14	63	82
Wisconsin											
DO6-62-9	-0.7	3	-4.1	-6.4	0.587	0.008	0.012	69	6	55	67
DO14-117-8	67.6	3	-4.9	-7.3	0.582	0.017	0.012	71	6	56	69
WC18-49-7	47.9	3	-2.9	-7.4	0.575	0.008	0.012	75	6	58	73
Michigan – Presque Isle Syncline											
PI2-50-2	8.8	4	-12.3	-8.5	0.578	0.015	0.010	73	5	57	71
Michigan – White Pine Mine											
WP-338	??	3	-7.7	-12.0	0.630	0.010	0.012	49	5	43	48
WP-148	0.7	3	-8.7	-14.1	0.565	0.007	0.012	80	6	61	78
WP-079	4.0	4	-9.1	-13.9	0.507	0.015	0.010	116	7	79	111
WP-442	0.4	5	-7.9	-8.5	0.576	0.011	0.009	74	5	58	72
Michigan – Keweenaw Peninsula											
CHC-12-04	n/a	3	-0.9	-7.9	0.588	0.022	0.013	68	6	54	66

[a]Stratigraphic height relative to the Copper Harbor–Nonesuch contact
[b]Number of replicate analyses
[c]Values normalized to the absolute reference frame (ARF) of Dennis et al. (2011)
[d]Standard deviation of replicate analyses
[e]Standard error calculated by dividing σ by the square root of n, where σ is calculated from replicate analyses unless it is exceeded by the long-term σ of standards (0.020‰)
[f]Temperature calibration of Kluge et al. (2014)
[g]Temperature calibration of Ghosh et al. (2006), modified for use in the ARF by Dennis et al. (2011)
[h]Theoretical temperature calibration of Schauble et al. (2006)

4.3.2 Organic Geochemistry

Organic geochemistry sample preparation and analyses were performed at the Biogeochemistry Laboratory at the Australian National University. To limit possible contamination from modern sources or from drilling fluids, the exterior surfaces of samples were removed with a solvent-cleaned rock saw as described in Brocks et al. (2008). The exterior and interior portions of trimmed samples were then pulverized separately using a steel puck mill. Grinding equipment was cleaned with dichloromethane and methane between samples. Bitumen

was extracted from pulverized samples according to the methodology described by Jarrett et al. (2013). Laboratory blanks of combusted quartz sand were used to monitor contamination during analyses. Extracted samples were then analyzed on an Agilent 6890 gas chromatograph (GC) coupled to a Micromass Autospec Premier double sector mass spectrometer. Helium was used as the carrier gas and the GC was equipped with a 60 m DB-5 MS capillary column. Samples were injected in *n*-hexane at 60 °C before being heated to 300 °C. Data collected was used to calculate a series of thermal maturity index values. The equations and references for these are found in Table 4.3.

4.4 Results

4.4.1 Carbonate Geochemistry Results

Complete clumped isotope geochemistry results are presented in tables C.1 and C.2. Average Δ_{47} values ranged between 0.630 and 0.507‰ (Table 4.2). With the exception of samples PLR-12-09 and CHC-12-04, the long-term standard deviation of replicate standard analyses (0.020‰) exceeded the standard deviation of replicate sample analyses. Clumped isotope derived temperatures for sedimentary and early diagenetic calcite in the Nonesuch and Copper Harbor formations cluster tightly between 68 ± 6 °C and 75 ± 6 °C (Fig. 4.3). Conventional carbonate stable isotope results from these same samples exhibit more variability. The $\delta^{18}O$ values range between -6.4 and -8.5‰, with slightly more ^{18}O-depleted values in Michigan samples (-7.9 to -8.5‰) than Wisconsin samples (-6.4 to -7.4‰). The $\delta^{13}C$ values span a much greater range (-0.9 to -12.3‰), but do not display a clear geographic trend, as the samples with the most ^{13}C-enriched and most ^{13}C-depleted $\delta^{13}C$ values both come from Michigan.

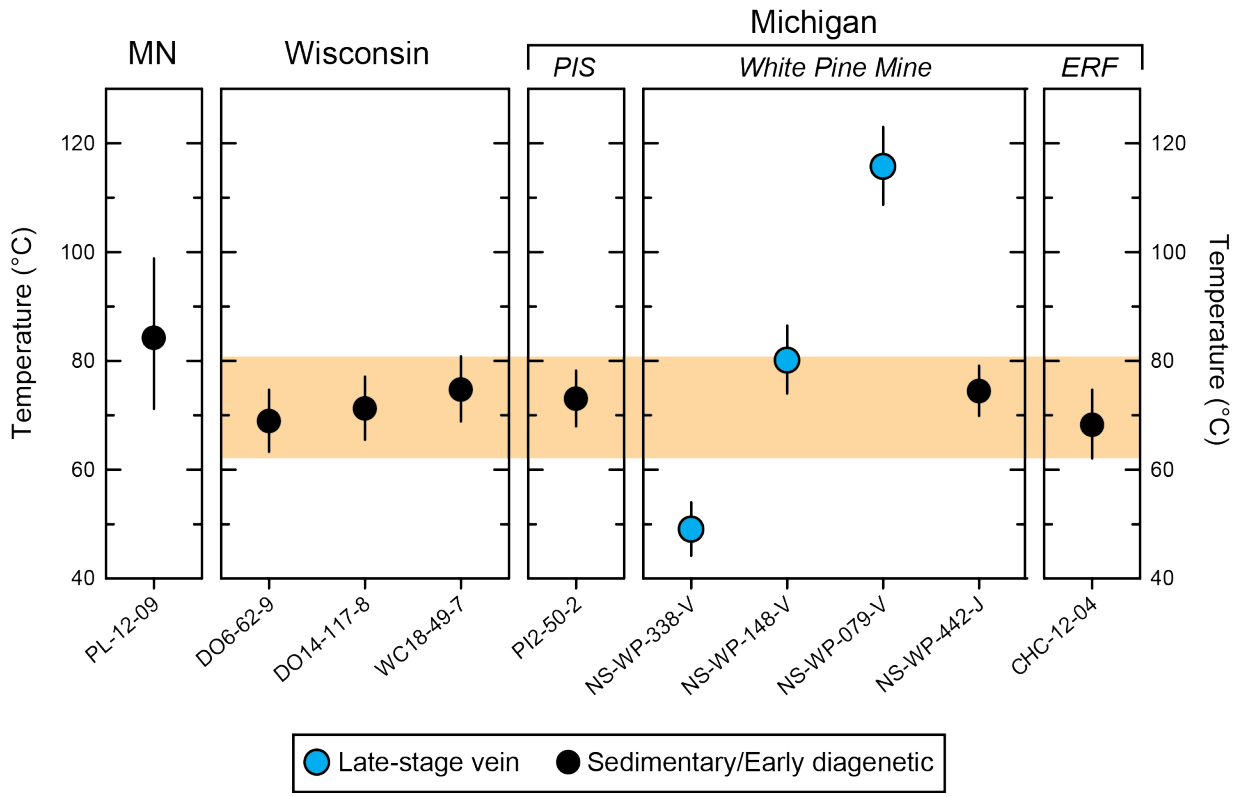

Figure 4.3

Clumped isotope temperatures results for calcite samples from the Midcontinent rift. Error bars display ±1 standard error. Solid black symbols represent calcite that formed either at the time of deposition or during early diagenesis. Blue symbols represent the late-stage veins from the White Pine Mine. The orange window highlights the range of values in the sedimentary/early-diagenetic calcite pool (± error) MN – Minnesota; PIS – Presque Isle Syncline; ERF – Eagle River Falls.

The average clumped isotope temperature of 84 ± 14 °C determined for the calcite-filled basalt vesicle from the North Shore Volcanic Group in Minnesota was the least reproducible clumped isotope sample. The temperature of 84 ± 14 °C is within the error range for the hottest measured temperatures within the sedimentary and early diagenetic samples from the Oronto Group. The $\delta^{13}C$ value of this sample (-2.4‰) is within the observed range of Oronto Group samples; however the $\delta^{18}O$ value of -17.0‰ for this sample falls well below those same samples.

Late stage vein samples from the Nonesuch Formation in the White Pine Mine span a much larger temperature range than the sedimentary and early diagenetic samples, with values between 49 ± 5 °C and 116 ± 7 °C. The $\delta^{18}O$ and $\delta^{13}C$ values from the veins fall at the lower end

of the range observed in sedimentary and early diagenetic samples, with values between -12.0 – -14.1 and -7.7 – -9.1‰, respectively.

Table 4.3 Organic thermal maturity data

Sample	Height (m)[a]	MDI (%)[b]	$C_{31}22$ S/(S+R)[c]	$C_{30}\beta\alpha\alpha\beta$[d]	$C_{27}T_S$/ (T_s+Tm)[e]	Phen/MP[f]	MPI-1[g]	R_C[h]	TA (%)[i]
Wisconsin									
DO-6-51-3	69.4	0.34	0.59	0.24	0.032	n/c	n/c	n/c	n/c
DO-6-54-7	43.8	0.53	0.58	0.10	1.0	0.88	0.33	0.6	41
DO-14-112-5	66.3	n/c	n/c	0.094	2.6	n/c	n/c	n/c	n/c
Michigan – Presque Isle Syncline									
PI2-10-4	173.6	0.34	0.59	0.28	0.22	0.88	0.25	0.55	42
PI2-35-6	69.0	0.36	0.57	0.21	0.71	n/c	n/c	0.40	n/c
PI2-43-4	37.5	0.34	0.58	0.12	0.90	0.49	0.23	0.54	75
PI2-48-2	17.8	0.58	0.59	0.14	0.81	n/c	n/c	n/c	n/c
Michigan – Iron River Syncline									
WPB3-40-1	140.7	0.29	0.58	0.27	0.21	0.70	0.24	0.54	41
WPB3-47-2	110.8	0.38	0.58	0.21	0.48	1.4	0.26	0.56	n/c
WPB3-??	??	n/c	0.58	0.29	0.20	1.20	0.31	0.59	50
WPB3-54-4	78.9	n/c	0.58	0.32	0.046	0.67	0.22	0.53	n/c
WPB4-8-2	127.5	n/c	0.58	0.35	0.11	0.41	0.25	0.55	56
WPB4-26-3	50.9	n/c	0.58	0.25	0.061	1.1	0.24	0.55	n/c
WPB4-??	??	n/c	0.60	0.24	0.034	1.3	0.27	0.56	73

n/c = not computable due to low signal-to-noise ratio

[a]Stratigraphic height relative to the Copper Harbor–Nonesuch contact

[b]MDI: Methyldiamantane (MD) index, MDI = 4-MD/(1-MD+3-MD+4-MD) (Chen et al., 1996)

[c]Hopane ratio C_{31} S/(S+R) expressed in percent, S and R are stereoisomers of the respective αβ-hopane (Seifert and Moldowan, 1980)

[d]Ratio of C_{30} moretane(βα) and hopane (αβ): βα/αβ (Seifert and Moldowan, 1980a)

[e]C_{27} hopane ratio with T_s = 18α-22,29,30-trisnorneohopane and T_m = 17α-22,29,30-trisnorhopane, (Siefert and Moldowan, 1978)

[f]Ratio of Phenanthrene (Phen) and Methylphenanthrenes (MP), Phen/MP = Phen/(3-MP+2-MP+9-MP+1-MP)

[g]The MPI-1 (Radke and Welte, 1983) was corrected for laboratory-specific response area: 1.5*(1.74*3-MP + 1.65*2-MP)/(P + 3.62*9-MP + 2.43*1-MP).

[h]Calculated vitrinite reflectance R_c = 0.6*MPI-1+0.4 (Radke et al., 1982).

[i]Triaromatic (TA) steroid ratio, TA = (C_{20}+ C_{21})/(C_{20}+ C_{21}+ C_{27}+ C_{28}+ C_{29}) in % (here only 4-methyl TA in the *m/z* 245 trace were identified and used, however not all homologues were detected)

4.4.2 Organic Geochemistry Results

Organic thermal maturity results are presented in Table 4.3. Samples from different cores of the Nonesuch produced fairly consistent results for a number of thermal indices. For example, C_{31} hopane 22S/(22S+22R) ratios all fall between 0.57 and 0.60. Methlydiamantane index (MDI) values between 0.29 and 0.38 were found in all cores. The stratigraphically lowermost samples cores DO-6 and PI-2 produced slightly greater MDI values of 0.53 and 0.58, respectively. C_{30} moretane to hopane ratios were > 0.1, with the exception of two samples from Wisconsin. The MPI-1 values were also fairly consistent and ranged between 0.22 and 0.33. Two of the organic indices exhibited greater variability between samples. C_{27} hopane T_s/(T_s + T_m) values ranged

between 0.032 and 2.6, and the ratio of phenanthrene to methylphenanthrene produced values from 0.49 to 1.4.

4.5 Discussion

Carbonate clumped isotope derived temperatures from the sedimentary and early diagenetic phases are restricted between 68 and 75 °C, which is much hotter than what would be expected for (near) surface temperatures during sedimentation. Therefore, it is likely that the clumped isotope values were reset to hotter temperatures during burial. As stated above, maximum burial temperature estimates for the Nonesuch Formation derived from clay thermometry data range between 110 and 190 °C (Price et al., 1993). Maximum burial temperatures calculated based on estimates of heat flow and overlying sediment thickness fall in the middle of this temperature range (140–150 °C; Mauk et al., 1992). The disparity between these constraints and the clumped isotope temperatures suggests that the latter do not represent the maximum burial temperature, but instead were partially reset to intermediate temperature values.

Unlike conventional carbonate stable isotope values ($\delta^{13}C$ and $\delta^{18}O$), reordering of clumped isotopes can occur in the solid state and does not require interaction with a fluid (Passey and Henkes, 2012). The small amount of Δ_{47} variability that exists between sedimentary and early-diagenetic calcite samples could be attributed to factors such as minor differences in burial depth, different initial formation temperatures, or different trace element compositions (e.g. Passey and Henkes, 2012). Post-depositional hydrothermal interacted with the basal Nonesuch Formation in all of the Michigan localities sampled as part of this study. Evidence for this fluid activity comes from enriched copper concentrations within the lowermost 10–15 meters of the

Nonesuch Formation. Copper mineralization in this interval formed from copper-bearing fluids that flowed through the underlying permeable and porous red beds of the Copper Harbor Formation before reaching the less-permeable Nonesuch Formation, which is relatively enriched in organic matter (White, 1971; Brown, 1971; Mauk and Hieshima, 1992). Dissolution and re-precipitation of calcite during this event could have reset the clumped isotope values; however, clumped isotope values from sedimentary and early diagenetic calcite within the copper-mineralized zone are consistent with those collected from the overlying, unmineralized sedimentary rocks. This consistency implies either that there was not significant dissolution/re-precipitation associated with this fluid event, or that any calcite formed during this event did so soon after deposition when temperatures remained similar to the formation temperatures of overlying samples.

In contrast, the late-stage veins from the White Pine Mine record a much wider temperature range of 49–116 °C, extending to hotter and cooler temperatures than those recorded by previous fluid inclusion homogenization temperatures (70–100 °C; Nishioka, 1983). This disparity could be a result of sampling different veins that formed at a wider range of temperatures. Alternatively, temperatures at the hotter end of this range (116 °C) could be a product of partial resetting of the clumped isotope composition during burial, as seen with the sedimentary and early diagenetic carbonates. However, partial resetting would not explain the absolute range of observed temperatures, because all veins in the mine were deposited at a similar time and therefore would have experienced the same burial history. The more likely explanation is that these veins were initially formed at different temperatures and are recording variable fluid temperatures in different areas of the mine. Certain areas of the White Pine Mine are characterized by greater vein activity and secondary copper mineralization. For example,

Sample WP-079 comes from one of these productive units of the mine (Unit 96) and produced the hottest clumped isotope temperature (116 °C), which suggests that hotter hydrothermal fluid temperatures may correlate with the more productive areas of the mine.

The relatively small temperature window of 68–75 °C recorded by the sedimentary and early-diagenetic calcite samples suggests that significant spatial differences in thermal history along the southeastern arm of the Midcontinent Rift did not occur. This interpretation contrasts with the clay thermometry data of Price and McDowell (1993), which was used to suggest that the Nonesuch Formation in different areas experienced a large range of maximum temperatures (110–190°). The wide range of temperatures derived from the clay mineralogy could be a product of factors other than temperature, such as a variable lithology, post-depositional fluid activity, or metastability of clay phases (Price and McDowell, 1993; Essene and Peacor, 1995).

A spatially consistent thermal history along the southeastern arm of the Midcontinent Rift is further supported by the consistent nature of organic thermal maturity data presented herein (Table 4.3). After burial, sedimentary organic matter is transformed by heat-driven reactions. Specifically, the stereochemistry of preserved steranes and hopanes can be used to assess the degree of organic thermal maturity with respect to oil generation (Mackenzie et al., 1980; Seifert and Moldowan, 1980). All samples entered the oil generation window as evidenced by isomerization of C_{31} 17αβ-hopanes at C-22. When bitumen enters the oil window, C_{31} 22S/(22S+22R) ratios attain equilibrium values between 0.57–0.62 (Mackenzie et al., 1980; Seifert and Moldowan, 1980). Samples from the Nonesuch fell within this range, with values of 0.57–0.60.

Additional thermal maturity indices indicate that samples tend to be of low to moderate thermal maturity. The moretane ratio C_{30} βα/αβ is greater than 0.1 for all but one sample, which

indicates low thermal maturity (Grantham, 1986; Mackenzie et al., 1980; Seifert and Moldowan, 1980). Low thermal maturity is further supported by methylphenanthrene index (MPI-1) values between 0.22 and 0.33. For most samples, the ratio of phenanthrene to methylphenanthrene is < 1, demonstrating that the MPI is not reversed (Brocks et al., 2003). Vitrinite reflectance (Rc) values calculated from the MPI ranged between 0.40 and 0.60, which represent low maturity bitumens that entered the early oil generation window (Boreham et al., 1988; Radke and Welte, 1983). The methyldiamantane index (MDI) is below 0.50 for all samples except DO6-54-7 and PI2-48-2, indicating that thermal maturities are generally low to moderate (Chen et al., 1996).

The absence of clear spatial trends in the organic thermal maturity data contrasts with previously published relative abundances of pristane and phytane as compared to *n*-alkanes (Hieshima and Pratt, 1991). Hieshima and Pratt (1991) interpreted these data as a product of greater thermal maturity in Wisconsin as compared to Michigan. However, biodegradation processes are also known to affect pristane and phytane abundances (Peters et al., 2005). We also observed greater variability in organic parameters that are affected by multiple processes. For example, C_{27} $T_s/(T_s+T_m)$ hopane ratios, which are controlled by both thermal maturity and source composition (Peters et al., 2005), are highly variable in our samples (0.03–2.9). The lack of spatial variability in sedimentary/early-diagenetic clumped isotope results combined with generally consistent thermal maturity indices suggests that the variability in these other organic parameters, including Pr/Ph, is more likely a product of variations in source material or degradation under fluctuating environmental conditions at the time of deposition and early diagenesis. Imbus et al. (1992) similarly concluded that slight differences observed in $\delta^{13}C_{org}$ values between Wisconsin and Michigan were a result of environmental rather than thermal differences.

4.5.1 Solid-state reordering model

In addition to assessing spatial trends in thermal history, the clumped isotope results can be used to refine the burial history of the Nonesuch Formation. A solid-state reordering model can be used to evaluate how the clumped isotope temperatures would be reset under various thermal history scenarios (Passey and Henkes, 2012; Henkes et al., 2014; Stolper and Eiler, 2015). The first order approximation model and 'transient defect/equilibrium' models predict that the clumped isotope composition of samples are likely to remain stable on geologic timescales if temperatures do not exceed 100 °C, and rapid partial resetting of Δ_{47} temperatures is not expected until burial temperatures reach 150–160 °C (Henkes et al., 2014). Slightly cooler temperature thresholds are suggested by the modeling results of Stolper and Eiler (2015), which predict that measurable Δ_{47} temperature changes do not occur if burial temperatures remain below 75 °C. Their results predict Δ_{47} temperatures will increase by 10–25 °C when burial temperatures are between 80–100 °C, whereas if burial temperatures exceed 125 °C, a rapid partial increase in Δ_{47} temperatures will be followed by a slower change until the environmental temperature is reached (Stolper and Eiler, 2015).

Existing thermal constraints and the thermal history model of Price et al. (1996) suggest that the Copper Harbor and Nonesuch formations experienced temperatures high enough to result in partial resetting of the Δ_{47} values. As discussed above, thermal reconstructions suggest that maximum burial temperatures did not exceed 200 °C, with the majority of temperature constraints and estimates falling below 150 °C. Therefore, the first order approximation model can be used because the predicted reordering rates of the first-order approximation model and 'transient defect/equilibrium' model are nearly identical at temperatures below 150–200 °C

(Henkes et al., 2014). Changes in Δ_{47} values during burial can be predicted using the following equation:

$$\ln\left[\frac{\Delta_{47}^{t}-\Delta_{47}^{eq}}{\Delta_{47}^{init}-\Delta_{47}^{eq}}\right]=-tK_0\exp\left[\frac{-E_a}{RT}\right]$$

where Δ_{47}^{t} is the clumped isotope composition after a given time duration (t), Δ_{47}^{eq} is the equilibrium clumped isotope composition at a given temperature, Δ_{47}^{init} is the initial clumped isotope value at the beginning of a time interval, K_0 and E_a are empirically derived constants, R is the universal gas constant, and T is the temperature. Marginally different values for K_0 and E_a were derived from results of heating experiments that assessed brachiopod and optical calcite samples (Passey and Henkes, 2012; Henkes et al., 2014). Because the model was developed using the theoretical calibration of Schauble et al. (2006), this temperature calibration was used for the modeling portion of the work.

The thermal history produced by Price et al. (1996) for the basal Nonesuch Formation was used as an initial input to drive the solid state reordering model (Fig. 4.4), with the initial clumped isotope temperature set at 25 °C. In this thermal history, the basal Nonesuch reaches a maximum burial temperature of 125 °C at 1073 Ma before cooling rapidly around 1060 Ma in association with regional uplift and erosion of overlying sediments. A subsequent increase in burial temperature occurs at around 1035 Ma due to deposition of the overlying Jacobsville Formation and Bayfield Group, although temperatures never again exceed ~85 °C and slowly cool towards present day.

To test the sensitivity of clumped isotope reordering to different burial histories, the maximum burial temperature was varied between 125–150 °C for three different cooling scenarios (Fig. 4.4A–4.4C). The timing of the initial burial temperature decline, which is assumed to be driven primarily by regional compression and uplift, was set for 1060, 1050, and

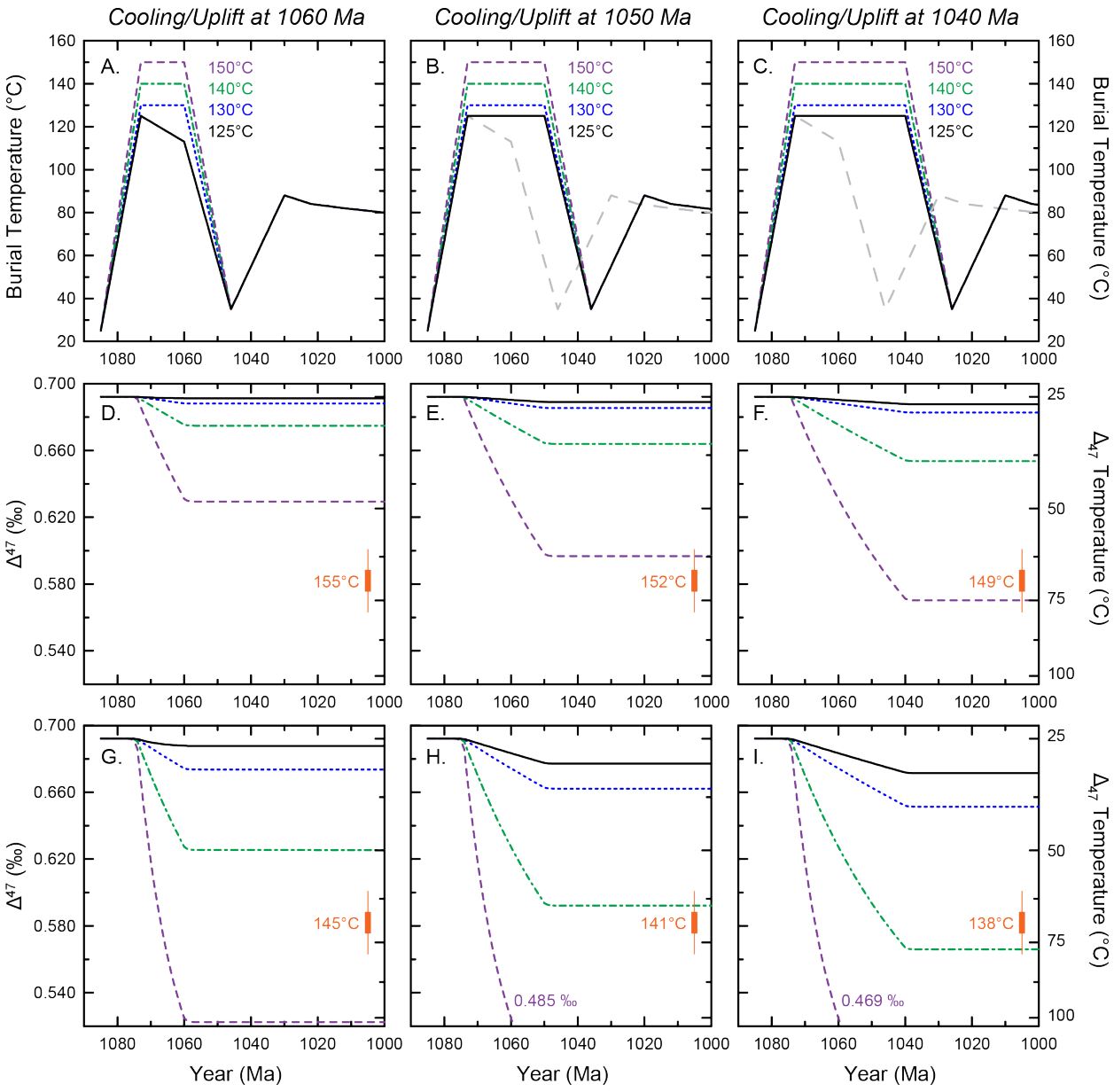

Figure 4.4

Modeled solid-state reordering of clumped isotope values under different burial scenarios using the first-order approximation model (Passey and Henkes, 2012; Henkes et al., 2014). A–C display different maximum burial temperature scenarios assuming uplift and cooling began at (A) 1060, (B) 1050, or (C) 1040 Ma The black line in A corresponds to the best-fit model for the basal Nonesuch from Price, et al. (1996), and is shown for reference as a dashed gray line in the other two uplift scenarios. Reordered Δ_{47} values are shown as forced by the thermal history plotted in the same column. Δ_{47} temperatures are plotted using the theoretical calibration of Schauble et al. (2006). D–F use the optical calcite coefficients, whereas G–I use the brachiopod coefficients. D–I use the same colors and dashes as the corresponding thermal history above. The thick orange vertical line represents the observed range of Δ_{47}values from the sedimentary/early-diagenetic pool, and the thin orange line corresponds to the error window of this sample pool displayed in Figure 3. The orange number corresponds to the maximum burial temperature required to produce a Δ_{47} value within the targeted range.

1040 Ma. 1040 Ma was considered the younger limit for regional uplift based upon the biotite age from Archean basement rocks that was reset at 1060 ± 20 Ma due to regional uplift (Cannon et al. 1993). These scenarios correspond to maximum burial temperature durations of 13, 23, and 33 million years, respectively. Model results using first-order approximation coefficients from both the optical and brachiopod calcite heating experiments are presented in Fig. 4.4.

The modeled scenarios indicate that maximum temperatures between 138 and 155 °C are required to reset the Δ_{47} values to between 0.575–0.588‰. These temperatures are consistent with the maximum burial temperature estimates of Mauk et al. (140–150 °C; 1992), and fall in the middle of the clay thermometry temperature estimates (110–190 °C; 1993). Use of the brachiopod-derived coefficients allows for comparable degrees of resetting at slightly lower temperatures. However, it is unclear which set of coefficients is more appropriate for samples analyzed herein, because the underlying cause of the slight differences in reordering kinetics between optical and brachiopod calcite remains unknown (Henkes et al., 2014).

The modeling results demonstrate that clumped isotope reordering is very sensitive to small differences in maximum burial temperatures between 130 and 150 °C. This observation supports the interpretation of only minor spatial heterogeneity in thermal history along the southeastern arm of the rift. Otherwise, a greater range of Δ_{47} values would be expected within the sedimentary/early-diagenetic calcite sample set. Modeling results further suggest that all of the sedimentary/early-diagenetic samples initially formed at similar temperatures. This assumption was tested by varying the initial clumped isotope temperature between 10 and 30 °C and modeling the reordering using the same thermal scenarios described above. Resulting Δ_{47} values exhibited much greater variability (0.032–0.061‰; Fig. C.1) as compared to the tight

range observed in the samples (0.013‰), which supports the assumption of similar initial temperatures.

The modeling results demonstrate that relatively rapid burial and uplift as suggested by the various radiometric ages is consistent with the clumped isotope data as long as burial temperatures reached maximum temperatures of 140–150 °C. It is difficult to evaluate the relative likelihood of different uplift timing scenarios, due to uncertainty surrounding the different reordering coefficients. The large spread in the clumped isotope temperatures of late-stage veins suggests that these samples have not been reordered and likely reflect different initial formation temperatures. Even if some post-formation reordering occurred, it must have been relatively minor in order to maintain the lower observed temperatures (<50 °C). Emplacement of the veins, therefore, likely occurred after burial temperatures were well below 100 °C.

4.5.2 $\delta^{18}O$ of hydrothermal fluids

Because the clumped isotope composition of carbonate (Δ_{47}) is controlled exclusively by the formation temperature, the $\delta^{18}O$ of the precipitating fluids ($\delta^{18}O_{fl}$) can be calculated using the clumped isotope temperature and the $\delta^{18}O$ of the carbonate ($\delta^{18}O_{carb}$) following the $\delta^{18}O_{carb}$–temperature– $\delta^{18}O_{fl}$ relationships (Ghosh et al., 2006b). Calculated $\delta^{18}O_{fl}$ data can be used to examine the resetting of clumped isotope values further, as well as the origin of the fluids (e.g. meteoric, metamorphic, magmatic) that produced the late-stage veins in the White Pine Mine.

As discussed above, the clumped isotope temperatures of the sedimentary and early-diagenetic calcite samples were likely partially reset through solid-state reordering during burial. If the clumped isotope reordering occurred in the solid state and the there was little to no interaction with a secondary fluid, the bulk $\delta^{18}O_{carb}$ would remain unaffected. Calculating the $\delta^{18}O_{fl}$ using the measured clumped isotope temperatures and the calcite-water fractionation

factor of Friedman and O'Neill (1977) yields values between 1.5 and 3.2‰ (VSMOW) for the sedimentary and early-diagenetic samples (Fig. 4.5A). This range is more positive than would be expected for a lacustrine depositional environment that lacks evidence for significantly evaporative conditions (Elmore et al., 1989). If instead an original formation temperature of 25 °C is used, more reasonable $\delta^{18}O_{fl}$ values for lake water derived from meteoric water are produced (Fig. 4.5B; -6.5 to -4.3‰), supporting the assessment that clumped isotope values were reordered and $\delta^{18}O_{carb}$ values were not affected by later fluid interaction.

Nishioka (1983) originally suggested that meteoric water was the primary source of the fluids that produced the second-stage veins. Mauk et al. (1992b) observed a significant shift in $\delta^{18}O_{carb}$ values from synsedimentary limestone to the calcite veins that could best be explained by as shift in $\delta^{18}O_{fl}$ from approximately -6.4‰ for the limestone to -1.3‰ for the veins. They

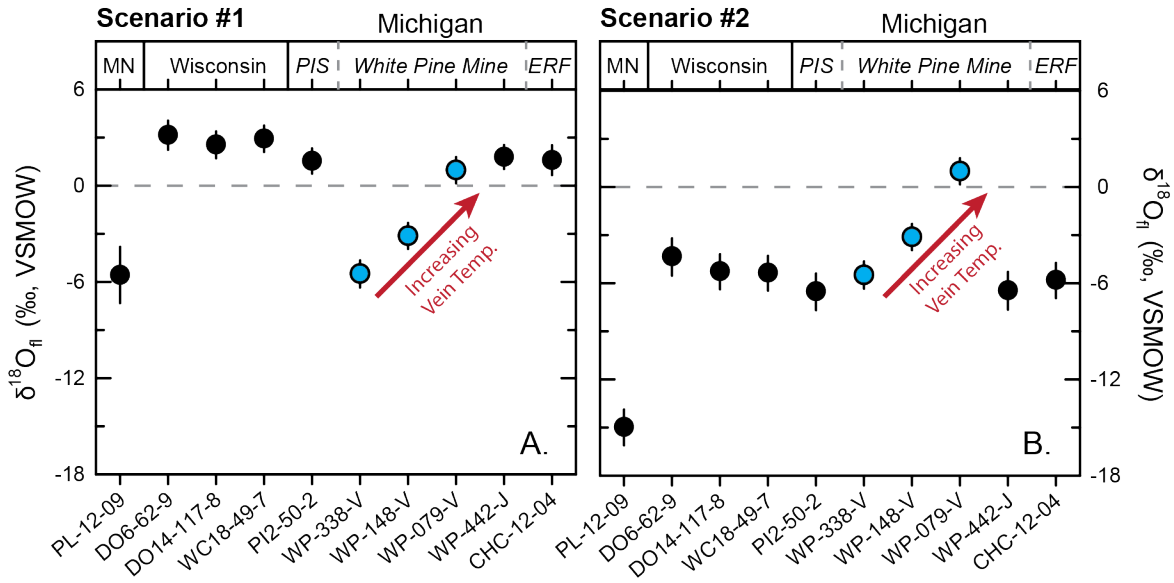

Figure 4.5

Calculated $\delta^{18}O$ values of the precipitating fluids ($\delta^{18}O_{fl}$). A) $\delta^{18}O_{fl}$ calculated assuming that the measured clumped isotope temperature corresponds to the formation temperature. B) $\delta^{18}O_{fl}$ calculated assuming a formation temperature of 25°C (±10°C)for the sedimentary/early-diagenetic calcite samples and using the clumped isotope temperature for the late-stage vein samples. MN – Minnesota; PIS – Presque Isle Syncline; ERF – Eagle River Falls.

interpreted the more ^{18}O-enriched fluid values as a product of greater water-rock interaction. Calculating $\delta^{18}O_{fl}$ values for the late-stage vein samples using the clumped isotope temperatures yields values between -5.5 and 1.0‰, with the more positive values corresponding to hotter temperatures. The new data is broadly similar to the $\delta^{18}O_{fl}$ values estimated by Mauk et al. (1992b), lending support to their interpretation. However, with the data available it is not entirely possible to rule out metamorphic- or magmatic-sourced brines as a fluid source.

4.6. Conclusions

In contrast to previous studies of clay thermometry and bulk organic matter composition, carbonate clumped isotope and organic thermal maturity results indicate a spatially homogenous thermal history within the MRS. Temperatures derived from the clumped isotope composition of sedimentary and early diagenetic calcite samples cluster tightly between 69 and 75 °C. These temperatures likely do not correspond to the original formation temperatures, but were instead elevated to intermediate temperatures due to partial resetting during burial. Modeling results suggest that maximum burial temperatures of 138–155 °C would have been required to reset the clumped isotope composition to this intermediate temperature range, assuming that regional uplift began no later than 1040 Ma. Late-stage calcite veins associated with secondary mineralization within the White Pine Mine display a wide range of clumped isotope temperatures (49–116 °C), likely representing variable hydrothermal fluid activity and also constraining the timing of emplacement to after burial temperatures had fallen below ~100 °C.

Organic thermal maturity results indicate that all samples entered the oil generation window, and did not exhibit significant spatial variability. Organic indicators that are dependent on thermal maturity as well as source composition exhibit more variability, both spatially and within individual cores. Therefore, the previously documented spatial differences in bulk organic

matter composition are more likely a product of variable environmental conditions around the time of deposition and/or early diagenetic preservation of organic matter, rather than a spatially variable thermal history. The relatively low burial temperatures indicated by both the clumped isotope and biomarker data demonstrate that the deposits within the MRS comprise a sedimentary archive that experienced a relatively moderate (<200 °C) thermal history for its age, making it a valuable archive for understanding early Earth environments.

4.7 References

Affek, H.P., and Eiler, J.M., 2006, Abundance of mass 47 CO2 in urban air, car exhaust, and human breath: Geochimica Et Cosmochimica Acta, v. 70, p. 1–12.

Boreham, C.J., Crick, I.H., and Powell, T.G., 1988, Alternative calibration of the methylphenanthrene index against vitrinite reflectance - Application to maturity measurements on oils and sediments: Organic Geochemistry, v. 12, p. 289–294.

Bornhorst, T.J., Paces, J.B., Grant, N.K., Obradovich, J.D., and Huber, N.K., 1988, Age if native copper mineralization, Keweenaw Peninsula, Michigan: Economic Geology, v. 83, p. 619–625.

Bornhorst, T.J., and Williams, W.C., 2013, The Mesoproterozoic Copperwood Sedimentary Rock-Hosted Stratiform Copper Deposit, Upper Peninsula, Michigan: Economic Geology, v. 108, p. 1325–1346.

Bristow, T.F., Bonifacie, M., Derkowski, A., Eiler, J.M., and Grotzinger, J.P., 2011, A hydrothermal origin for isotopically anomalous cap dolostone cements from south China: Nature, v. 474, p. 68–71.

Brocks, J.J., Buick, R., Logan, G.A., and Summons, R.E., 2003, Composition and syngeneity of molecular fossils from the 2.78 to 2.45 billion-year-old Mount Bruce Supergroup, Pilbara Craton, Western Australia: Geochimica Et Cosmochimica Acta, v. 67, p. 4289–4319.

Brocks, J.J., Grosjean, E., and Logan, G.A., 2008, Assessing biomarker syngeneity using branched alkanes with quaternary carbon (BAQCs) and other plastic contaminants: Geochimica Et Cosmochimica Acta, v. 72, p. 871–888.

Brown, A.C., 1971, Zoning in White Pine copper deposit, Ontonagon County, Michigan: Economic Geology, v. 66, p. 543–573.

Cannon, W.F., 1994, Closing of the Midcontinent Rift - a far-field effect of Grenvillian compression: Geology, v. 22, p. 155–158.

Cannon, W.F., Daniels, D.L., Nicholson, S.W., Phillips, J., Woodruff, L.G., Chandler, V.W., Morey, G.B., Boerboom, T., Wirth, K.R., and Mudrey, M.G., 2001, New Map Reveals Origin and Geology of North American Mid-continent Rift: EOS, v. 82, p. 97–112.

Cannon, W.F., Green, A.G., Hutchinson, D.R., Lee, M., Milkereit, B., Behrendt, J.C., Halls, H.C., Green, J.C., Dickas, A.B., Morey, G.B., Sutcliffe, R., and Spencer, C., 1989, The North-American Midcontinent rift beneath Lake Superior from GLIMPCE seismic-reflection profiling: Tectonics, v. 8, p. 305–332.

Cannon, W.F., Peterman, Z.E., and Sims, P.K., 1993, Crustal-scale thrusting and origin of the Montreal River Monoclime - A 35-km-thick cross-section of the Midcontinent Rift in Northern Michigan and Wisconsin: Tectonics, v. 12, p. 728–744.

Chen, J.H., Fu, J.M., Sheng, G.Y., Liu, D.H., and Zhang, J.J., 1996, Diamondoid hydrocarbon ratios: Novel maturity indices for highly mature crude oils: Organic Geochemistry, v. 25, p. 179–190.

Craddock, J.P., Konstantinou, A., Vervoort, J.D., Wirth, K.R., Davidson, C., Finley-Blasi, L., Juda, N.A., and Walker, E., 2013, Detrital Zircon Provenance of the Mesoproterozoic Midcontinent Rift, Lake Superior Region, U.S.A. (vol 121, pg 57, 2013): Journal of Geology, v. 121, p. 307–308.

Cumming, V.M., Poulton, S.W., Rooney, A.D., and Selby, D., 2013, Anoxia in the terrestrial environment during the late Mesoproterozoic: Geology, v. 41, p. 583–586.

Daniels, P.A., 1982, Upper Precambrian sedimentary rocks - Oronto Group, Michigan-Wisconsin: Geological Society of America Memoirs, v. 156, p. 107–133.

Davis, D.W., and Green, J.C., 1997, Geochronology of the North American Midcontinent rift in western Lake Superior and implications for its geodynamic evolution: Canadian Journal of Earth Sciences, v. 34, p. 476–488.

Davis, D.W., and Paces, J.B., 1990, Time resolution of geologic events on the Keweenaw Peninsula and implications for development of the Midcontinent Rift System: Earth and Planetary Science Letters, v. 97, p. 54–64.

Defliese, W.F., Hren, M.T., and Lohmann, K.C., 2015, Compositional and temperature effects of phosphoric acid fractionation on Δ_{47} analysis and implications for discrepant calibrations: Chemical Geology, v. 396, p. 51–60.

Eglinton, G., Burlingame, A.L., Belsky, T., Scott, P.M., and Calvin, M., 1964, Hydrocarbons of biological origin from 1-billion-year-old-sediment: Science, v. 145, p. 263–264.

Eiler, J.M., 2011, Paleoclimate reconstruction using carbonate clumped isotope thermometry: Quaternary Science Reviews, v. 30, p. 3575–3588.

Elmore, R.D., 1983, Precambrian non-marine stromatolites in alluvial-fan deposits, the Copper Harbor Conglomerate, Upper Michigan: Sedimentology, v. 30, p. 829–842.

Elmore, R.D., 1984, The Copper Harbor Conglomerate - a Late Precambrian fining-upward alluvial-fan sequence in northern Michigan: Geological Society of America Bulletin, v. 95, p. 610–617.

Elmore, R.D., Milavec, G.J., Imbus, S.W., and Engel, M.H., 1989, The Precambrian Nonesuch Formation of the North-American Mid-Continent Rift, sedimentology and organic geochemical aspects of lacustrine deposition: Precambrian Research, v. 43, p. 191–213.

Essene, E.J., and Peacor, D.R., 1995, Clay mineral thermometry - A critical perspective: Clays and Clay Minerals, v. 43, p. 540–553.

Fernandez, A., Tang, J., and Rosenheim, B.E., 2014, Siderite 'clumped' isotope thermometry: A new paleoclimate proxy for humid continental environments: Geochimica Et Cosmochimica Acta, v. 126, p. 411–421.

Ferry, J.M., Passey, B.H., Vasconcelos, C., and Eiler, J.M., 2011, Formation of dolomite at 40-80 degrees C in the Latemar carbonate buildup, Dolomites, Italy, from clumped isotope thermometry: Geology, v. 39, p. 571–574.

Ghosh, P., Adkins, J., Affek, H., Balta, B., Guo, W.F., Schauble, E.A., Schrag, D., and Eller, J.M., 2006, ^{13}C-^{18}O bonds in carbonate minerals: A new kind of paleothermometer: Geochimica Et Cosmochimica Acta, v. 70, p. 1439–1456.

Ghosh, P., Eiler, J., Campana, S.E., and Feeney, R.F., 2007, Calibration of the carbonate 'clumped isotope' paleothermometer for otoliths: Geochimica Et Cosmochimica Acta, v. 71, p. 2736–2744.

Grantham, P.J., 1986, Sterane isomerization and moretane hopane ratios in crude oils derived from tertiary source rocks: Organic Geochemistry, v. 9, p. 293–304.

Halls, H.C., and Pesonen, L.J., 1982, Paleomagnetism of Keweenawan rocks: Geological Society of America Memoirs, v. 156, p. 173–201.

Henkes, G.A., Passey, B.H., Grossman, E.L., Shenton, B.J., Perez-Huerta, A., and Yancey, T.E., 2014, Temperature limits for preservation of primary calcite clumped isotope paleotemperatures: Geochimica Et Cosmochimica Acta, v. 139, p. 362–382.

Hieshima, G.B., and Pratt, L.M., 1991, Sulfur carbon ratios and extractable organic-matter of the Middle Proterozoic Nonesuch Formation, North-American Midcontinent Rift: Precambrian Research, v. 54, p. 65–79.

Ho, E.S., and Mauk, J.L., 1996, Relationship between organic matter and copper mineralization in the Proterozoic Nonesuch Formation, northern Michigan: Ore Geology Reviews, v. 11, p. 71–87.

Hoffman, J., and Hower, J., 1979, Clay mineral assemblages as low grade metamorphic geothermometers: application to the thrust faulted disturbed belt of Montana, U.S.A.: SEPM Special Publication No. 26, p. 55–79.

Hower, J., Eslinger, E.V., Hower, M.E., and Perry, E.A., 1976, Mechanism of burial metamorphism of argillaceous sediment: 1. Mineralogical and chemical evidence: Geological Society of America Bulletin, v. 87, p. 725–737.

Hren, M.T., Sheldon, N.D., Grimes, S.T., Collinson, M.E., Hooker, J.J., Bugler, M., and Lohmann, K.C., 2013, Terrestrial cooling in Northern Europe during the Eocene-Oligocene transition: Proceedings of the National Academy of Sciences of the United States of America, v. 110, p. 7562–7567.

Huntington, K.W., Budd, D.A., Wernicke, B.P., and Eiler, J.M., 2011, Use of clumped-isotope thermometry to constrain the crystallization temperature of diagenetic calcite: Journal of Sedimentary Research, v. 81, p. 656–669.

Huntington, K.W., Eiler, J.M., Affek, H.P., Guo, W., Bonifacie, M., Yeung, L.Y., Thiagarajan, N., Passey, B., Tripati, A., Daeron, M., and Came, R., 2009, Methods and limitations of 'clumped' CO(2) isotope (Delta(47)) analysis by gas-source isotope ratio mass spectrometry: Journal of Mass Spectrometry, v. 44, p. 1318–1329.

Imbus, S.W., Engel, M.H., Elmore, R.D., and Zumberge, J.E., 1988, The origin, distribution and hydrocarbon generation potential of organic-rich facies in teh Nonesuch Formation, Central North American Rift System - A regional study: Organic Geochemistry, v. 13, p. 207–219.

Imbus, S.W., Macko, S.A., Elmore, R.D., and Engel, M.H., 1992, Stable isotope (C, S, N) and molecular studies on the Precambrian Nonesuch Shale (Wisconsin-Michigan, USA) - Evidence for differential preservation rates, depositional environment and hydrothermal influence: Chemical Geology, v. 101, p. 255–281.

Jarrett, A.J.M., Schinteie, R., Hope, J.M., and Brocks, J.J., 2013, Micro-ablation, a new technique to remove drilling fluids and other contaminants from fragmented and fissile rock material: Organic Geochemistry, v. 61, p. 57–65.

Jolly, W.T., 1974, Behavior of Cu, Zn, and NI during Prehnite-Pumpellyite rank metamorphism of Keweenawan Basalts, Northern Michigan: Economic Geology, v. 69, p. 1118–1125.

Kalliokoski, J., 1982, Jacobsville sandstone: Geological Society of America Memoirs, v. 156, p. 147–155.

Kluge, T., John, C.M., Jourdan, A.L., Davis, S., and Crawshaw, J., 2015, Laboratory calibration of the calcium carbonate clumped isotope thermometer in the 25-250 degrees C temperature range: Geochimica et Cosmochimica Acta, v. 157, p. 213–227.

Levandowski, W., Boyd, O.S., Briggs, R.W., and Gold, R.D., 2015, A random-walk algorithm for modeling lithospheric density and the role of body forces in the evolution of the Midcontinent Rift: Geochemistry Geophysics Geosystems, v. 16, p. 4084–4107.

Mackenzie, A.S., Patience, R.L., Maxwell, J.R., Vandenbroucke, M., and Durand, B., 1980, Molecular-parameters of maturation in the Toarcian Shales, Paris Basin, France 1.

Changes in the configurations of acyclic isoprenoid alkanes, steranes, and triterpanes: Geochimica Et Cosmochimica Acta, v. 44, p. 1709–1721.

Malone, D.H., Stein, C.A., Craddock, J.P., Kley, J., Stein, S., and Malone, J.E., 2016, Maximum deposition age of the Neoproterozoic Jacobsville Sandstone, Michigan: implicatons for the evolution of the Midecontinent Rift: Geosphere, v. 12, p. 1–12

Mauk, J.L., and Hieshima, G.B., 1992, Organic-matter adn copper mineralization at White-Pine, Michigan, USA: Chemical Geology, v. 99, p. 189–211.

Mauk, J.L., Kelly, W.C., Vanderpluijm, B.A., and Seasor, R.W., 1992, Relations between deformation and sediment-hosted copper mineralization - evidence from the White-Pine of the Midcontinent Rift System: Geology, v. 20, p. 427–430.

Meinschein, W.G., Schopf, J.W., and Barghoorn, E.S., 1964, Biological remnants in Precambrian sediment: Science, v. 145, p. 262–263.

Mitchell, R.L., and Sheldon, N.D., 2009, Weathering and paleosol formation in the 1.1 Ga Keweenawan Rift: Precambrian Research, v. 168, p. 271–283.

Mitchell, R.L., and Sheldon, N.D., 2010, The similar to 1100 Ma Sturgeon Falls paleosol revisited: Implications for Mesoproterozoic weathering environments and atmospheric CO(2) levels: Precambrian Research, v. 183, p. 738–748.

Mitchell, R.L., and Sheldon, N.D., 2016, Sedimentary provenance and weathering processes in the 1.1 Ga Midcontinental Rift of the Keweenaw Peninsula, Michigan, USA: Precambrian Research, v. 275, p. 225–240.

Morey, G.B., and Green, J.C., 1982, Status of the Keweenawan as a stratigraphic unit in the Lake Superior region, *in* Wold, R.J., and Hinze, W.J., eds., Geology and Tectonics of the Lake Superior Basin, Volume 156, Geological Society of America Memoir, p. 15–25.

Morey, G.B., and Ojakangas, R.W., 1982, Keweenawan sedimentary-rocks of eastern Minnesota and northwestern Wisconsin: Geological Society of America Memoirs, v. 156, p. 135–146.

Nicholson, S.W., Shirey, S.B., Schulz, K.J., and Green, J.C., 1997, Rift-wide correlation of 1.1 Ga midcontinent rift system basalts: Implications for multiple mantle sources during rift development: Canadian Journal of Earth Sciences, v. 34, p. 504–520.

Nishioka, G.K., 1983, Origin of late veins in the White Pine copper deposit, northern Michigan, M.S. Tesis, University of Michigan, Ann Arbor.

Ohr, M., 1993, Geochronology of diagenesis and low-grade metamorphism in pelites: Ann Arbor, Ph.D. Dissertation, University of Michigan.

Ojakangas, R.W., and Dickas, A.B., 2002, The 1.1-Ga Midcontinent Rift System, central North America: sedimentology of two deep boreholes, Lake Superior region: Sedimentary Geology, v. 147, p. 13–36.

Ojakangas, R.W., and Morey, G.B., 1982, Keweenawan sedimentary-rocks of the Lake-Superior Region - A summary: Geological Society of America Memoirs, v. 156, p. 157–164.

Ojakangas, R.W., Morey, G.B., and Green, J.C., 2001, The Mesoproterozoic Midcontinent Rift System, Lake Superior Region, USA: Sedimentary Geology, v. 141, p. 421–442.

Paces, J.B., and Miller, J.D., 1993, Precise U-Pb ages of Duluth complex and related mafic intrusions, Northeastern Minnesota - Geochronological insights to physical, petrogenetic, paleomagnetic, adn tectonomagnetic processes associated with the 1.1 Ga Midcontinent Rift: Journal of Geophysical Research-Solid Earth, v. 98, p. 13997–14013.

Passey, B.H., and Henkes, G.A., 2012, Carbonate clumped isotope bond reordering and geospeedometry: Earth and Planetary Science Letters, v. 351, p. 223–236.

Passey, B.H., Levin, N.E., Cerling, T.E., Brown, F.H., and Eiler, J.M., 2010, High-temperature environments of human evolution in East Africa based on bond ordering in paleosol carbonates: Proceedings of the National Academy of Sciences of the United States of America, v. 107, p. 11245–11249.

Peters, K.E., Walters, C.C., and Moldowan, J.M., 2005, The Biomarker Guide: Cambridge, Cambridge University Press, 704 p.

Petersen, S.V., Winkelstern, I.Z., Lohmann, K.C., and Meyer, K.W., 2016, The effects of Porapak (TM) trap temperature on delta O-18, delta C-13, and Delta(47) values in preparing samples for clumped isotope analysis: Rapid Communications in Mass Spectrometry, v. 30, p. 199–208.

Pratt, L.M., Summons, R.E., and Hieshima, G.B., 1991, Sterane and triterpane biomarkers in the Precambrian Nonesuch Formation, North-American Midcontinent Rift: Geochimica Et Cosmochimica Acta, v. 55, p. 911–916.

Price, K.L., Huntoon, J.E., and McDowell, S.D., 1996, Thermal history of the 1.1-Ga Nonesuch Formation, North American mid-continent rift, White Pine, Michigan: Aapg Bulletin-American Association of Petroleum Geologists, v. 80, p. 1–15.

Price, K.L., and McDowell, S.D., 1993, Illite-smectite geothermometry of the proterozoic Oronto Group, Midcontinent Rift System: Clays and Clay Minerals, v. 41, p. 134–147.

Radke, M., and Welte, D.H., 1983, The MethylphenanthreneIndex (MPI): A maturity parameter based on aromatic hydrocarbons, Advances in Organic Geochemistry, Wiley and Sons, p. 504–512.

Ruiz, J., Jones, L.M., and Kelly, W.C., 1984, Rubidium-Strontium dating of ore-deposits hosted by Rb-rich rocks, using calcite and other common Sr-bearing minerals: Geology, v. 12, p. 259–262.

Schauble, E.A., Ghosh, P., and Eiler, J.M., 2006, Preferential formation of C-13-O-18 bonds in carbonate minerals, estimated using first-principles lattice dynamics: Geochimica Et Cosmochimica Acta, v. 70, p. 2510–2529.

Seifert, W.K., and Moldowan, J.M., 1980, The effect of thermal stress on source-rock quality as measured by hopane stereochemistry: Physics and Chemistry of the Earth, v. 12, p. 229–237.

Sheldon, N.D., 2012, Microbially induced sedimentary structures in non-marine sediments from the ~1100 Ma old Mid-Continent Rift of North America, *in* Noffke, N., and Chafetz, H., eds., Microbial Mats in Siliciclastic Systems Through Time: SEPM Special Publication 101, p. 153–162.

Sheldon, N.D., 2013, Causes and consequences of low atmospheric pCO(2) in the Late Mesoproterozoic: Chemical Geology, v. 362, p. 224–231.

Shenton, B.J., Grossman, E.L., Passey, B.H., Henkes, G.A., Becker, T.P., Laya, J.C., Perez-Huerta, A., Becker, S.P., and Lawson, M., 2015, Clumped isotope thermometry in deeply buried sedimentary carbonates: The effects of bond reordering and recrystallization: Geological Society of America Bulletin, v. 127, p. 1036–1051.

Stein, C.A., Kley, J., Stein, S., Hindle, D., and Keller, G.R., 2015, North America's Midcontinent Rift: When rift met LIP: Geosphere, v. 11, p. 1607–1616.

Stein, C.A., Stein, S., Merino, M., Keller, G.R., Flesch, L.M., and Jurdy, D.M., 2014, Was the Midcontinent Rift part of a successful seafloor- spreading episode?: Geophysical Research Letters, v. 41, p. 1465–1470.

Stolper, D.A., and Eiler, J.M., 2015, The kinetics of solid-state isotope-exchange reactions for clumped isotopes: A study of inorganic calcites and apatites from natural and experimental samples: American Journal of Science, v. 315, p. 363–411.

Strother, P.K., and Wellman, C.H., 2016, Palaeoecology of a billion-year-old non-marine cyanobacterium from teh Torridon Group and Nonesuch Formation: Palaeontology, v. 59, p. 89–108.

Swanson-Hysell, N.L., Burgess, S.D., Maloof, A.C., and Bowring, S.A., 2014, Magmatic activity and plate motion during the latent stage of Midcontinent Rift development: Geology, v. 42, p. 475–478.

Wellman, C.H., and Strother, P.K., 2015, The terrestrial biota prior to the origin of land plants (embryophytes): a review of the evidence: Palaeontology, v. 58, p. 601–627.

White, W.S., 1968, The native copper deposits of northern Michigan, *in* Ridge, J.D., ed., Ore deposits of the United States 1933-1967, Volume 1: New York, American Institutes of Mining, Metallurgical and Petroleum Engineers, p. 303–325.

White, W.S., 1970, A paleohydrologic model for mineralization of White Pine copper deposit, Northern Michigan: Economic Geology, v. 65, p. 1–13.

White, W.S., and Wright, J.C., 1960, Lithofacies of the Copper Harbor Conglomerate, Northern Michigan: US Geological Survey Professional Paper, v. 400, p. B5–B8.

Wilmeth, D.T., Dornbos, S.Q., Isbell, J.L., and Czaja, A.D., 2014, Putative domal microbial structures in fluvial siliciclastic facies of the Mesoproterozoic (1.09 Ga) Copper Harbor Conglomerate, Upper Peninsula of Michigan, USA: Geobiology, v. 12, p. 99–108.

Zartman, R.E., Nicholson, S.W., Cannon, W.F., and Morey, G.B., 1997, U-Th-Ph zircon ages of some Keweenawan supergroup rocks from the south shore of Lake Superior: Canadian Journal of Earth Sciences, v. 34, p. 549–561.

Zbinden, E.A., Holland, H.D., Feakes, C.R., and Dobos, S.K., 1988, The Sturgeon Falls paleosol and the composition of the atmosphere, 1.1 Ga BP: Precambrian Research, v. 42, p. 141–163.

CHAPTER 5

Conclusions

5.1 Summary of results

Pedogenic carbonate is relatively abundant in the geologic record and can provide insight into many questions regarding paleoclimate, paleobiology, and paleoelevation. Geologic applications of pedogenic carbonate preserved in paleosols have proliferated; however, these applications are somewhat limited by uncertainty that persists around the nature of pedogenic carbonate formation. A number of environmental variables that are reconstructed from pedogenic carbonate exhibit significant seasonal variations throughout the year, including temperature, soil pCO_2, and soil water $\delta^{18}O$ (Breecker et al., 2009). Therefore, an accurate understanding of the seasonal timing of pedogenic carbonate formation is required in order to improve environmental reconstructions.

In **Chapter 2**, I determined clumped isotope temperatures for pedogenic carbonate sampled from modern soils that formed under four distinct precipitation regimes. Clumped isotope temperatures derived from these samples were within error or slightly below mean annual air temperature (MAAT) at sites from three of the four precipitation regimes. Only the relatively wet, continental climate regime produced temperatures well above MAAT. These results illustrate that a warm-season formation bias cannot always be assumed.

I used a soil water balance model to predict the seasonal timing of soil water depletion in each of the sampled soils. Modeled soil temperatures at the time of soil water depletion generally agree with the clumped isotope temperatures, indicating that fluctuations in soil moisture exert a control on the timing of pedogenic carbonate formation. Soil water $\delta^{18}O$ values calculated from the clumped isotope temperature and the $\delta^{18}O$ value of the carbonate most closely reflect the isotopic composition of precipitation during the month of soil water depletion, further supporting the conclusion that pedogenic carbonate forms when the soil begins to dry out.

To gain an improved understanding of temperature biases that are likely imparted on pedogenic carbonate and other paleosol temperature proxies, I compiled soil moisture and temperature data from the Soil Climate Analysis Network in **Chapter 3**. It was shown that soil temperature seasonality was significantly reduced as compared to air temperature fluctuations at sites where cold month temperatures fell below freezing, likely due to snow insulation and latent heat exchange during the freezing and thawing of H_2O. These cold season temperatures produce mean annual soil temperature well above MAAT.

Using the SCAN data, I evaluated two different soil moisture scenarios to predict the time of the year during which pedogenic carbonate is most likely to form and constrain what temperature biases relative to MAAT would be expected. If pedogenic carbonate is most likely to form during the absolute driest point of the year, a systematic cold bias would be expected. However, a warm temperature bias would be more likely if pedogenic carbonate formation is better predicted by the largest seasonal decline in soil moisture. The latter scenario appears more likely due to comparison with previously published clumped isotope measurements. The exact magnitude of the warm bias is difficult to predict, although temperatures greater than 12–14 °C are considered unlikely at depths below 50 cm in soils.

Beyond uncertainties surrounding the formation of pedogenic carbonate, studies that aim to reconstruct environmental conditions from paleosols, and terrestrial systems in general, must always attempt to constrain post-depositional alteration. Solid state reordering of carbonate clumped isotopes during burial is of particular concern for paleosol carbonate samples (Quade et al., 2013). In **Chapter 4**, I evaluated post-depositional alteration of continental deposits from the Midcontinent Rift System (MRS) of North America. These rocks were deposited at approximately 1.1 Ga and comprise an important archive of terrestrial life and environments; however, accurate environmental reconstructions depend on a well-constrained post-depositional history.

Clumped isotope analyses of three different generations of calcite were combined with organic thermal maturity data to refine the thermal history of the MRS. Clumped isotope values from sedimentary and early-diagenetic samples were partially reset to elevated temperatures between 68 and 75 °C. Solid-state reordering models indicate that temperatures between 138 and 155 °C over a 13 to 33 million year period would have been required to reset the temperatures into the observed range. This data is consistent with independent analyses of organic thermal maturity, which also both indicate that there were not significant spatial differences in the regional thermal history.

5.2 Future research directions

5.2.1 An improved, process-based understanding of pedogenic carbonate formation

The clumped isotope data presented in **Chapter 2** and the soil instrumental data presented in **Chapter 3** together demonstrate that pedogenic carbonate form during different seasons under different climate regimes. Potentially, the seasonal timing of carbonate formation

may even occur during different seasons at various depths within the same soil. This seasonal variability makes the magnitude of temperature bias recorded by paleosol carbonate is difficult to predict. Despite decades of research, a complete, process-based understanding of the factors that control pedogenic carbonate formation is still lacking and is required to improve its utility as a paleoclimate archive. Furthermore, fundamental questions remain about the carbon isotopic fractionations between soil CO_2 and pedogenic carbonate. A general range of (14–17 ‰) is assumed to represent equilibrium (Cerling et al., 1989; Cerling and Quade, 1993); however, the exact processes and their respective magnitudes remain uncertain (Monger et al., 2009).

One of the most difficult aspects of studying pedogenic carbonate formation in modern soils is its long formation time. Pedogenic carbonate tends to only accumulate in sizable quantities in soils after hundreds of years, and most soils with well-developed carbonate horizons have been developing for hundreds to thousands of years at minimum (Gile et al., 1966). The long formation time increases the uncertainty that modern soil environmental conditions adequately reflect the mean conditions that pedogenic carbonate experienced throughout its entire formation history. Another complication is that short-term soil instrumental records potentially do not capture normal recent soil environmental conditions, especially with modern climate change rapidly changing regional hydrology.

Investigations that take an experimental approach towards understanding the seasonal controls on pedogenic carbonate may be able to avoid some of these complicating factors. A research approach that combines experimental soil manipulation and computer modeling has the potential to develop a more complete, process-based understanding of pedogenic carbonate formation. If an improved understanding of the factors controlling pedogenic carbonate formation can be developed and the primary factors identified, the possibility exists that

paleoclimate model data may be used to help understand the seasonal formation processes in paleo-applications.

5.2.2 Effect of soil texture on pedogenic carbonate formation

As demonstrated in **Chapter 2**, as well as other studies (Hough et al., 2014; Burgener et al., 2016), soil moisture can exert a control on the seasonal timing of pedogenic carbonate formation. Soil texture also plays an important role in soil moisture dynamics as it affects the water holding capacity of soils as well as the rate of infiltration. Therefore, it is important to understand the effect of soil texture on the geochemistry of pedogenic carbonate. Understanding the role of soil texture is especially important in arid settings, where finer grained soils with slow infiltration rates may lose more water to evaporation (Noy-Meir, 1973). The ^{18}O-enriched soil water values from the two poorly drained soils in **Chapter 2** underscore the potentially sizeable effect that slower infiltration can have on the isotopic composition of pedogenic carbonate.

Texture also shapes the nature of pedogenic carbonate formation in soils. Coarse-grained soils generally accumulate carbonate as coatings on the undersides of large clasts, whereas fine-grained soils will tend to form nodular carbonate (Gile et al., 1966). Because of the hydrologic difference between the two textural end members, there is reason to suspect that they might form during different seasons, and thereby record different temperature biases. The majority of clumped isotope studies of carbonate in modern soils have focused primarily on clast undercoatings (Quade et al., 2013; Peters et al., 2013; Hough et al., 2014; Ringham et al., 2016; Burgener et al., 2016). More work needs to be done focusing on nodule-bearing soils to ensure that the colder-nature of the results presented on nodular carbonate in **Chapter 2** are indeed a function of climatic differences and not texture.

Oerter and Amundson (2016) analyzed undercoatings and filamentous carbonate from the within the same soils, and documented differences between the two types of carbonate within some soils but not others. Future work should attempt to target nodular bearing soils that are fairly close to coarser-grained soils that can be analyzed and compared. Paleo-studies should also be aware of changes in texture within stacked sequences of paleosols to make sure that any observed shifts in temperatures are a product of actual environmental change and are not forced by texturally-induced changes in soil hydrology.

5.2.3 Partial resetting of clumped isotopes in pedogenic carbonate

One of the greatest challenges facing applications of clumped isotope thermometry to pedogenic carbonate preserved in paleosols is assessing if samples have been reordered to hotter temperatures during burial. Because this process does not require fluid interaction or recrystallization (Passey and Henkes, 2012), it can be difficult to detect in samples where temperatures are still plausible for the Earth's surface (e.g. a sample that formed at 10 °C but was reordered to 30 °C). Evidence for partial reordering of paleosol carbonates was documented at relatively shallow burial depths of only 2−4 km (Quade et al., 2013). Further concern is raised by the modeling results of Stolper and Eiler (2015), which suggest that partial reordering of ~10 °C may be possible even in situations where burial temperatures remain below 100 °C.

Improved means of assessing solid-state reordering will allow for greater confidence in the fidelity of temperature reconstructions derived from the clumped isotope composition of paleosol carbonate. Electron backscatter diffraction has been suggested as a possible technique to help detect the occurrence of reordering processes in calcite (Henkes et al., 2014); however, the effectiveness of this approach remains to be evaluated. It should be noted that certain types of

carbonate, such as micritic limestone, are potentially more easily reset to elevated temperatures than optical or shell calcite (Winkelstern et al., 2016). It is possible that pedogenic carbonate, which can forms as diffuse, poorly-crystalline filaments (Gile et al., 1966), may also be more susceptible to reordering or potentially even minor recrystallization during early burial.

The upper threshold of a 12–14 °C bias above MAAT proposed in **Chapter 4** provides some guidance when evaluating if the clumped isotope composition of paleosol carbonate samples are pristine. In some circumstances, clumped isotope temperatures may be combined with independent proxies that reconstruct MAAT, such as plant fossils (e.g. Snell et al., 2013), to assess if reconstructed temperature seasonality values are plausible (e.g. < 12–14 °C). However, more direct methods for constraining solid state reordering are needed to increase the confidence of temperature reconstructions.

5.3 References

Breecker, D.O., Sharp, Z.D., and McFadden, L.D., 2009, Seasonal bias in the formation and stable isotopic composition of pedogenic carbonate in modem soils from central New Mexico, USA: Geological Society of America Bulletin, v. 121, p. 630-640.

Burgener, L., Huntington, K.W., Hoke, G.D., Schauer, A., Ringham, M.C., Latorre, C., and Diaz, F.P., 2016, Variations in soil carbonate formation and seasonal bias over > 4 km of relief in the western Andes (30 degrees S) revealed by clumped isotope thermometry: Earth and Planetary Science Letters, v. 441, p. 188-199.

Cerling, T.E., and Quade, J., 1993, Stable Carbon and Oxygen Isotopes in Soil Carbonates, *in* Swart, P.K., Lohmann, K.C., Mckenzie, J., and Savin, S., eds., Climate Change in Continental Isotopic Records, Volume 78: Geophysical Monograph, American Geophysical Union Geophysical Monograph, p. 217-231.

Cerling, T.E., Quade, J., Wang, Y., and Bowman, J.R., 1989, Carbon isotopes in soils and paleosols as ecology and paleoecology indicators: Nature, v. 341, p. 138-139.

Gile, L.H., Peterson, F.F., and Grossman, R.B., 1966, Morphological and genetic sequences of carbonate accumulation in desert soils: Soil Science, v. 101, p. 347-360.

Henkes, G.A., Passey, B.H., Grossman, E.L., Shenton, B.J., Perez-Huerta, A., and Yancey, T.E., 2014, Temperature limits for preservation of primary calcite clumped isotope paleotemperatures: Geochimica Et Cosmochimica Acta, v. 139, p. 362-382.

Hough, B.G., Fan, M., and Passey, B.H., 2014, Calibration of the clumped isotope geothermometer in soil carbonate in Wyoming and Nebraska, USA: Implications for paleoelevation and paleoclimate reconstruction: Earth and Planetary Science Letters, v. 391, p. 110-120.

Monger, H.C., Cole, D.R., Buck, B.J., and Gallegos, R.A., 2009, Scale and the isotopic record of C-4 plants in pedogenic carbonate: from the biome to the rhizosphere: Ecology, v. 90, p. 1498-1511.

Noy-Meir, I., 1973, Desert ecosystems: environment and producers: Annual Review of Ecology and Systematics, v. 4, p. 25-51.

Oerter, E.J., and Amundson, R., 2016, Climate controls on spatial and temporal variations in the formation of pedogenic carbonate in the western Great Basin of North America: Geological Society of America Bulletin, v. 128, p. 1095-1104.

Passey, B.H., and Henkes, G.A., 2012, Carbonate clumped isotope bond reordering and geospeedometry: Earth and Planetary Science Letters, v. 351, p. 223-236.

Peters, N.A., Huntington, K.W., and Hoke, G.D., 2013, Hot or not? Impact of seasonally variable soil carbonate formation on paleotemperature and O-isotope records from clumped isotope thermometry: Earth and Planetary Science Letters, v. 361, p. 208-218.

Quade, J., Eiler, J., Daeron, M., and Achyuthan, H., 2013, The clumped isotope geothermometer in soil and paleosol carbonate: Geochimica Et Cosmochimica Acta, v. 105, p. 92-107.

Ringham, M.C., Hoke, G.D., Huntington, K.W., and Aranibar, J.N., 2016, Influence of vegetation type and site-to-site variability on soil carbonate clumped isotope records, Andean piedmont of Central Argentina (32-34°S): Earth and Planetary Science Letters, v. 440, p. 1-11.

Snell, K.E., Thrasher, B.L., Eiler, J.M., Koch, P.L., Sloan, L.C., and Tabor, N.J., 2013, Hot summers in the Bighorn Basin during the early Paleogene: Geology, v. 41, p. 55-58.

Stolper, D.A., and Eiler, J.M., 2015, The kinetics of solid-state isotope-exchange reactions for clumped isotopes: A study of inorganic calcites and apatites from natural and experimental samples: American Journal of Science, v. 315, p. 363-411.

Winkelstern, I.Z., and Lohmann, K.C., 2016, Shallow burial alteration of dolomite and limestone clumped isotope geochemistry: Geology, v. 44, p. 467-470.

Appendix A

Supplemental Figures and Data for Chapter 2

Table A.1 Sites and corresponding climate station information

Site/Soil	Station Name	Location		Elevation
		N (°)	W (°)	(m)
Muroc[a]	Mojave, CA US	35.049	118.162	834
Lavic[a]	El Mirage, CA US	34.589	117.630	899
Guvo	Arizona City, AZ US	32.731	111.692	465
Cross-Apache	Seligman, AZ US	35.332	112.880	1600
Cornville	Montezuma Castle NM, AZ US	34.611	111.838	969
Plughat	Des Moines, NM US	36.750	103.833	2018
Montecito	Taos, NM US	36.391	105.586	2123
Witt[b]	Mountainair 8 NW, NM US	34.624	106.310	2014
	Mountainair, NM US	34.521	106.261	1987
Kranzburg	Mitchell Municipal Airport, SD US	43.774	98.038	396
Clamo	Brookings 2 NE, SD US	44.325	96.769	497
Eros	Sioux Falls 14 NNE, SD US	43.735	96.622	486
Adams Ranch[c]	Corona Lincoln Compressor Station, NM US	34.100	105.683	1981
	Corona 10 SW, NM US	34.149	105.698	2036

[a]These samples were collected from the California "Soil Series Pedolarium," and the GPS coordinates given are for the type location of the soil series.
[b]Mountainair 8 NW was the closest climate station to the Witt site, but only had temperature data, so precipitation data was taken from the Mountainair station.
[c]Corona Lincoln Compressor Station was the closest climate station to the Adams Ranch site, but only had temperature data, so precipitation data was taken from the Corona 10 SW station.

Table A.2 Soil thermal properties

Site/Soil	κ (W/K/m)[a]	C_v ($J/m^3/K$)[b]	d (cm)[c]
Muroc	0.57	1.38	204
Lavic	0.85	1.2	267
Guvo	0.52	1.31	200
Cross-Apache	1.09	1.98	235
Cornville	0.52	2.01	161
Plughat	1.09	1.98	235
Montecito	1.08	2.23	220
Witt	1.09	1.98	235
Kranzburg	1.09	1.98	235
Clamo	1.09	1.98	235
Eros	1.09	1.98	235
Adams Ranch	0.52	2.01	161

[a]Thermal conductivity; data from Shukla (2014)
[b]Volumetric heat capacity; data from Shukla (2014)
[c]Damping depth

Table A.3 Summary of evapotranspiration and soil water balance calculations

Site	Month	ET_0 (cm)	ET_0' (cm)[a]	Precip (cm)	P-ET0 (cm)	Soil Water Storage (cm)
Muroc	Jan	2.2	2.2	3.0	0.9	1.0
	Feb	4.5	4.5	3.9	-0.6	0.4
	Mar	9.5	9.5	2.5	-7.1	0.0
	Apr	13.9	13.9	0.6	-13.3	0.0
	May	20.2	20.2	0.3	-20.0	0.0
	Jun	24.5	24.5	0.1	-24.4	0.0
	Jul	27.5	27.5	0.8	-26.7	0.0
	Aug	25.2	25.2	0.7	-24.5	0.0
	Sep	17.6	17.6	0.4	-17.2	0.0
	Oct	9.9	9.9	0.9	-8.9	0.0
	Nov	4.7	4.7	1.5	-3.1	0.0
	Dec	2.1	2.1	2.3	0.1	0.1
Lavic	Jan	2.2	2.2	2.6	0.4	0.1
	Feb	4.6	4.6	2.7	-1.8	0.0
	Mar	9.7	9.7	2.0	-7.7	0.0
	Apr	14.2	14.2	0.7	-13.5	0.0
	May	20.4	20.4	0.4	-20.0	0.0
	Jun	24.3	24.3	0.2	-24.2	0.0
	Jul	27.1	27.1	0.4	-26.6	0.0
	Aug	24.9	24.9	0.8	-24.1	0.0
	Sep	17.7	17.7	0.6	-17.1	0.0
	Oct	9.9	9.9	0.7	-9.1	0.0
	Nov	4.7	4.7	0.9	-3.8	0.0
	Dec	2.2	2.2	1.9	-0.3	0.0
Guvo	Jan	1.2	1.2	2.6	1.5	3.3
	Feb	3.2	3.2	2.6	-0.7	2.6
	Mar	7.5	7.4	2.7	-4.8	0.0
	Apr	12.6	12.3	0.8	-11.5	0.0
	May	17.8	17.7	0.5	-17.2	0.0
	Jun	20.5	20.4	0.3	-20.1	0.0
	Jul	21.0	20.9	3.2	-17.7	0.0
	Aug	18.5	18.5	3.7	-14.8	0.0
	Sep	15.0	15.0	2.2	-12.7	0.0
	Oct	8.9	8.8	1.8	-7.0	0.0
	Nov	3.1	3.1	1.8	-1.3	0.0
	Dec	0.9	0.9	2.7	1.9	1.9
Cross-Apache	Jan	1.5	0.0	2.8	2.8	5.1
	Feb	3.1	1.1	2.9	1.8	6.9
	Mar	6.9	6.9	2.7	-4.1	2.8
	Apr	10.8	10.8	1.4	-9.4	0.0
	May	16.2	16.2	0.9	-15.3	0.0
	Jun	20.0	20.0	0.8	-19.2	0.0
	Jul	19.8	19.8	4.6	-15.2	0.0
	Aug	17.4	17.4	5.5	-11.9	0.0
	Sep	13.6	13.6	3.5	-10.1	0.0
	Oct	7.4	7.4	2.8	-4.6	0.0
	Nov	2.7	2.3	2.2	-0.1	0.0
	Dec	1.3	0.0	2.3	2.3	2.3
Cornville	Jan	1.7	1.7	3.4	1.7	3.7
	Feb	3.0	3.0	3.5	0.5	4.2
	Mar	7.5	7.5	3.4	-4.1	0.1
	Apr	12.1	12.1	1.6	-10.5	0.0
	May	17.7	17.7	1.1	-16.6	0.0
	Jun	20.8	20.8	0.7	-20.1	0.0
	Jul	20.0	20.0	4.6	-15.4	0.0
	Aug	17.6	17.6	5.5	-12.1	0.0
	Sep	13.9	13.9	4.4	-9.5	0.0
	Oct	7.8	7.8	2.7	-5.1	0.0
	Nov	2.5	2.5	2.4	-0.1	0.0
	Dec	1.2	1.2	3.2	2.1	2.1

Site	Month	ET_0 (cm)	ET_0' (cm)[a]	Precip (cm)	P-ET0 (cm)	Soil Water Storage (cm)
Plughat	Jan	2.2	0.0	1.2	1.2	3.5
	Feb	2.8	0.0	1.7	1.7	5.3
	Mar	5.7	4.3	2.8	-1.5	3.8
	Apr	9.1	9.1	2.4	-6.8	0.0
	May	12.8	13.1	5.3	-7.8	0.0
	Jun	15.6	15.9	5.5	-10.4	0.0
	Jul	16.4	17.0	7.0	-10.0	0.0
	Aug	14.2	14.7	7.3	-7.4	0.0
	Sep	10.6	11.0	4.6	-6.3	0.0
	Oct	6.5	6.6	3.6	-3.0	0.0
	Nov	3.3	2.1	2.1	0.1	0.1
	Dec	1.8	0.0	2.2	2.2	2.3
Montecito	Jan	1.2	0.0	1.6	1.6	5.1
	Feb	2.7	0.0	1.4	1.4	6.5
	Mar	6.6	1.3	2.0	0.7	7.3
	Apr	10.8	10.8	2.0	-8.7	0.0
	May	15.5	15.5	2.9	-12.6	0.0
	Jun	18.2	18.2	2.5	-15.7	0.0
	Jul	17.1	17.1	3.8	-13.3	0.0
	Aug	14.9	14.9	5.2	-9.6	0.0
	Sep	12.6	12.6	3.8	-8.8	0.0
	Oct	8.0	8.0	3.3	-4.7	0.0
	Nov	3.5	0.4	2.0	1.7	1.7
	Dec	1.3	0.0	1.9	1.9	3.6
Witt	Jan	1.5	0.0	1.4	1.4	4.6
	Feb	3.2	0.0	1.5	1.5	6.2
	Mar	6.4	4.7	2.1	-2.7	3.5
	Apr	9.8	9.8	1.5	-8.3	0.0
	May	12.9	13.1	1.9	-11.1	0.0
	Jun	14.4	14.3	2.6	-11.7	0.0
	Jul	14.0	14.1	6.8	-7.3	0.0
	Aug	12.8	13.0	7.3	-5.7	0.0
	Sep	9.6	9.7	4.6	-5.1	0.0
	Oct	5.9	5.9	3.8	-2.1	0.0
	Nov	2.7	1.5	1.9	0.5	0.5
	Dec	1.2	0.0	2.7	2.7	3.2
Kranzburg	Jan	0.0	0.0	0.9	0.9	5.7
	Feb	0.3	0.0	1.0	1.0	6.7
	Mar	2.0	0.5	2.9	2.4	9.2
	Apr	5.6	5.6	5.4	-0.2	8.9
	May	9.2	9.2	7.5	-1.6	7.3
	Jun	12.3	12.3	10.9	-1.3	6.0
	Jul	13.8	13.8	8.3	-5.6	0.4
	Aug	11.9	11.9	7.8	-4.1	0.0
	Sep	7.7	7.7	8.1	0.4	0.4
	Oct	4.0	4.0	5.2	1.2	1.7
	Nov	1.3	0.5	2.4	1.9	3.6
	Dec	0.2	0.0	1.2	1.2	4.8
Clamo	Jan	0.0	0.0	0.56	0.6	4.1
	Feb	0.4	0.0	0.86	0.9	4.9
	Mar	2.4	0.2	2.69	2.5	7.5
	Apr	5.9	5.9	5.54	-0.3	7.2
	May	9.6	9.6	7.44	-2.2	5.0
	Jun	12.8	12.8	10.49	-2.3	2.7
	Jul	14.9	14.9	7.90	-7.0	0.0
	Aug	12.9	12.9	6.05	-6.8	0.0
	Sep	7.7	7.7	5.89	-1.8	0.0
	Oct	3.5	3.5	4.11	0.6	0.6
	Nov	1.1	0.2	1.98	1.8	2.4
	Dec	0.1	0.0	1.14	1.1	3.5

Site	Month	ET_0 (cm)	ET_0' (cm)[a]	Precip (cm)	P-ET0 (cm)	Soil Water Storage (cm)
Eros	Jan	0.1	0	1.8	1.8	8.8
	Feb	0.4	0	1.4	1.4	10.3
	Mar	2.1	0.3	4.4	4.1	14.3
	Apr	5.6	5.6	7.7	2.1	16.4
	May	9.6	9.6	8.2	-1.4	15.0
	Jun	12.8	12.8	11.2	-1.6	13.4
	Jul	14.6	14.6	7.9	-6.7	6.7
	Aug	12.7	12.7	8.1	-4.6	2.1
	Sep	8.1	8.1	8.0	-0.1	2.0
	Oct	4.0	4.0	5.6	1.6	1.6
	Nov	1.3	0.5	4.1	3.6	5.2
	Dec	0.2	0	1.9	1.9	7.1
Adams Ranch	Jan	3.8	0.0	1.6	1.6	4.1
	Feb	5.1	0.0	1.8	1.8	5.9
	Mar	8.8	5.7	1.7	-4.0	1.9
	Apr	12.0	12.0	2.1	-9.9	0.0
	May	15.0	15.0	2.8	-12.1	0.0
	Jun	16.5	16.5	3.8	-12.7	0.0
	Jul	15.4	15.4	8.4	-6.9	0.0
	Aug	13.9	13.9	8.2	-5.7	0.0
	Sep	11.3	11.3	5.1	-6.2	0.0
	Oct	8.8	8.8	4.7	-4.0	0.0
	Nov	5.8	3.1	2.1	-1.0	0.0
	Dec	4.0	0.0	2.5	2.5	2.5

[a]Calculated by multiplying ET_0 by the fraction of days in the month when the normal daily normal minimum temperature is > -4°C

Table A.4 Raw Clumped Isotope Data

Type	Date	Name	δ^{47} ‰,WG[a]	δ^{48} ‰,WG[a]	$\delta^{13}C$ ‰,VSMOW	$\delta^{18}O$ ‰,VPDB
May–June 2012						
Heated Gas	05/13/12	Heated Gas IV	-27.51	-5.23	-18.98	23.68
Heated Gas	05/14/12	Heated Gas V	-3.78	48.02	-3.68	32.19
25°C Equil. Gas	05/14/12	MDIW CO2-H2O 25C	-27.93	14.14	-28.10	31.47
25°C Equil Gas	05/14/12	AAS CO2-H2O 25C	-41.23	-39.29	-28.18	18.17
Heated Gas	05/14/12	Barbados Coral HG	-7.00	-11.97	-1.78	27.14
25°C Equil Gas	05/14/12	Evap CO2-H2O 25C	-8.79	42.61	-27.08	49.73
Standard	05/14/12	Cararra 75C rxn	7.39	8.77	1.83	37.47
25°C Equil Gas	05/15/12	AAS CO2-H2O 25C	-41.03	-42.23	-28.05	18.19
Standard	05/15/12	Cararra 75C rxn	7.20	7.24	1.86	37.25
Standard	05/15/12	Cararra 75C rxn	7.34	7.29	1.93	37.32
25°C Equil Gas	05/15/12	Evap CO2-H2O 25C	-12.83	32.58	-28.30	46.90
Heated Gas	05/16/12	MDIW HG	-31.45	-15.08	-28.04	28.68
Heated Gas	05/16/12	AAS HG	-42.71	-45.71	-28.08	17.34
25°C Equil Gas	05/17/12	MDIW CO2-H2O 25C	-27.77	-7.12	-28.09	31.59
Heated Gas	05/17/12	Barbados Coral HG	-4.08	-12.15	-1.79	30.02
25°C Equil Gas	05/17/12	AAS CO2-H2O 25C	-40.96	-42.53	-28.13	18.34
Standard	05/18/12	Cararra 75C rxn AB	7.31	6.70	1.89	37.31
Heated Gas	05/18/12	Evap HG	-22.47	9.47	-28.75	38.45
25°C Equil Gas[b]	05/20/12	MDIW CO2-h2O 25C	-27.20	-8.04	-28.08	31.60
Heated Gas	05/20/12	Heated Gas	-64.52	-66.69	-42.49	9.42
25°C Equil Gas	05/20/12	Evap CO2-H2O 25C	-8.54	40.25	-27.09	50.02
Heated Gas	05/22/12	MDIW HG	-30.34	-13.85	-28.04	29.79
25°C Equil Gas	05/22/12	AAS CO2-H2O 25C	-40.32	-41.72	-28.15	18.99
25°C Equil Gas	05/24/12	Evap CO2-H2O 25C	-14.78	28.51	-28.94	45.53
Heated Gas	05/24/12	AAS HG	-42.96	-47.75	-28.08	17.09
25°C Equil Gas	05/25/12	AAS CO2-H2O 25C	-39.80	-40.76	-28.05	19.42
Heated Gas	05/25/12	Evap HG	-19.15	18.01	-28.80	41.87
Heated Gas	05/26/12	Adamussium HG	1.75	-6.51	1.85	32.21
25°C Equil Gas	05/26/12	MDIW CO2-H2O 25C	-28.56	-10.31	-28.17	30.86
Heated Gas	05/27/12	Matheson HG	-8.98	-20.28	-3.96	27.30
25°C Equil Gas	05/27/12	Evap CO2-H2O 25C	-11.48	34.23	-27.85	47.79
Heated Gas	05/29/12	Barbados Coral HG	-5.24	-16.57	-1.67	28.78
25°C Equil Gas	05/29/12	MDIW 25C	-26.57	-13.45	-25.09	29.89
Heated Gas	05/30/12	Heated Gas IV	-8.89	-17.94	-4.83	28.21
25°C Equil Gas	05/30/12	AAS CO2-H2O 25C	-41.70	-44.44	-28.51	17.95
25°C Equil Gas	05/31/12	Evap CO2-H2O 25C	-13.30	30.48	-28.46	46.56
Heated Gas	05/31/12	AAS HG	-41.95	-44.91	-28.01	18.05
Heated Gas	06/01/12	MDIW HG	-32.47	-19.06	-28.23	27.82
25°C Equil Gas	06/02/12	MDIW CO2-H20 25C	-28.15	-10.03	-28.10	31.24
25°C Equil Gas	06/03/12	AAS CO2-H2O 25C	-43.66	-49.22	-28.95	16.40
Heated Gas	06/03/12	Evap HG	-20.33	13.78	-28.39	40.24
Sample	06/04/12	Cornville	-3.60	-16.73	-0.59	28.77
Heated Gas	06/04/12	HG-I	-6.29	-13.78	-3.85	29.87
25°C Equil Gas	06/04/12	AAS CO2-H2O 25C	-39.38	-40.66	-27.65	19.45
Sample	06/04/12	Plughat-P1	-7.64	-11.54	-6.51	30.53
Sample	06/04/12	Plughat-P2	-8.40	-13.80	-6.46	29.74
Sample	06/05/12	Cross-Apache	-8.29	-12.72	-6.65	30.04
Heated Gas	06/05/12	Adamussium HG	9.46	12.08	1.98	39.66
25°C Equil Gas	06/05/12	Evap CO2-H2O 25C	-11.26	35.33	-28.00	48.18
Sample	06/06/12	Cornville	-3.78	-16.74	-0.64	28.64
Sample	06/06/12	Witt	-4.46	-7.52	-5.05	32.26
Sample	06/06/12	Cross-Apache	-7.67	-12.05	-6.38	30.39
Sample	06/06/12	Guvo	-1.77	-3.27	-3.79	33.68
Sample	06/06/12	Plughat-P2	-8.59	-13.87	-6.50	29.59
Heated Gas	06/07/12	HG II	-32.70	-36.76	-21.53	20.99
25°C Equil Gas	06/07/12	MDIW CO2-H2O 25C	-28.47	-10.46	-28.14	30.97
25°C Equil Gas	06/07/12	MDIW CO2-H2O 25C	-28.47	-10.46	-28.14	30.97
Sample	06/07/12	Cornville	-3.10	-15.19	-0.47	29.16
Sample	06/07/12	Plughat-P1	-7.14	-10.79	-6.18	30.70
Heated Gas	06/08/12	HG III #1	-33.94	-39.00	-22.08	20.28
25°C Equil Gas	06/08/12	MDIW CO2-H2O 25C	-27.91	-9.15	-28.10	31.47

Type	Date	Name	δ^{47} ‰,WG[a]	δ^{48} ‰,WG[a]	$\delta^{13}C$ ‰,VSMOW	$\delta^{18}O$ ‰,VPDB
Sample	06/08/12	Plughat-P2	-7.72	-11.92	-6.54	30.50
Sample	06/08/12	Cross-Apache	-7.93	-12.17	-6.58	30.31
Sample	06/09/12	Witt	-4.41	-7.01	-5.05	32.29
Sample	06/09/12	Kranzburg	0.31	-5.86	-0.79	32.79
Sample	06/09/12	Guvo	-2.06	-3.28	-3.73	33.35
Heated Gas	06/09/12	Barbados Coral HG	-6.02	-18.09	-1.73	28.06
25°C Equil Gas	06/09/12	Evap CO2-H2O 25C	-11.67	34.94	-28.14	47.89
Sample	06/10/12	Witt	-4.39	-6.98	-5.03	32.29
Sample	06/10/12	Guvo	-1.97	-4.03	-3.69	33.39
Sample	06/10/12	Montecito	-5.97	-12.63	-4.35	30.07
Sample	06/10/12	Plughat-P2	-8.68	-13.87	-6.61	29.63
Sample	06/10/12	Montecito	-6.41	-13.30	-4.59	29.88
Heated Gas	06/11/12	Adamussium and Jolters HG	-6.29	-9.57	-5.47	31.48
25°C Equil Gas	06/11/12	AAS CO2-H2O 25C	-45.75	-52.36	-29.60	14.95
Sample	06/11/12	Montecito	-6.31	-13.41	-4.49	29.86
Sample	06/11/12	Kranzburg	0.35	-5.74	-0.71	32.74
Sample	06/11/12	Kranzburg	0.63	-5.32	-0.61	32.93
Heated Gas	06/12/12	MDIW HG	-33.40	-21.70	-28.22	26.87
25°C Equil Gas	06/12/12	MDIW CO2-H2O 25C	-28.29	-9.72	-28.21	31.22
Sept–Oct 2012						
Heated Gas	10/23/12	Matheson HG	-4.58	-9.78	-3.62	31.27
Heated Gas	10/23/12	Evap HG	-18.15	18.22	-28.07	41.99
Heated Gas	10/23/12	AAS HG	-41.67	-41.83	-28.00	18.01
Heated Gas	10/24/12	Math/BD Mix HG	-17.51	-19.35	-12.79	27.40
Heated Gas	10/24/12	Barbados Coral HG	-3.30	-10.57	-1.56	30.52
Heated Gas	10/24/12	MDIW HG	-30.64	-14.11	-28.25	29.49
Heated Gas	10/24/12	Matheson HG	-2.58	-4.31	-3.73	33.35
25°C Equil Gas	10/24/12	MDIW CO2-H2O 25C	-27.94	-8.81	-28.24	31.39
25°C Equil Gas	10/24/12	AAS CO2-H2O 25C	-41.88	-44.52	-28.05	17.01
25°C Equil Gas	10/25/12	Evap CO2-H2O 25C	-12.02	30.79	-27.99	47.28
25°C Equil Gas	10/25/12	AAS CO2-H2O 25C	-41.48	-42.96	-28.09	17.48
Heated Gas	10/25/12	AAS HG	-41.49	-41.35	-28.15	18.35
Heated Gas	10/25/12	MDIW HG	-31.78	-16.90	-28.13	28.19
Heated Gas	10/25/12	Admussium HG	9.41	12.00	1.91	39.69
Standard	10/25/12	Cararra 75C rxn	5.78	4.13	1.13	36.55
25°C Equil Gas	10/26/12	Evap CO2-H2O 25C	-12.51	30.72	-28.26	47.08
Heated Gas	10/26/12	Matheson HG	-6.62	-14.59	-3.53	29.17
Standard	10/26/12	Cararra 75C rxn	6.43	4.34	1.67	36.69
25°C Equil Gas	10/26/12	MDIW CO2-H2O 25C	-27.47	-7.60	-28.10	31.70
25°C Equil Gas	10/27/12	AAS CO2-H2O 25C	-42.37	-45.13	-28.17	16.63
Heated Gas	10/28/12	BD HG	-29.91	-35.44	-18.79	20.83
25°C Equil Gas	10/28/12	Evap 25C	-12.04	31.09	-28.07	47.34
25°C Equil Gas	10/29/12	MDIW CO2-H2O 25C	-28.05	-8.83	-28.23	31.27
Heated Gas	10/29/12	MDIW HG	-31.22	-15.23	-28.20	28.87
Heated Gas	10/30/12	AAS HG	-42.80	-45.05	-28.19	17.08
25°C Equil Gas	10/31/12	AAS CO2-H2O 25C	-41.41	-43.22	-28.20	17.67
Heated Gas	11/01/12	Evap HG	-18.28	17.08	-27.98	41.79
25°C Equil Gas	11/01/12	MDIW CO2-H20 25C	-29.32	-12.51	-28.18	29.93
25°C Equil Gas	11/02/12	Evap CO2-H2O 25C	-12.86	30.07	-28.21	46.66
Heated Gas	11/02/12	MDIW HG	-30.24	-13.77	-28.00	29.70
Heated Gas	11/03/12	AAS HG	-43.21	-46.19	-28.17	16.70
25°C Equil Gas	11/03/12	AAS CO2-H2O 25C	-40.62	-41.65	-28.08	18.39
Heated Gas	11/04/12	Evap HG	-15.97	23.04	-28.06	44.22
25°C Equil Gas	11/04/12	Evap CO2-H2O 25C	-15.31	23.79	-28.25	44.18
25°C Equil Gas	11/05/12	MDIW CO2-H2O 25C	-28.59	-10.32	-28.28	30.80
Heated Gas	11/06/12	Barbados Coral HG	-4.05	-13.09	-1.63	29.85
25°C Equil Gas	11/06/12	AAS CO2-H2O 25C	-41.59	-44.39	-28.07	17.43
Heated Gas	11/07/12	Matheson HG	-13.49	-28.55	-5.02	23.76
25°C Equil Gas	11/07/12	Evap CO2-H2O 25C	-14.43	25.59	-28.07	44.92
Heated Gas	11/08/12	AAS HG	-42.02	-43.78	-28.03	17.80
25°C Equil Gas	11/08/12	MDIW CO2-H2O 25C	-27.99	-9.43	-28.09	31.26
Heated Gas	11/10/12	MDIW HG	-32.88	-20.56	-28.09	27.13
25°C Equil Gas	11/10/12	AAS CO2-H2O 25C	-42.26	-45.69	-28.17	16.86
Heated Gas	11/11/12	Evap HG	-18.90	15.94	-28.10	41.32
25°C Equil Gas	11/11/12	MDIW CO2-H2O 25C	-28.73	-11.38	-28.10	30.50

Type	Date	Name	δ^{47} ‰,WG[a]	δ^{48} ‰,WG[a]	$\delta^{13}C$ ‰,VSMOW	$\delta^{18}O$ ‰,VPDB
Heated Gas	11/12/12	AAS HG	-41.91	-43.31	-28.13	18.01
25°C Equil Gas	11/14/12	MDIW CO2-H2O 25C	-28.42	-10.59	-28.15	30.91
Heated Gas	11/14/12	Matheson HG	-9.33	-21.10	-3.84	26.78
Sample	11/14/12	Muroc	-7.81	-13.95	-5.54	29.35
Sample	11/15/12	Lavic	-6.67	-17.08	-3.24	28.27
25°C Equil Gas	11/15/12	Evap CO2-H2O 25C	-11.78	32.41	-27.96	47.52
Heated Gas	11/15/12	Evap HG	-15.42	24.78	-28.01	44.73
25°C Equil Gas	11/16/12	AAS CO2-H2O 25C	-40.70	-42.51	-27.86	18.17
Heated Gas	11/16/12	MDIW HG	-31.24	-15.39	-28.17	28.86
Heated Gas	11/17/12	AAS HG	-42.71	-45.05	-28.21	17.31
25°C Equil Gas	11/18/12	MDIW CO2-H2O 25C	-29.80	-14.57	-27.88	29.18
25°C Equil Gas	11/19/12	Evap CO2-H2O 25C	-12.30	31.69	-28.07	47.13
Heated Gas	11/19/12	Evap HG	-16.24	22.54	-28.03	43.93
Sample	11/19/12	Muroc	-7.48	-13.94	-5.36	29.49
Sample	11/19/12	Lavic	-6.98	-17.27	-3.53	28.21
25°C Equil Gas	11/20/12	AAS CO2-H2O 25C	-41.62	-44.01	-28.25	17.60
Heated Gas	11/20/12	Evap HG	-19.04	15.64	-28.07	41.14
Sample	11/20/12	Muroc	-8.33	-14.30	-6.01	29.32
Sample	11/20/12	Lavic	-6.99	-16.88	-3.57	28.24
Heated Gas	11/21/12	MDIW HG	-29.36	-11.42	-28.05	30.67
25°C Equil Gas	11/21/12	MDIW CO2-H20 25C	-29.50	-13.62	-27.88	29.51
Sept–Oct 2012						
Heated Gas	10/19/13	Math HG	-8.75	-15.75	-4.95	28.41
Heated Gas	10/19/13	AAS HG	-56.86	-44.12	-41.66	16.04
Heated Gas	10/20/13	BCoral HG	-45.68	-17.70	-41.51	27.39
Heated Gas	10/20/13	BCoral HG	-9.55	-21.34	-2.97	25.66
Heated Gas	10/20/13	Evap HG	-29.51	21.06	-40.99	43.35
Heated Gas	10/20/13	MCB HG	-16.17	-29.89	-6.15	22.19
Heated Gas	10/20/13	Barbados Coral HG	-11.07	-25.26	-2.94	24.14
Heated Gas	10/21/13	Cararra HG	3.05	-4.13	2.00	33.33
Heated Gas	10/21/13	MCB HG	-15.48	-30.20	-5.92	22.68
Heated Gas	10/21/13	BCoral HG	-10.02	-24.31	-2.78	25.07
Heated Gas	10/21/13	Carerra HG	4.05	-2.74	2.26	34.07
Heated Gas	10/21/13	MCB HG	-17.24	-36.11	-5.35	20.36
Heated Gas	10/22/13	BCoral HG	-7.86	-19.26	-2.79	27.23
Heated Gas	10/22/13	Carerra HG	3.44	-3.98	2.32	33.43
25°C Equil Gas	10/22/13	AAS 25C	-54.71	-42.87	-41.53	17.30
25°C Equil Gas	10/22/13	MDIW 25C	-41.40	-10.09	-41.38	30.87
Heated Gas	10/22/13	Cararra HG	3.20	-3.86	1.95	33.54
25°C Equil Gas	10/22/13	Evap 25C	-26.18	28.57	-41.47	46.62
Heated Gas	10/23/13	MCB HG	-5.32	-14.57	-1.98	28.90
Heated Gas	10/23/13	AAS HG	-55.46	-43.32	-41.39	17.27
25°C Equil Gas	10/23/13	AAS 25C	-54.92	-42.88	-41.61	17.21
25°C Equil Gas	10/23/13	Evap 25C	-25.04	31.61	-41.39	47.75
25°C Equil Gas	10/23/13	MDIW 25C	-41.36	-9.54	-41.43	31.00
Standard	10/24/13	ActualCarerra	6.90	5.11	1.91	36.94
Heated Gas	10/24/13	Evap HG	-15.78	22.46	-27.90	44.25
25°C Equil Gas	10/24/13	AAS 25C	-54.31	-42.31	-41.41	17.65
Standard	10/24/13	Cararra 75C rxn	7.37	6.35	1.99	37.31
25°C Equil Gas	10/25/13	Evap 25C	-26.14	31.11	-41.61	46.81
Heated Gas	10/26/13	MCB HG	-6.33	-17.72	-1.73	27.71
25°C Equil Gas	10/26/13	MDIW 25C	-41.41	-10.25	-41.27	30.83
Heated Gas	10/28/13	MCB HG	-3.71	-11.77	-1.71	30.25
25°C Equil Gas	10/28/13	AAS 25C	-54.74	-41.55	-41.55	17.38
25°C Equil Gas	10/29/13	Evap 25C	-25.45	31.04	-41.40	47.33
Heated Gas	10/29/13	Cararra HG	3.04	-4.52	2.10	33.22
Heated Gas	10/30/13	Barbados Coral HG	-11.39	-27.62	-2.82	23.79
25°C Equil Gas	10/30/13	MDIW 25C	-42.03	-11.00	-41.45	30.38
Standard	10/30/13	Cararra #1 75C BL	6.72	4.93	1.73	36.95
Standard	10/31/13	Cararra #2 75C BL	7.15	5.63	1.93	37.13
25°C Equil Gas	10/31/13	AAS 25C	-55.47	-45.08	-41.47	16.62
Heated Gas	10/31/13	Evap HG	-32.77	14.64	-41.59	40.91
Standard	11/01/13	Cararra #3 75C WD	6.58	7.06	1.79	36.71
Heated Gas	11/01/13	MCB HG	-5.81	-17.12	-1.63	28.14
25°C Equil Gas	11/01/13	MDIW 25C	-41.59	-10.72	-41.23	30.63

Type	Date	Name	δ^{47} ‰,WG[a]	δ^{48} ‰,WG[a]	$\delta^{13}C$ ‰,VSMOW	$\delta^{18}O$ ‰,VPDB
Heated Gas	11/03/13	AAS HG	-56.33	-45.37	-41.51	16.65
25°C Equil Gas	11/03/13	Evap 25C	-25.35	31.45	-41.38	47.44
Standard	11/03/13	Carerra #4 75C WD	5.66	3.44	1.23	36.36
25°C Equil Gas	11/04/13	AAS 25C	-54.46	-42.36	-41.44	17.70
Heated Gas	11/04/13	Evap HG	-30.01	21.32	-41.26	43.42
Heated Gas	11/05/13	BCoral HG	-8.82	-22.57	-2.58	26.08
25°C Equil Gas	11/05/13	MDIW 25C	-41.96	-11.14	-41.30	30.35
Heated Gas	11/06/13	Cararra HG	6.18	3.05	2.25	36.21
25°C Equil Gas	11/07/13	Evap 25C	-25.69	31.08	-41.42	47.18
Heated Gas	11/08/13	MCB HG	-3.52	-12.12	-1.54	30.32
25°C Equil Gas	11/08/13	AAS 25 C	-54.85	-44.19	-41.49	17.35
Heated Gas	11/09/13	MDIW HG	-44.06	-14.68	-41.51	29.28
25°C Equil Gas	11/09/13	MDIW 25C	-41.86	-11.25	-41.49	30.66
Sample	11/10/13	Clamo	1.24	-3.64	-0.65	33.58
Heated Gas	11/10/13	AAS HG	-15.03	-30.22	-5.74	22.96
25°C Equil Gas	11/10/13	Evap 25C	-25.48	31.85	-41.38	47.36
Sample	11/10/13	Clamo	1.64	-2.60	-0.57	33.87
Sample	11/10/13	Clamo	1.18	-3.46	-0.64	33.50
25°C Equil Gas	11/11/13	AAS 25C BL	-54.84	-41.69	-41.04	16.91
Heated Gas	11/11/13	EVAP HG BL	-29.15	24.48	-41.61	44.69

[a]Working gas

[b]Irregular heated gas, excluded from the reference frame calculations

Table A.5 Clumped Isotope Data – Samples in the Absolute Reference Frame

Type	Date	Name	$\Delta_{47\text{-}[SGvsWG]0}$ ‰	$\Delta_{47\text{-}RF}$[a] ‰	$\Delta_{47\text{-}RF\text{-}AC}$[b] ‰	T[c] °C
May–June 2012						
Heated Gas	05/13/12	Heated Gas IV				
Heated Gas	05/14/12	Heated Gas V				
25°C Equil. Gas	05/14/12	MDIW CO2-H2O 25C				
25°C Equil Gas	05/14/12	AAS CO2-H2O 25C				
Heated Gas	05/14/12	Barbados Coral HG				
25°C Equil Gas	05/14/12	Evap CO2-H2O 25C				
Standard	05/14/12	Cararra 75C rxn				
25°C Equil Gas	05/15/12	AAS CO2-H2O 25C				
Standard	05/15/12	Cararra 75C rxn				
Standard	05/15/12	Cararra 75C rxn				
25°C Equil Gas	05/15/12	Evap CO2-H2O 25C				
Heated Gas	05/16/12	MDIW HG				
Heated Gas	05/16/12	AAS HG				
25°C Equil Gas	05/17/12	MDIW CO2-H2O 25C				
Heated Gas	05/17/12	Barbados Coral HG				
25°C Equil Gas	05/17/12	AAS CO2-H2O 25C				
Standard	05/18/12	Cararra 75C rxn AB				
Heated Gas	05/18/12	Evap HG				
25°C Equil Gas[d]	05/20/12	MDIW CO2-h2O 25C				
Heated Gas	05/20/12	Heated Gas				
25°C Equil Gas	05/20/12	Evap CO2-H2O 25C				
Heated Gas	05/22/12	MDIW HG				
25°C Equil Gas	05/22/12	AAS CO2-H2O 25C				
25°C Equil Gas	05/24/12	Evap CO2-H2O 25C				
Heated Gas	05/24/12	AAS HG				
25°C Equil Gas	05/25/12	AAS CO2-H2O 25C				
Heated Gas	05/25/12	Evap HG				
Heated Gas	05/26/12	Adamussium HG				
25°C Equil Gas	05/26/12	MDIW CO2-H2O 25C				
Heated Gas	05/27/12	Matheson HG				
25°C Equil Gas	05/27/12	Evap CO2-H2O 25C				
Heated Gas	05/29/12	Barbados Coral HG				
25°C Equil Gas	05/29/12	MDIW 25C				
Heated Gas	05/30/12	Heated Gas IV				
25°C Equil Gas	05/30/12	AAS CO2-H2O 25C				
25°C Equil Gas	05/31/12	Evap CO2-H2O 25C				
Heated Gas	05/31/12	AAS HG				
Heated Gas	06/01/12	MDIW HG				
25°C Equil Gas	06/02/12	MDIW CO2-H20 25C				
25°C Equil Gas	06/03/12	AAS CO2-H2O 25C				
Heated Gas	06/03/12	Evap HG				
Sample	06/04/12	Cornville	-0.356	0.640	0.707	21.1
Heated Gas	06/04/12	HG-I				
25°C Equil Gas	06/04/12	AAS CO2-H2O 25C				
Sample	06/04/12	Plughat-P1	-0.305	0.697	0.763	3.6
Sample	06/04/12	Plughat-P2	-0.314	0.687	0.754	6.4
Sample	06/05/12	Cross-Apache	-0.315	0.686	0.753	6.6
Heated Gas	06/05/12	Adamussium HG				
25°C Equil Gas	06/05/12	Evap CO2-H2O 25C				
Sample	06/06/12	Cornville	-0.347	0.651	0.718	17.6
Sample	06/06/12	Witt	-0.330	0.670	0.736	11.6
Sample	06/06/12	Cross-Apache	-0.324	0.676	0.743	9.5
Sample	06/06/12	Guvo	-0.337	0.662	0.728	14.1
Sample	06/06/12	Plughat-P2	-0.316	0.684	0.751	7.1
Heated Gas	06/07/12	HG II				
25°C Equil Gas	06/07/12	MDIW CO2-H2O 25C				
25°C Equil Gas	06/07/12	MDIW CO2-H2O 25C				
Sample	06/07/12	Cornville	-0.362	0.634	0.701	23.2
Sample	06/07/12	Plughat-P1	-0.303	0.699	0.766	2.8
Heated Gas	06/08/12	HG III #1				

Type	Date	Name	$\Delta_{47\text{-}[SGvsWG]0}$ ‰	$\Delta_{47\text{-}RF}$[a] ‰	$\Delta_{47\text{-}RF\text{-}AC}$[b] ‰	T[c] °C
25°C Equil Gas	06/08/12	MDIW CO2-H2O 25C				
Sample	06/08/12	Plughat-P2	-0.327	0.673	0.740	10.5
Sample	06/08/12	Cross-Apache	-0.307	0.694	0.761	4.2
Sample	06/09/12	Witt	-0.316	0.685	0.752	6.8
Sample	06/09/12	Kranzburg	-0.341	0.657	0.724	15.5
Sample	06/09/12	Guvo	-0.353	0.644	0.710	20.0
Heated Gas	06/09/12	Barbados Coral HG				
25°C Equil Gas	06/09/12	Evap CO2-H2O 25C				
Sample	06/10/12	Witt	-0.320	0.680	0.747	8.4
Sample	06/10/12	Guvo	-0.339	0.659	0.726	14.8
Sample	06/10/12	Montecito	-0.314	0.687	0.753	6.4
Sample	06/10/12	Plughat-P2	-0.334	0.665	0.732	13.1
Sample	06/10/12	Montecito	-0.319	0.681	0.748	8.0
Heated Gas	06/11/12	Adamussium and Jolters HG				
25°C Equil Gas	06/11/12	AAS CO2-H2O 25C				
Sample	06/11/12	Montecito	-0.304	0.698	0.765	3.1
Sample	06/11/12	Kranzburg	-0.326	0.674	0.740	10.3
Sample	06/11/12	Kranzburg	-0.335	0.664	0.730	13.5
Heated Gas	06/12/12	MDIW HG				
25°C Equil Gas	06/12/12	MDIW CO2-H2O 25C				
Sept–Oct 2012						
Heated Gas	10/23/12	Matheson HG				
Heated Gas	10/23/12	Evap HG				
Heated Gas	10/23/12	AAS HG				
Heated Gas	10/24/12	Math/BD Mix HG				
Heated Gas	10/24/12	Barbados Coral HG				
Heated Gas	10/24/12	MDIW HG				
Heated Gas	10/24/12	Matheson HG				
25°C Equil Gas	10/24/12	MDIW CO2-H2O 25C				
25°C Equil Gas	10/24/12	AAS CO2-H2O 25C LOW YIELD				
25°C Equil Gas	10/25/12	Evap CO2-H2O 25C				
25°C Equil Gas	10/25/12	AAS CO2-H2O 25C				
Heated Gas	10/25/12	AAS HG				
Heated Gas	10/25/12	MDIW HG				
Heated Gas	10/25/12	Admussium HG				
Standard	10/25/12	Cararra 75C rxn				
25°C Equil Gas	10/26/12	Evap CO2-H2O 25C				
Heated Gas	10/26/12	Matheson HG				
Standard	10/26/12	Cararra 75C rxn				
25°C Equil Gas	10/26/12	MDIW CO2-H2O 25C				
25°C Equil Gas	10/27/12	AAS CO2-H2O 25C				
Heated Gas	10/28/12	BD HG				
25°C Equil Gas	10/28/12	Evap 25C				
25°C Equil Gas	10/29/12	MDIW CO2-H2O 25C				
Heated Gas	10/29/12	MDIW HG				
Heated Gas	10/30/12	AAS HG				
25°C Equil Gas	10/31/12	AAS CO2-H2O 25C				
Heated Gas	11/01/12	Evap HG				
25°C Equil Gas	11/01/12	MDIW CO2-H20 25C				
25°C Equil Gas	11/02/12	Evap CO2-H2O 25C				
Heated Gas	11/02/12	MDIW HG				
Heated Gas	11/03/12	AAS HG				
25°C Equil Gas	11/03/12	AAS CO2-H2O 25C				
Heated Gas	11/04/12	Evap HG				
25°C Equil Gas	11/04/12	Evap CO2-H2O 25C				
25°C Equil Gas	11/05/12	MDIW CO2-H2O 25C				
Heated Gas	11/06/12	Barbados Coral HG				
25°C Equil Gas	11/06/12	AAS CO2-H2O 25C				
Heated Gas	11/07/12	Matheson HG				
25°C Equil Gas	11/07/12	Evap CO2-H2O 25C				
Heated Gas	11/08/12	AAS HG				
25°C Equil Gas	11/08/12	MDIW CO2-H2O 25C				
Heated Gas	11/10/12	MDIW HG				
25°C Equil Gas	11/10/12	AAS CO2-H2O 25C				
Heated Gas	11/11/12	Evap HG				

Type	Date	Name	$\Delta_{47\text{-}[SGvsWG]0}$ ‰	$\Delta_{47\text{-}RF}$[a] ‰	$\Delta_{47\text{-}RF\text{-}AC}$[b] ‰	T[c] °C
25°C Equil Gas	11/11/12	MDIW CO2-H2O 25C				
Heated Gas	11/12/12	AAS HG				
25°C Equil Gas	11/14/12	MDIW CO2-H2O 25C				
Heated Gas	11/14/12	Matheson HG				
Sample	11/14/12	Muroc	-0.271	0.678	0.744	9.1
Sample	11/15/12	Lavic	-0.304	0.642	0.709	20.5
25°C Equil Gas	11/15/12	Evap CO2-H2O 25C				
Heated Gas	11/15/12	Evap HG				
25°C Equil Gas	11/16/12	AAS CO2-H2O 25C				
Heated Gas	11/16/12	MDIW HG				
Heated Gas	11/17/12	AAS HG				
25°C Equil Gas	11/18/12	MDIW CO2-H2O 25C				
25°C Equil Gas	11/19/12	Evap CO2-H2O 25C				
Heated Gas	11/19/12	Evap HG				
Sample	11/19/12	Muroc	-0.272	0.676	0.743	9.5
Sample	11/19/12	Lavic	-0.284	0.664	0.731	13.3
25°C Equil Gas	11/20/12	AAS CO2-H2O 25C				
Heated Gas	11/20/12	Evap HG				
Sample	11/20/12	Muroc	-0.293	0.654	0.721	16.4
Sample	11/20/12	Lavic	-0.277	0.671	0.738	11.1
Heated Gas	11/21/12	MDIW HG				
25°C Equil Gas	11/21/12	MDIW CO2-H20 25C				
Sept–Oct 2012						
Heated Gas	10/19/13	Math HG				
Heated Gas	10/19/13	AAS HG				
Heated Gas	10/20/13	BCoral HG				
Heated Gas	10/20/13	BCoral HG				
Heated Gas	10/20/13	Evap HG				
Heated Gas	10/20/13	MCB HG				
Heated Gas	10/20/13	Barbados Coral HG				
Heated Gas	10/21/13	Cararra HG				
Heated Gas	10/21/13	MCB HG				
Heated Gas	10/21/13	BCoral HG				
Heated Gas	10/21/13	Carerra HG				
Heated Gas	10/21/13	MCB HG				
Heated Gas	10/22/13	BCoral HG				
Heated Gas	10/22/13	Carerra HG				
25°C Equil Gas	10/22/13	AAS 25C				
25°C Equil Gas	10/22/13	MDIW 25C				
Heated Gas	10/22/13	Cararra HG				
25°C Equil Gas	10/22/13	Evap 25C				
Heated Gas	10/23/13	MCB HG				
Heated Gas	10/23/13	AAS HG				
25°C Equil Gas	10/23/13	AAS 25C				
25°C Equil Gas	10/23/13	Evap 25C				
25°C Equil Gas	10/23/13	MDIW 25C				
Standard	10/24/13	ActualCarerra				
Heated Gas	10/24/13	Evap HG				
25°C Equil Gas	10/24/13	AAS 25C				
Standard	10/24/13	Cararra 75C rxn				
25°C Equil Gas	10/25/13	Evap 25C				
Heated Gas	10/26/13	MCB HG				
25°C Equil Gas	10/26/13	MDIW 25C				
Heated Gas	10/28/13	MCB HG				
25°C Equil Gas	10/28/13	AAS 25C				
25°C Equil Gas	10/29/13	Evap 25C				
Heated Gas	10/29/13	Cararra HG				
Heated Gas	10/30/13	Barbados Coral HG				
25°C Equil Gas	10/30/13	MDIW 25C				
Standard	10/30/13	Cararra #1 75C BL				
Standard	10/31/13	Cararra #2 75C BL				
25°C Equil Gas	10/31/13	AAS 25C				
Heated Gas	10/31/13	Evap HG				
Standard	11/01/13	Cararra #3 75C WD				

Type	Date	Name	$\Delta_{47\text{-}[SGvsWG]0}$ ‰	$\Delta_{47\text{-}RF}$[a] ‰	$\Delta_{47\text{-}RF\text{-}AC}$[b] ‰	T[c] °C
Heated Gas	11/01/13	MCB HG				
25°C Equil Gas	11/01/13	MDIW 25C				
Heated Gas	11/03/13	AAS HG				
25°C Equil Gas	11/03/13	Evap 25C				
Standard	11/03/13	Carerra #4 75C WD				
25°C Equil Gas	11/04/13	AAS 25C				
Heated Gas	11/04/13	Evap HG				
Heated Gas	11/05/13	BCoral HG				
25°C Equil Gas	11/05/13	MDIW 25C				
Heated Gas	11/06/13	Cararra HG				
25°C Equil Gas	11/07/13	Evap 25C				
Heated Gas	11/08/13	MCB HG				
25°C Equil Gas	11/08/13	AAS 25 C				
Heated Gas	11/09/13	MDIW HG				
25°C Equil Gas	11/09/13	MDIW 25C				
Sample	11/10/13	Clamo	-0.343	0.630	0.696	24.8
Heated Gas	11/10/13	AAS HG				
25°C Equil Gas	11/10/13	Evap 25C				
Sample	11/10/13	Clamo	-0.328	0.647	0.714	18.9
Sample	11/10/13	Clamo	-0.335	0.639	0.706	21.6
25°C Equil Gas	11/11/13	AAS 25C BL				
Heated Gas	11/11/13	EVAP HG BL				

[a]Converted to the universal reference frame following the approach detailed in Dennis et al. (2011)

[b]All samples were reacted at 75°C, and an acid fractionation correction of 0.067 was used (Hren et al., 2013).

[c]Temperature calculated using the >70°C composite calibration of Defliese et al. (2015).

[d]Irregular heated gas, excluded from the reference frame calculations

Table A.6 Run intervals and corresponding transfer function values used

Run Interval[a]	Equilibrated Gas Line Slope	Empirical Transfer Function Slope	Empirical Transfer Function Intercept
May – June 2012			
May 13 – May 22	0.0316	1.1085	1.0453
May 24 – June 12	0.0316	1.0973	1.0315
October – November 2012			
Oct 24 - Nov 2	0.0252	1.0895	1.0035
Nov 3 - Nov 24	0.0282	1.0819	0.9711
October – November 2013			
Oct 19 - Oct 30	0.0250	1.1778	1.0602
Oct 31 - Nov 11	0.0288	1.0858	1.0029

[a]Change in slopes correspond to lab power outages and equipment shut-downs

Table A.7 Corrected stable isotope data and $\delta^{18}O$ soil water calculations

Site/Soil	$\delta^{13}C_{raw}$ (‰) VPDB	$\delta^{13}C_{ppq}$[a] (‰) VPDB	$\delta^{18}O_{raw}$ (‰) VSMOW	$\delta^{18}O_{ppq}$[a] (‰) VSMOW	$\delta^{18}O_{AF}$[b] (‰) VSMOW	$\delta^{18}O_{AF}$ (‰) VPDB	Δ_{47}-Temp. (°C)	$10^3 ln\alpha$[c]	$\delta^{18}O_{SW}$[d] (‰) VSMOW
Muroc	-5.6	-5.5	29.4	29.7	21.3	-9.4	11.7	31.371	-10.3
Lavic	-3.4	-3.3	28.2	28.6	20.1	-10.5	15.0	30.595	-10.6
Guvo	-3.7	-3.6	33.5	33.8	25.3	-5.4	16.3	30.286	-5.3
Cross-Apache	-6.5	-6.4	30.2	30.6	22.1	-8.5	6.8	32.585	-10.6
Cornville	-0.6	-0.5	28.9	29.2	20.7	-9.9	20.6	29.319	-8.7
Plughat–Pit 1	-6.4	-6.3	30.6	30.9	22.5	-8.2	5.6	32.883	-10.6
Plughat–Pit 2	-6.5	-6.4	29.7	30.0	21.5	-9.1	8.8	32.071	-10.7
Montecito	-4.5	-4.4	29.9	30.3	21.8	-8.8	5.8	32.832	-11.2
Witt	-5.0	-4.9	32.3	32.6	24.1	-6.6	9.0	32.039	-8.2
Kranzburg	-0.6	-0.5	33.7	34.0	25.5	-5.3	21.8	29.074	-3.9
Clamo	-0.7	-0.6	32.8	33.2	24.7	-6.1	13.1	31.038	-6.6

[a]Corrected for temperature dependent fractionations associated with Porapak-Q column held at -25°C (Petersen et al., 2016)
[b]Corrected using the acid fractionation factor of 1.00830 for calcite reacted at 75°C (Swart et al., 1991)
[c]Calcite-water fractionation factor of Friedman and O'Neil (1977) using the Δ_{47}-Temp
[d]Calculated $\delta^{18}O$ of the soil water using the corresponding calcite-water fractionation factor

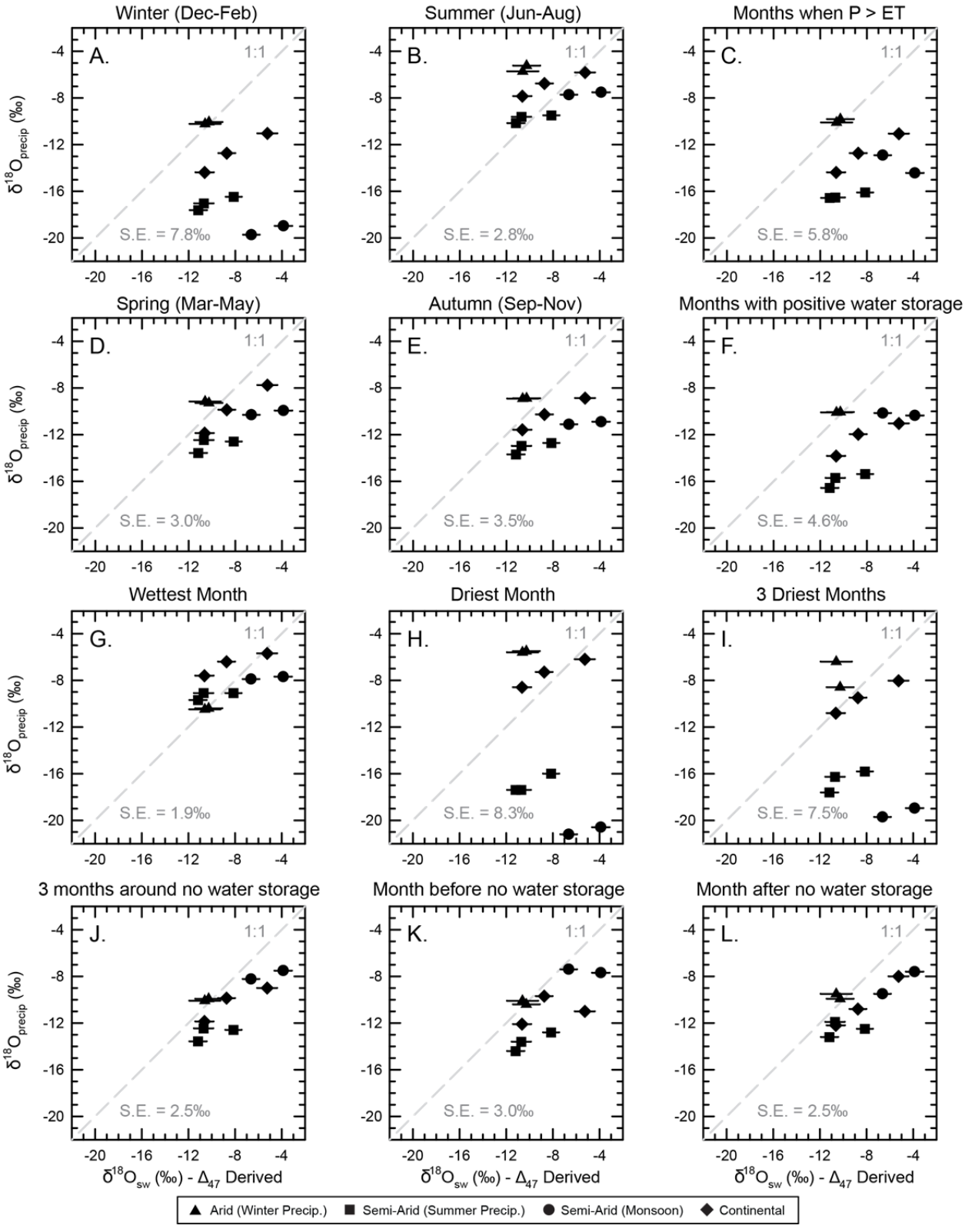

Figure A.1 Additional plots of calculated $\delta^{18}O$ values of the soil water ($\delta^{18}O_{sw}$) plotted against different scenarios of OIPC-derived weighted $\delta^{18}O$ values of precipitation ($\delta^{18}O_{precip}$). Standard Error (S.E.) calculated relative to the 1:1 line.

Appendix B

Supplemental Data for Chapter 3

Table B.1 SCAN stations, climate normal stations, and excluded data

Scan Station	Climate Normal Station		Soil Moisture Data		Soil Temperature Data	
	Temperature	*Precipitation*	*51 cm*	*102 cm*	*51 cm*	*102 cm*
2021	454679	454679				
2198	94129	94129				
2074	355174	355174				
2218	Excluded	Excluded				
2214	48873	48873				
2192	48873	48873				
2215	40943	40943				
2149	40684	44881				
2191	43369	45280				
2187	42331	42331				
2217	43083	43083				
2190	48200	48200		Excluded		
2186	263316	263316				
2189	46154	46154			Excluded	
2219	46154	46154				
2185	Excluded	Excluded				
2183	42410	42410		Excluded		Excluded
2184	42410	42410				
674	106174	106174		Excluded		Excluded
2148	108412	357736	Excluded	Excluded	Excluded	Excluded
750	4139	4139		Excluded		Excluded
2216	Excluded	Excluded		Excluded		Excluded
2116	264698	264698				
2170	260507	260507				
2143	Excluded	Excluded		Excluded		Excluded
2144	Excluded	Excluded				
2145	265400	265400				
2142	265400	265400				
2141	265400	265400				
2146	265400	265400	Excluded	Excluded	Excluded	Excluded
2160	423486	423486				
2153	427408	427408				
2135	428668	428668				
2136	421918	421918				
2151	4111	4111		Excluded		Excluded
2150	4111	4111				
2133	425826	425826				
2152	423348	423348				
2154	424342	424342				
2134	420074	420074				
2155	422253	422253				
2167	422257	422257	Excluded			
2165	424174	424174				
2137	426135	426135				
2132	427026	93141				
2126	422578	422578				
2163	422607	422607				
2127	426357	426357				
2131	423418	423418				

Scan Station	Climate Normal Station		Soil Moisture Data		Soil Temperature Data	
	Temperature	*Precipitation*	*51 cm*	*102 cm*	*51 cm*	*102 cm*
2164	429152	429152				
2129	23176	23176				
2156	420527	412012				
2125	421432	421432				
2166	424947	424947				
2139	425805	425805				
2130	421308	421308				
2138	420738	420738				
2140	420738	420738				
2158	422592	422592				
2157	426601	426601				
2162	426534	428847				
2161	426181	Excluded				
2128	422558	422558				
2159	424968	424968				
2026	28619	28619				
2019	243110	243110				
2118	248233	248233				
2117	241974	241974				
2120	247560	247560				
581	245045	248169				
2121	241231	94051				
2119	245761	245761				
808	248363	245123				
2018	94053	94053				
2017	94074	94074				
2197	94074	94074				
2172	290245	290245				
2169	295150	295150				
2171	290915	290915				
2015	292095	292096				
2108	291445	291445				
2107	292207	292207				
2168	294426	3074				
2020	325479	325479				
2072	4990	4990				
2001	94995	94995				
2111	256552	254110				
2093	146378	146378				
2094	141408	141408				
2147	3997	3997				
2092	13932	13932				
2022	342818	342818				
2006	411267	411267				
2202	419346	419346	Excluded	Excluded	Excluded	Excluded
2201	410708	416146				
2104	418232	23042				
2105	415183	415183				
2106	416074	416074				
2203	3969	3969				
2200	416499	416499				
2199	415611	415611		Excluded		
2207	410613	410613				
2016	410655	410655				
2204	414907	411007				
2206	12928	12928				
2205	419588	419588	Excluded	Excluded	Excluded	Excluded
2050	216787	216787				
2002	14926	14926				
2068	133909	133909				
2031	130200	130200				
2047	237963	237963				
2061	232568	232568				
2195	231482	235541				
2220	232591	232591	Excluded	Excluded	Excluded	Excluded
2193	232511	232511				
2060	235862	235862		Excluded		
2194	238583	238583				

Scan Station	Climate Normal Station		Soil Moisture Data		Soil Temperature Data	
	Temperature	*Precipitation*	*51 cm*	*102 cm*	*51 cm*	*102 cm*
2048	230735	235207				
2085	53959	53959				
2090	33200	34938				
2030	31102	31102				
2084	34638	34638				
2091	36920	36920				
2083	35754	35754				
2003	474582	474582				
2196	476646	476646				
2004	113940	113940				
2034	228998	228998				
2024	222773	220488				
2025	222773	220488				
2035	224869	224869				
2046	221743	221743				
2064	228374	228374				
2109	221738	221738				
2070	30234	13939				
2032	226009	226009				
2086	220660	220660				
2087	227560	227560				
2110	229860	229860				
2033	227560	227560				
2082	229157	53858				
2005	156580	156580				
2079	151391	155097				
2077	409800	409800				
2075	403074	403074				
2076	407459	407459				
2053	403074	403074				
2078	403074	403074				
2057	3856	3856				
2173	224455	224455				
2055	13575	63866				
2056	12840	12840				
2113	12096	63867				
2179	13620	13620				
2175	18608	10369				
2174	10184	10178				
2114	14798	14798				
2176	14274	63897				
2177	15553	15553		Excluded		
2178	15439	15439				
2115	15439	15439				
2182	92738	92738				
2181	10402	10402				
2180	16988	16988				
2073	336389	336389				
2014	334681	334681				
2013	98950	98950				
2027	98703	98703				
2009	88756	88756				
2012	85076	85076				
2051	84095	84095	Excluded	Excluded	Excluded	Excluded
2069	273415	270681				
2043	273530	273530				
2041	Excluded	Excluded				
2042	439591	Excluded				
2011	303184	303184				
2036	368449	368449				
2028	367931	367931				
2049	183675	183675				
2039	446712	446712				
2088	445685	444876				
2040	444044	444044				
2089	448170	448170				
2008	316853	316853				
2037	383111	383111				

Scan Station	Climate Normal Station		Soil Moisture Data		Soil Temperature Data	
	Temperature	*Precipitation*	*51 cm*	*102 cm*	*51 cm*	*102 cm*
2038	92055	383906				
2052	664702	664702		Excluded		Excluded
2188	662934	662934				
2112	666073	666073	Excluded	Excluded	Excluded	Excluded
15	665908	665908				
2045	Excluded	Excluded	Excluded	Excluded		
2122	667292	667292				
2067	662316	665693	Excluded	Excluded	Excluded	Excluded
2066	665097	665097				
2123	11624	11624				
965	26616	26642		Excluded		Excluded
2212	26533	26533	Excluded	Excluded	Excluded	Excluded
2213	26617	26617				
2210	503212	503212	Excluded	Excluded	Excluded	Excluded
2081	26435	26435				
2221	26502	26502	Excluded	Excluded	Excluded	Excluded
2211	26502	26502	Excluded	Excluded	Excluded	Excluded
2080	509313	509313				
2065	26615	26615				
2208	26615	26615				
2062	503682	503682		Excluded		Excluded
1233	25506	25506				
1232	26615	26615				
1234	502457	502457				
2209	25503	25503				
2097	Excluded	Excluded				
2099	Excluded	Excluded				
2102	Excluded	Excluded				
2103	Excluded	Excluded				
2100	514459	514459				
2098	Excluded	Excluded		Excluded		Excluded
2101	Excluded	Excluded		Excluded		Excluded
2096	518552	512751		Excluded		Excluded

Table B.2 Average maximum and minimum monthly air and soil temperatures

SCAN Site	Monthly Avg. Air Temperature		Monthly Average Soil Temperature			
			51 cm		*102 cm*	
	Max (°C)	*Min (°C)*	*Max (°C)*	*Min (°C)*	*Max (°C)*	*Min (°C)*
2021	21.6	-1.7	23.5	2.9	21.1	5.3
2198	18.7	-1.1	19.6	2.6	17.6	4.4
2074	19.1	-0.4	21.2	2.3	19.5	3.6
2218			24.8	6.3	22.1	8.0
2214	18.4	-3.1	22.7	1.1	24.0	1.4
2192	18.4	-3.1	22.9	0.8	20.7	2.7
2215	13.3	-5.2	15.8	1.0	14.5	2.5
2149	20.3	-1.2	24.6	5.1	23.8	6.5
2191	16.4	-2.5	22.2	4.7	22.5	9.9
2187	24.1	0.0	25.7	3.5	23.3	6.2
2217	26.7	8.3	34.3	11.6	31.9	15.1
2190	32.8	9.3	36.0	11.5	32.9	13.4
2186	29.9	5.6	31.6	9.1	28.8	11.3
2189	24.2	8.1			30.8	15.4
2219	24.2	8.1	30.1	10.1	27.9	14.1
2185			34.9	12.6	33.0	13.4
2183	34.0	11.5	38.8	16.7		
2184	34.0	11.5	36.8	17.3	34.7	21.0
674	24.3	-1.3	24.5	1.6		
2148	21.4	-2.3				
750	17.0	-2.5	20.5	4.0		
2216			19.8	1.0		
2116	23.3	-0.8	23.0	4.6	19.3	8.2
2170	21.9	-0.6	19.1	0.8	16.3	2.9
2143						
2144						
2145	18.2	-0.1	17.7	1.8	15.8	3.5
2142	18.2	-0.1	18.0	2.8	15.4	4.7
2141	18.2	-0.1	21.6	2.2	20.0	3.5
2146	18.2	-0.1				
2160	20.6	-4.8	20.5	2.1	19.1	3.5
2153	22.3	-3.8	22.9	1.6	20.5	4.3
2135	22.6	-6.1	22.6	2.2	19.7	4.0
2136	23.4	-4.6	18.3	1.9	16.2	3.7
2151	19.2	-6.2	18.1	0.5		
2150	19.2	-6.2	15.9	0.7	14.1	2.1
2133	21.8	-4.3	19.6	1.1	18.1	1.9
2152	25.3	-2.6	22.9	5.2	21.2	7.9
2154	22.8	-7.9	25.1	-0.2	22.3	2.1
2134	20.2	-6.6	17.5	1.4	15.8	2.8
2155	21.5	-6.7	21.3	0.2	18.8	2.1
2167	25.6	-2.8	23.6	2.4	22.7	3.2
2165	20.9	-2.7	21.9	0.5	20.0	3.7
2137	23.7	-2.1	22.4	2.5	20.2	4.1
2132	23.3	-4.0	24.7	0.1	22.8	2.4
2126	20.6	-5.6	19.2	1.7	17.6	3.4
2163	24.2	-2.2	30.4	1.2	27.7	3.9
2127	25.8	-1.9	24.9	1.6	23.0	4.7
2131	26.6	-2.6	29.6	-1.0	26.8	2.4
2164	24.8	-1.8	24.3	1.5	22.1	4.4
2129	23.6	-2.3	22.7	3.0	20.5	5.5
2156	26.0	5.4	20.4	1.7	18.2	3.4
2125	21.7	-1.9	20.0	0.4	17.7	3.8
2166	21.4	-3.3	21.5	1.3	19.0	3.4
2139	20.5	-3.9	21.0	0.4	19.1	2.3
2130	21.7	-2.6	20.4	2.1	19.1	3.7
2138	24.6	0.1	23.0	1.9	21.7	2.8
2140	24.6	0.1	25.2	2.9	23.8	5.5
2158	23.3	-0.9	24.9	2.3	22.1	3.5
2157	18.5	-5.5	16.3	0.4	14.1	3.3

SCAN Site	Monthly Avg. Air Temperature		Monthly Avg. Air Temperature			
			51 cm		*102 cm*	
	Max (°C)	*Min (°C)*	*Max (°C)*	*Min (°C)*	*Max (°C)*	*Min (°C)*
2162	20.6	-1.1	19.9	1.1	17.9	2.8
2161			22.5	1.3	20.3	2.3
2128	22.8	-2.1	23.7	2.0	21.3	4.9
2159	29.0	5.1	30.0	4.9	27.5	7.7
2026	26.3	8.7	28.0	12.0	26.7	14.8
2019	21.3	-7.0	20.2	1.1	17.7	2.6
2118	20.5	-5.9	21.3	-0.8	18.8	1.3
2117	18.8	-5.6	18.7	-0.6	16.7	1.6
2120	22.3	-8.2	18.7	-0.8	16.6	0.8
581	20.4	-7.9	19.9	-0.2	17.6	1.4
2121	21.1	-8.2	21.6	-1.3	20.1	0.7
2119	18.9	-4.1	18.3	1.3	17.0	2.2
808	18.8	-6.7	18.7	0.8	16.3	2.5
2018	23.3	-2.7	23.6	0.7	21.5	3.1
2017	21.4	-2.9	22.4	0.9	21.0	3.4
2197	21.4	-2.9	22.8	0.2	20.4	1.9
2172	21.9	-1.1	26.1	1.7	23.0	4.5
2169	25.0	1.6	26.0	5.5	24.7	7.6
2171	25.6	1.9	28.1	5.0	26.2	7.6
2015	20.8	0.6	24.3	4.7	22.2	6.4
2108	24.9	3.6	28.4	5.9	27.0	7.3
2107	24.9	3.5	28.2	6.2	26.6	9.4
2168	26.2	3.8	29.3	8.0	27.3	11.4
2020	21.4	-10.7	16.4	-0.2	14.0	1.8
2072	22.1	-9.6	19.5	-0.2	17.3	1.0
2001	24.7	-4.4	22.0	2.1	19.6	3.5
2111	23.6	-3.5	21.5	1.0	19.7	3.0
2093	26.6	-1.7	22.8	2.8	20.9	4.6
2094	24.8	-3.7	21.3	3.7	19.7	5.8
2147	25.7	-1.5	23.1	3.3	21.2	5.5
2092	27.1	0.9	25.0	4.9	23.9	6.7
2022	27.3	2.2	23.1	6.2	21.8	7.8
2006	24.7	1.7	23.9	5.6	22.4	7.7
2202	29.1	4.9				
2201	28.9	6.0	30.8	6.1	29.0	8.8
2104	26.8	4.6	27.9	7.0	25.9	9.1
2105	26.1	4.1	28.0	7.0	26.2	9.3
2106	25.6	3.9	29.0	7.4	27.2	9.1
2203	28.1	6.5	28.0	8.1	26.4	10.4
2200	28.1	7.2	30.0	9.6	28.2	12.6
2199	28.9	8.6	29.0	11.7	27.0	13.7
2207	28.4	10.9	28.6	11.9	27.0	14.2
2016	28.6	10.2	28.2	13.8	27.0	15.0
2204	28.7	10.8	27.7	12.2	27.8	15.9
2206	29.6	14.0	30.3	14.8	28.1	16.6
2205	30.1	15.5				
2050	20.2	-14.6	16.7	-0.5	15.3	1.4
2002	21.3	-11.3	17.9	-0.5	16.6	0.8
2068	23.1	-7.6	21.1	0.7	18.7	2.7
2031	23.3	-6.3	17.3	2.8	15.9	3.6
2047	24.6	-4.6	22.2	3.7	20.6	5.3
2061	24.9	-2.3	23.6	5.1	22.3	6.4
2195	25.2	-1.8	23.3	2.7	21.0	5.2
2220	25.4	-0.9				
2193	25.7	-0.1	23.9	5.1	21.8	6.7
2060	25.4	0.3	24.4	5.2	23.5	6.8
2194	24.9	0.2	22.1	3.8	21.6	5.2
2048	27.0	1.7	26.2	5.8	24.4	7.3
2085	27.2	3.7	28.7	7.1	26.0	9.2
2090	27.0	3.4	27.1	7.8	25.5	9.1
2030	27.1	4.1	26.9	8.4	25.0	9.5
2084	27.5	4.2	28.1	8.1	26.2	9.6
2091	27.6	4.3	28.2	8.4	26.8	9.7

SCAN Site	Monthly Avg. Air Temperature		Monthly Avg. Air Temperature			
			51 cm		*102 cm*	
	Max (°C)	*Min (°C)*	*Max (°C)*	*Min (°C)*	*Max (°C)*	*Min (°C)*
2083	27.8	5.3	27.5	9.2	26.1	10.3
2003	18.0	-11.1	14.6	1.8	13.2	2.5
2196	22.1	-7.9	19.4	0.2	17.3	2.0
2004	24.8	-3.7	23.6	3.0	22.4	3.9
2034	27.9	4.7	25.8	7.9	24.6	10.4
2024	26.7	4.4	24.7	8.3	24.4	10.3
2025	26.7	4.4	22.7	9.3	21.2	10.2
2035	27.8	4.7	27.4	8.4	26.2	9.6
2046	27.8	5.2	28.6	8.7	26.4	10.7
2064	27.3	5.6	27.4	9.7	25.6	11.1
2109	27.8	5.0	31.0	8.4	29.5	9.6
2070	27.8	5.7	30.0	9.4	27.9	10.9
2032	27.8	5.9	28.1	10.1	25.8	11.1
2086	27.9	6.3	26.8	9.3	25.6	11.3
2087	27.9	6.7	28.8	10.7	26.5	13.1
2110	27.4	6.7	26.4	10.1	24.6	12.0
2033	27.9	6.7	28.5	10.5	26.4	12.1
2082	27.4	10.3	27.0	14.3	26.2	15.1
2005	25.9	2.3	23.8	6.5	22.7	7.4
2079	25.8	2.7	24.5	6.2	22.3	7.0
2077	24.7	3.7	23.7	6.9	22.2	8.1
2075	26.1	4.4	25.4	7.1	23.4	8.3
2076	25.4	2.8	22.9	6.9	22.2	9.3
2053	26.1	4.4	25.3	8.0	22.5	10.7
2078	26.1	4.4	25.3	7.8	23.6	8.6
2057	27.0	5.3	25.0	7.2	23.5	8.5
2173	25.4	3.3	27.2	7.2	24.8	8.9
2055	26.6	5.1	25.5	7.8	23.4	9.4
2056	26.2	4.3	23.8	7.9	23.4	9.1
2113	25.5	4.4	26.9	8.6	25.4	9.4
2179	27.3	5.8	26.0	7.8	25.0	8.9
2175	25.6	5.6	26.9	10.1	26.1	10.5
2174	27.2	6.3	26.5	9.7	25.3	11.4
2114	27.1	6.9	28.0	11.2	26.8	12.1
2176	27.1	7.3	28.7	10.8	27.5	12.2
2177	27.2	7.9	28.1	11.5	26.2	12.8
2178	27.4	7.6	29.3	10.2	26.3	12.6
2115	27.4	7.6	29.2	11.5	27.7	12.5
2182	28.4	9.9	27.4	13.2	26.6	14.5
2181	27.3	8.9	27.3	11.5	26.5	12.9
2180	27.3	9.7	28.8	13.3	27.8	14.4
2073	22.8	-1.9	21.2	1.5	20.0	3.5
2014	22.8	-3.1	21.4	4.1	19.4	5.4
2013	26.4	5.4	25.1	8.7	24.1	9.7
2027	27.1	8.9	28.7	12.2	27.3	13.8
2009	27.9	10.4	27.0	13.5	25.9	14.6
2012	27.7	13.7	29.9	17.0	29.6	17.9
2051	28.0	18.8				
2069	19.0	-8.7	15.1	2.5	13.8	3.3
2043	18.9	-8.8	14.6	2.1	13.4	3.0
2041			14.1	2.0	13.0	2.9
2042			14.1	2.0	12.8	2.9
2011	21.4	-4.7	20.3	3.3	18.5	4.0
2036	22.3	-2.7	21.0	2.7	18.7	3.3
2028	22.8	-2.6	22.6	2.0	21.8	3.0
2049	24.8	0.2	24.3	4.3	21.0	5.3
2039	24.7	1.3	25.3	5.4	23.0	7.2
2088	24.0	1.1	21.9	3.9	20.9	5.9
2040	26.2	4.3	25.7	8.1	24.6	8.3
2089	24.1	2.7	24.4	5.7	23.2	6.8
2008	26.5	6.2	26.6	9.2	24.8	10.6
2037	27.7	6.7	27.5	10.3	26.3	11.1
2038	27.6	8.9	27.8	11.6	26.6	12.9

SCAN Site	Monthly Avg. Air Temperature		Monthly Avg. Air Temperature			
			51 cm		*102 cm*	
	Max (°C)	*Min (°C)*	*Max (°C)*	*Min (°C)*	*Max (°C)*	*Min (°C)*
2052	26.7	23.3	28.1	23.9		
2188	26.6	22.8	26.7	23.6	26.5	23.9
2112	27.2	24.2				
15	23.3	20.3	22.1	20.4	22.2	21.0
2045			22.5	20.1	21.4	19.6
2122	28.1	24.8	30.6	25.9	29.9	26.3
2067	28.6	25.4				
2066	27.3	23.6	29.5	24.9	28.9	25.8
2123	28.8	25.7	29.2	26.3	28.9	26.7
965	10.1	-19.1	3.3	-7.4		
2212	15.4	-23.3				
2213	11.2	-14.9	2.7	-12.4	0.2	-11.7
2210	15.9	-22.9				
2081	16.1	-21.2	11.3	-2.8	9.0	-0.7
2221	14.2	-21.3				
2211	14.2	-21.3				
2080	15.3	-24.1	10.6	-5.7	7.5	-4.2
2065	13.4	-14.1	7.1	-2.6	5.5	-0.6
2208	13.4	-14.1	0.6	-5.2	-0.5	-4.0
2062	12.4	-4.8	6.2	0.5		
1233	13.4	-8.1	5.6	-2.8	2.2	-1.6
1232	13.4	-14.1	7.0	-1.2	5.7	-0.2
1234	12.8	-9.4	9.9	-0.7	9.0	0.1
2209	13.1	-8.8	7.7	-0.3	5.5	0.2
2097			23.4	20.5	23.4	21.0
2099			19.5	17.8	19.3	18.0
2102			18.7	15.8	18.7	16.6
2103			19.4	17.0	20.4	18.5
2100	23.1	19.8	22.6	19.5	22.2	19.8
2098			13.2	10.2		
2101	9.6	5.8	14.6	9.6		
2096	22.1	19.8	24.7	21.8		

Table B.3 Driest 30-day intervals and corresponding soil temperatures

SCAN Site	MAAT (°C)[a]	Driest 30-day Interval				Largest 30-day Soil Moisture Decline			
		51 cm		*102 cm*		*51 cm*		*102 cm*	
		First Day[b]	*Temp (°C)*	*First Day*[b]	*Temp (°C)*	*First Day*[b]	*Temp (°C)*	*First Day*[b]	*Temp (°C)*
2021	9.9	38	8.2	1	6.0	125	14.4	154	15.8
2198	8.6	283	11.5	37	9.4	141	14.6	157	13.9
2074	8.7	278	12.8	296	11.4	215	21.1	153	14.5
2218		298	13.4	313	12.9	99	14.0	155	18.4
2214	7.0	38	2.6	345	1.3	34	4.4	286	1.4
2192	7.0	247	18.6	247	18.6	158	19.9	164	17.8
2215	3.2	3	1.6	322	4.9	179	15.9	217	
2149	9.1	324	8.0	325	9.9	16	14.8	111	14.0
2191	5.9	38	9.6	167	2.8	13	16.0	149	18.8
2187	11.9	34	4.2	5	6.2	171	25.2	351	6.9
2217	17.6	1	11.6	334	16.7	298	19.9	199	31.5
2190	20.9	1	11.5			35	11.2		
2186	17.2	1	1.9	4	11.4	35	9.3	35	12.6
2189	15.3			2	16.9			346	16.5
2219	15.3	1	1.3	18	14.2	35	9.6	281	24.2
2185		39	18.5	15	23.7	251	31.8	211	33.1
2183	22.7	1	16.7			35	16.6		
2184	22.7	349	17.5	336	22.4	313	22.8	151	31.1
674	10.8	298	9.6			127	14.5		
2148	8.6								
750	6.1	38	7.9			134	13.5		
2216		312	4.3			146	14.0		
2116	10.7	341	6.3	249	20.0	314	1.1	189	17.9
2170	9.4	292	7.7	351	4.7	148	14.4	154	12.7
2143		328	-1.5			313	-0.6		
2144		326	7.6	326	9.9	121	14.7	132	13.7
2145	8.1	311	5.8	324	7.1	289	9.3	81	4.8
2142	8.1	32	5.8	328	7.7	115	1.2	173	14.1
2141	8.1	182	21.4	216	20.0	6	5.7	118	12.3
2146	8.1								
2160	7.3	318	4.9	352	4.4	152	15.3	166	15.7
2153	8.3	295	1.3	1	4.4	281	13.6	292	13.6
2135	7.7	321	4.7	336	6.3	17	2.5	24	19.7
2136	9.2	314	6.4	1	4.4	145	12.2	165	12.4
2151	5.5	339	1.9			163	15.2		
2150	5.5	32	4.2	224	14.2	165	13.1	162	1.8
2133	8.3	286	1.2	362	2.5	351	1.7	122	9.9
2152	10.6	329	8.7	5	8.4	123	13.4	351	9.9
2154	8.6	36	0.4	36	2.1	21	25.3	298	12.4
2134	6.7	336	2.2	337	4.1	149	13.6	161	13.4
2155	8.0	8	0.2	166	17.1	219	2.3	219	18.7
2167	10.8	43	4.5	12	3.4	8	2.5	233	21.7
2165	8.4	325	3.5	347	5.2	264	15.4	28	19.9
2137	10.2	327	5.4	3	5.0	18	1.4	29	13.6
2132	9.3	5	0.2	8	2.3	266	17.5	291	13.3
2126	7.2	1	1.8	35	3.4	121	1.7	21	17.2
2163	10.6	294	12.7	13	3.7	165	28.7	351	5.3
2127	11.1	332	4.5	22	4.6	115	13.4	267	18.8
2131	12.5	364	-1.9	3	2.3	294	11.3	276	18.3
2164	11.1	1	1.5	25	4.2	353	2.5	293	14.6
2129	10.2	7	2.8	22	5.5	295	11.9	291	14.9
2156	15.9	322	4.9	327	6.9	141	14.2	61	4.2
2125	9.4	329	4.2	25	3.7	143	15.3	169	15.2
2166	8.4	327	3.9	346	5.3	139	15.5	89	7.4
2139	7.9	1	0.5	12	2.6	118	1.8	214	19.6
2130	8.9	35	7.4	8	4.0	148	15.8	169	16.9
2138	11.8	356	2.4	1	3.4	114	12.6	351	4.5
2140	11.8	364	2.9	2	5.9	112	14.9	39	13.3
2158	10.8	36	9.8	34	5.7	12	16.2	314	9.2
2157	5.9	328	3.3	175	12.7	14	11.4	11	3.7

SCAN Site	MAAT (°C)[a]	Driest 30-day Interval				Largest 30-day Soil Moisture Decline			
		51 cm		*102 cm*		*51 cm*		*102 cm*	
		First Day[b]	*Temp (°C)*	*First Day*[b]	*Temp (°C)*	*First Day*[b]	*Temp (°C)*	*First Day*[b]	*Temp (°C)*
2162	9.0	213	19.9	325	6.2	138	14.9	152	14.2
2161		181	21.9	212	2.4	143	17.5	143	15.3
2128	9.6	325	5.9	325	9.7	117	14.0	166	18.2
2159	16.8	173	29.4	324	13.0	77	15.4	11	18.5
2026	17.6	36	18.5	12	14.8	217	26.8	346	16.0
2019	7.2	35	2.3	33	2.5	18	18.9	216	17.8
2118	7.2	25	-0.8	74	3.5	196	21.7	262	14.6
2117	6.2	14	-0.5	58	1.6	361	-0.6	1	2.3
2120	7.6	42	-0.8	52	0.7	178	17.9	47	0.8
581	5.9	229	18.6	321	5.2	185	2.6	183	17.0
2121	6.4	14	-1.2	42	0.7	168	19.6	213	2.7
2119	6.6	336	3.4	336	4.9	165	14.9	169	13.8
808	6.1	336	2.4	347	4.3	167	15.8	282	11.5
2018	9.3	16	0.6	251	18.9	154	19.5	158	17.5
2017	8.4	2	0.9	353	4.5	162	2.1	171	18.8
2197	8.4	36	0.1	336	3.8	149	18.4	161	17.2
2172	10.2	1	1.6	1	4.5	351	2.0	35	5.5
2169	13.2	4	5.6	15	7.6	184	25.8	319	13.0
2171	13.7	2	5.0	4	7.5	351	5.5	34	16.3
2015	10.5	19	5.3	357	6.6	35	4.7	125	16.6
2108	14.5	334	7.9	361	7.6	265	22.5	32	12.8
2107	14.6	363	6.1	17	9.2	148	26.7	258	24.0
2168	14.9	335	11.8	18	11.2	262	25.7	3	2.5
2020	5.9	39	-0.3	51	1.8	178	15.6	258	12.6
2072	7.2	39	-0.3	61	1.0	166	17.8	35	3.4
2001	10.5	213	22.0	235	19.4	197	22.8	196	19.1
2111	9.4	353	1.3	244	18.2	175	2.8	22	19.6
2093	11.9	334	6.4	346	7.6	162	19.3	161	16.2
2094	11.0	28	21.4	235	19.6	185	2.6	192	18.9
2147	12.7	2	23.6	311	12.8	16	21.2	184	2.3
2092	14.4	254	21.4	281	18.5	192	25.4	212	23.9
2022	14.8	25	23.2	265	19.5	14	19.8	188	2.9
2006	13.1	249	21.8	23	7.7	199	23.8	351	9.3
2202	17.2								
2201	17.7	33	15.4	27	1.5	193	3.6	27	28.8
2104	15.9	2	28.6	28	9.6	256	23.6	17	16.5
2105	15.2	1	7.0	336	11.7	149	25.3	318	14.3
2106	14.9	6	7.6	353	9.9	149	26.6	87	15.3
2203	17.6	257	25.8	274	23.8	196	27.8	25	26.2
2200	18.2	1	9.6	12	12.2	138	22.2	138	21.2
2199	19.2	268	23.5			29	29.4		
2207	20.4	217	28.4	238	26.4	22	28.9	223	26.9
2016	20.0	214	28.2	236	26.8	98	2.6	26	26.9
2204	20.3	1	12.2	51	16.3	35	14.5	351	17.8
2206	22.6	215	3.4	241	28.9	186	28.7	78	19.1
2205	23.6								
2050	4.2	39	-0.5	49	1.3	165	14.9	178	14.8
2002	6.1	39	-0.6	213	16.6	171	16.5	189	15.9
2068	8.6	45	0.7	1	4.1	357	1.8	35	5.7
2031	9.7	3	2.8	29	11.7	347	4.7	35	6.5
2047	10.7	25	22.3	323	2.0	187	21.9	212	2.6
2061	12.0	2	23.7	365	7.5	184	23.2	18	2.9
2195	12.3	292	13.8	72	6.5	359	4.2	232	2.7
2220	13.1								
2193	13.3	215	23.9	229	21.5	191	23.2	192	2.7
2060	13.3	228	23.7			22	24.5		
2194	13.0	23	21.7	236	21.2	159	19.8	186	2.5
2048	14.9	274	18.7	277	19.4	44	6.9	153	2.8
2085	16.1	231	27.5	38	9.3	162	26.8	182	24.4
2090	15.6	216	27.5	238	24.8	194	27.2	194	25.7
2030	16.1	214	27.0	267	22.2	164	25.7	25	24.8
2084	16.6	28	28.1	225	26.2	156	25.3	138	2.3
2091	16.6	24	28.2	24	26.6	152	25.6	56	11.1

SCAN Site	MAAT (°C)[a]	Driest 30-day Interval				Largest 30-day Soil Moisture Decline			
		51 cm		*102 cm*		*51 cm*		*102 cm*	
		First Day[b]	*Temp (°C)*	*First Day*[b]	*Temp (°C)*	*First Day*[b]	*Temp (°C)*	*First Day*[b]	*Temp (°C)*
2083	17.1	229	26.8	262	23.6	151	25.1	128	20.0
2003	4.4	257	12.1	262	11.4	18	13.8	191	12.7
2196	8.1	28	11.4	276	13.5	182	19.3	25	17.1
2004	11.4	213	23.7	253	2.3	176	23.0	198	22.4
2034	17.0	239	24.7	252	23.8	24	25.6	212	24.6
2024	16.2	253	22.4	248	23.2	195	24.8	164	22.8
2025	16.2	254	2.8	274	18.9	95	14.7	134	16.8
2035	17.1	229	26.7	239	25.6	167	26.9	142	21.7
2046	17.1	256	24.2	255	24.6	148	25.3	192	25.7
2064	16.9	222	27.1	25	2.0	187	27.2	327	15.3
2109	17.3	238	28.7	92	16.9	156	28.9	53	11.5
2070	17.4	214	3.4	214	27.9	23	3.4	94	16.7
2032	17.7	274	22.3	45	11.4	158	26.8	248	24.9
2086	18.0	268	21.9	263	23.4	213	26.8	173	24.7
2087	18.0	16	1.5	237	26.4	268	23.9	194	25.6
2110	17.7	17	10.0	26	12.1	194	26.7	263	23.4
2033	18.0	251	26.1	319	17.5	199	28.5	261	24.6
2082	19.4	31	19.3	37	19.8	266	24.1	266	24.5
2005	14.8	249	21.4	254	2.8	118	17.2	238	22.1
2079	14.9	217	24.5	213	22.3	193	24.6	161	20.0
2077	14.7	27	23.7	217	22.2	122	17.5	119	15.1
2075	15.7	219	25.4	219	23.4	118	17.9	144	18.9
2076	14.6	158	3.0	15	18.9	88	13.2	87	13.3
2053	15.7	241	23.6	235	22.6	92	15.0	13	16.8
2078	15.7	162	23.4	28	23.5	119	17.7	157	2.5
2057	16.7	165	23.6	29	23.4	124	18.7	119	16.3
2173	14.8	291	16.5	256	22.4	157	26.3	6	9.2
2055	16.4	227	24.9	239	23.0	188	25.2	26	23.2
2056	15.5	228	23.5	245	22.6	2	23.7	146	19.7
2113	15.4	187	26.6	23	25.2	166	25.8	123	18.7
2179	17.2	273	19.8	255	22.3	153	24.1	115	17.6
2175	16.0	235	26.7	235	25.5	357	1.6	6	12.5
2174	17.3	184	26.6	196	26.0	168	26.2	179	24.6
2114	17.4	267	23.8	275	23.1	145	25.1	141	22.8
2176	17.6	252	26.3	261	25.3	23	27.8	128	22.5
2177	18.1	178	27.3			126	23.4		
2178	18.0	32	17.3	32	19.1	42	12.3	45	13.0
2115	18.0	25	29.3	24	27.8	94	19.9	95	18.7
2182	19.9	229	26.6	23	26.6	15	3.0	18	2.4
2181	18.8	242	26.4	257	25.9	21	27.5	21	26.5
2180	19.1	27	23.6	25	27.8	68	17.4	189	27.5
2073	10.8	226	2.6	266	16.4	351	3.9	21	2.1
2014	10.4	256	18.1	258	17.6	237	2.2	26	19.4
2013	16.2	14	2.8	231	24.0	124	18.8	24	9.8
2027	18.6	295	19.8	31	2.5	358	12.5	98	19.4
2009	19.8	127	23.6	136	22.7	218	26.9	72	18.2
2012	21.4	132	28.4	129	27.3	79	23.1	272	27.1
2051	23.8								
2069	5.9	33	2.6	33	3.7	11	5.7	17	5.8
2043	5.7	232	14.3	231	13.5	11	5.7	157	1.2
2041		236	13.6	24	12.9	113	5.6	362	3.9
2042		243	13.2	252	12.2	17	4.6	156	9.5
2011	8.7	273	14.5	236	18.2	179	19.8	113	9.7
2036	10.1	21	21.2	264	16.0	98	10.0	1	7.8
2028	10.3	216	22.5	217	21.7	99	1.4	348	5.6
2049	12.6	239	22.4	237	2.5	224	23.5	36	7.1
2039	13.2	215	25.3	217	23.1	143	21.7	15	18.7
2088	12.7	197	22.6	215	2.9	155	19.8	154	17.9
2040	15.4	192	25.7	221	24.5	134	2.5	167	23.0
2089	13.7	218	24.2	219	23.2	195	24.6	357	8.5
2008	16.6	164	25.4	192	24.2	144	23.3	351	12.7
2037	17.5	163	26.2	212	26.3	11	19.0	16	17.5
2038	18.5	125	23.7	127	21.9	92	19.4	92	18.4

SCAN Site	MAAT (°C)[a]	Driest 30-day Interval				Largest 30-day Soil Moisture Decline			
		51 cm		*102 cm*		*51 cm*		*102 cm*	
		First Day[b]	*Temp (°C)*	*First Day*[b]	*Temp (°C)*	*First Day*[b]	*Temp (°C)*	*First Day*[b]	*Temp (°C)*
2052	25.1	58	24.8			259	27.5		
2188	24.9	199	26.7	96	24.8	188	26.7	325	25.6
2112	26.0								
15	21.9	59	2.4	46	21.1	31	21.6	31	22.8
2045									
2122	26.6	135	29.9	13	29.2	344	26.7	351	26.5
2067	27.2								
2066	25.7	35	25.6	36	26.0	345	25.2	31	27.6
2123	27.2	199	28.9	99	27.4	15	28.3	184	28.2
965	-5.8	38	-6.1			199	0.7		
2212	-4.7								
2213	-2.6	21	-14.3	25	-12.5	296	-0.2	282	-0.4
2210	-3.3								
2081	-2.7	44	-2.8	88	-0.7	343	-3.0	351	0.3
2221	-3.8								
2211	-3.8								
2080	-3.9	32	-5.4	54	-4.9	298	-0.7	33	-0.7
2065	-0.7	43	-2.3	112	-0.6	162	1.9	31	-0.8
2208	-0.7	69	-5.8	7	-4.7	337	-0.3	34	-1.4
2062	3.3	22	0.6			1	0.8		
1233	2.1	65	-2.3	81	-1.4	37	-0.3	9	-1.2
1232	-0.7	31	-1.1	27	0.2	13	-0.7	157	-0.2
1234	1.3	73	-0.7	74	0.2	13	-0.2	342	1.3
2209	1.8	75	-0.3	78	0.3	33	-0.9	284	3.4
2097		156	22.8	28	23.3	12	21.4	23	23.4
2099		299	19.2	195	19.2	231	19.6	152	18.7
2102		22	18.7	237	18.7	98	16.8	229	18.7
2103		18	18.9	24	2.3	153	18.5	99	18.7
2100	21.7	274	22.3	253	22.2	78	19.9	144	3.0
2098		233	13.1			351	1.8		
2101		281	13.5			127	12.9		
2096	21.0	336	22.5			319	23.1		

[a]MAAT–mean annual air temperature
[b]Listed day is the first day (1–365) of the 30-day interval

Appendix C

Supplemental Data and Figure for Chapter 4

Table C.1 Raw Clumped Isotope Data 1 of 2

Day	Date	Int.[a]	Name	$d^{13}C$	$d^{18}O$	d45	d46	d47	d48	d49
September 2014 run										
Heated Gasses and 25°C Waters										
1	9/9	1	MCBHG	-2.85	23.32	0.41	-11.256	-11.911	-14.707	8.5
1	9/9	1	MixHG	-3.08	25.14	0.25	-9.499	-10.249	-15.566	4.15
1	9/9	1	CararraHG	2.04	36.86	5.44	1.83	6.662	8.818	6.291
1	9/9	1	OoidsHG	4.34	37.36	7.62	2.313	9.491	16.855	2.893
1	9/9	1	AAS25C	-41.51	17.01	-36.09	-17.422	-55.164	-35.217	5.359
2	9/10	1	MixHG	-3.04	26.57	0.34	-8.11	-8.79	-17.448	8.411
2	9/10	1	MCBHG	-3.35	20.99	-0.135	-13.499	-14.698	-26.647	5.635
2	9/10	1	MDIWHG	-41.34	28.97	-35.539	-5.883	-44.328	-13.7	12.117
2	9/10	1	AAS25C	-41.19	17.96	-35.76	-16.509	-54.047	-33.31	11.596
2	9/10	1	Evap25C	-40.43	47.15	-34.1	11.674	-24.83	35.797	6.319
2	9/10	1	MDIW25C	-41.49	30.58	-35.631	-4.327	-42.071	-8.086	10.362
3	9/11	1	CararraHG	2.10	36.73	5.489	1.704	6.605	5.159	9.811
3	9/11	1	MixHG	-2.99	22.49	0.251	-12.055	-12.87	-30.131	9.655
3	9/11	1	Evap25C	-40.44	46.64	-34.13	11.177	-25.349	33.492	11.157
3	9/11	1	MDIW25C	-41.42	30.66	-35.561	-4.245	-41.883	-9.768	11.184
4	9/12	1	MixHG	-2.94	27.52	0.459	-7.2	-7.743	-16.278	9.873
4	9/12	1	MDIW25C	-41.52	30.26	-35.67	-4.637	-42.371	-9.213	10.28
4	9/12	1	MDIW25C	-41.34	30.80	-35.483	-4.111	-41.67	-8.524	12.104
6	9/14	2	MCBHG	-3.08	22.31	0.163	-12.229	-13.104	-32.319	39.987
6	9/14	2	AAS25	-41.66	15.35	-36.28	-19.028	-56.976	-48.441	15.571
7	9/15	2	CarraraHG	1.88	37.10	5.297	2.058	6.744	6.355	7.239
7	9/15	2	AAS25C	-41.48	17.31	-36.054	-17.139	-54.978	-43.085	12.317
8	9/16	2	CararraHG	2.11	37.61	5.527	2.552	7.475	7.937	7.971
8	9/16	2	Evap25	-40.50	46.96	-34.171	11.49	-25.106	30.507	9.12
9	9/17	2	Evap25C	-41.39	46.40	-35.028	10.948	-26.552	28.88	8.238
10	9/18	2	MixHG	-3.09	24.95	0.244	-9.677	-10.485	-24.863	8.803
11	9/19	2	MCBHG	-3.05	21.82	0.172	-12.699	-13.609	-31.356	9.77
11	9/19	2	MDIW25C	-41.37	29.27	-35.562	-5.595	-43.208	-14.264	13.339
12	9/20	3	AASHG	-41.55	16.41	-36.142	-18.005	-56.782	-46.34	10.931
12	9/20	3	AAS25C	-41.36	17.11	-35.944	-17.328	-55.082	-45.269	16.377
14	9/22	3	MDIWHG	-41.24	26.66	-35.524	-8.105	-46.492	-20.759	10.947
14	9/22	3	AAS25	-41.45	17.37	-36.021	-17.072	-54.902	-45.649	23.501
15	9/23	3	CararraHG	2.02	33.60	5.312	-1.318	3.335	-3.535	8.089
15	9/23	3	Evap25C	-41.35	46.74	-34.977	11.27	-26.222	29.66	9.621
16	9/24	3	EVAPHG	-41.39	45.16	-35.067	9.744	-27.79	25.269	10.19
16	9/24	3	AAS25	-41.46	17.51	-36.026	-16.944	-54.785	-44.182	15.208
18	9/26	3	MDIWHG	-41.15	29.36	-35.349	-5.499	-43.793	-15.192	14.339
18	9/26	3	AAS25C	-41.57	17.24	-36.134	-17.199	-55.149	-43.67	14.154
19	9/27	3	AASHG	-41.34	16.96	-35.933	-17.472	-56.066	-44.062	12.093
19	9/27	3	Evap25C	-41.31	47.04	-34.928	11.56	-25.901	31.689	10.317
20	9/28	3	MixHG	-3.35	26.44	0.04	-8.247	-9.255	-21.547	10.202
20	9/28	3	AAS25C	-41.33	17.70	-35.896	-16.754	-54.52	-43.932	15.737
21	9/29	3	Carrara2HG	2.35	35.20	5.679	0.223	5.258	-0.597	10.267
21	9/29	3	MDIW25C	-41.26	30.66	-35.413	-4.249	-41.857	-11.468	12.923
23	10/1	3	EvapHG	-41.34	39.76	-35.194	4.534	-33.891	11.114	13.361

Day	Date	Int.[a]	Name	$d^{13}C$	$d^{18}O$	d45	d46	d47	d48	d49
Carbonate Standards										
3	9/11	1	Carrara1	1.78	36.45	5.183	1.426	6.308	4.789	5.048
3	9/11	1	Carrara2	1.96	37.03	5.374	1.994	7.116	6.363	4.853
16	9/24	3	Cararra3	1.97	37.09	5.38	2.047	7.119	4.746	8.162
22	9/30	3	Carrara4	1.70	36.17	5.102	1.161	5.953	2.844	8.006
Samples										
5	9/13	1	NS-WP-079-V	-9.00	24.70	-5.32	-9.936	-16.168	-24.087	9.861
5	9/13	1	NS-WP-148-V	-8.63	24.25	-4.982	-10.369	-16.195	-25.729	10.302
5	9/13	1	DO14-117-8-L	-4.94	31.23	-1.294	-3.626	-5.513	-9.192	8.647
5	9/13	1	NS-WP-421-J	-6.42	30.35	-2.713	-4.475	-7.914	26.775	7.451
5	9/13	1	NS-WP-148-N	-9.69	27.40	-5.874	-7.33	-14.102	3.309	6.918
7	9/15	2	NS-WP-079-V	-9.02	24.61	-5.335	-10.025	-16.287	-25.195	9.517
8	9/16	2	NS-WP-148-V	-8.65	24.22	-5	-10.396	-16.25	-26.639	10.903
8	9/16	2	DO14-117-8-L	-4.90	31.31	-1.257	-3.546	-5.399	-9.347	9.746
8	9/16	2	NS-WP-079-V	-9.31	24.04	-5.628	-10.569	-17.16	-27.534	10.923
8	9/16	2	NS-WP-421-J	-6.43	30.32	-2.725	-4.505	-7.961	6.465	8.119
8	9/16	2	NS-WP-148-N	-9.56	27.29	-5.763	-7.432	-14.083	-3.53	8.443
11	9/19	2	NS-WP-148-V	-8.93	24.32	-5.263	-10.297	-16.438	-26.975	10.698
11	9/19	2	DO14-117-8-L	-4.96	31.39	-1.305	-3.467	-5.357	-6.208	6.366
12	9/20	3	NS-WP-421-J	-6.56	30.32	-2.841	-4.501	-8.061	2.594	9.025
12	9/20	3	NS-WP-148-N	-9.68	27.36	-5.867	-7.365	-14.149	-13.098	10.31
16	9/24	3	NS-WP-079-V	-8.91	24.61	-5.236	-10.023	-16.203	-26.091	9.475
16	9/24	3	NS-WP-421-J	-6.44	30.36	-2.73	-4.464	-7.943	-2.011	9.65
16	9/24	3	NS-WP-148-N	-9.57	27.58	-5.756	-7.151	-13.801	-12.888	9.871
16	9/24	3	NS-WP-079-N	-8.03	28.95	-4.267	-5.825	-10.92	57.879	6.909
16	9/24	3	NS-WP-442-J	-8.02	30.24	-4.221	-4.585	-9.598	-8.844	9.171
21	9/29	3	NS-WP-442-J	-7.78	30.50	-3.98	-4.336	-9.107	-8.801	11.609
21	9/29	3	NS-WP-079-N	-7.70	28.97	-3.957	-5.806	-10.554	0.878	9.832
21	9/29	3	NS-WP-442-J	-7.95	30.15	-4.151	-4.675	-9.639	-10.236	9.905
22	9/30	3	NS-WP-079-N	-7.69	28.97	-3.952	-5.812	-10.534	8.849	5.759
December 2015 run										
Heated Gasses and 25°C Waters										
1	11/30	1	2xEVHG	-41.05	55.10	-34.433	19.345	-18.366	43.117	9.901
1	11/30	1	CarraraHG	1.91	29.47	5.075	-5.303	-0.957	-13.812	11.722
1	11/30	1	MDIWHG	-41.14	28.16	-35.378	-6.665	-44.381	-16.789	18.081
1	11/30	1	2xEV25C	-41.12	70.45	-34.01	34.153	-2.829	78.119	7.844
1	11/30	1	MDIW25C	-41.04	30.66	-35.205	-4.245	-41.07	-11.085	19.309
1	11/30	1	Evap25C	-41.05	47.56	-34.672	12.061	-24.807	26.907	13.02
2	12/1	1	2xEVHG	-41.00	58.52	-34.268	22.646	-15.029	53.083	-7.263
2	12/1	1	2xEV25C	-41.26	71.12	-34.12	34.799	-2.323	80.261	6.126
3	12/2	1	OoidsHG	4.41	36.59	7.652	1.573	8.694	26.203	3.286
3	12/2	1	MDIW25C	-41.39	30.17	-35.552	-4.72	-41.867	-11.533	14.261
4	12/3	1	EvapHG	-41.02	35.40	-35.033	0.33	-37.24	-0.491	15.538
5	12/4	1	CarraraHG	1.82	35.88	5.205	0.876	5.401	0.706	7.365
5	12/4	1	Evap25C	-41.02	47.43	-34.649	11.942	-24.885	26.746	12.8
6	12/5	1	MDIW25C	-41.05	30.44	-35.219	-4.463	-41.251	-11.197	20.901
7	12/6	1	EvapHG	-41.11	42.19	-34.896	6.876	-30.851	14.069	13.45
7	12/6	1	2xEV25C	-41.07	70.50	-33.961	34.208	-2.717	79.033	4.478
8	12/7	1	OoidsHG	4.25	32.07	7.358	-2.789	3.958	20.402	5.56
8	12/7	1	MDIWHG	-40.87	28.45	-35.12	-6.376	-43.819	-14.661	12.235
9	12/8	1	CarraraHG	2.09	31.65	5.32	-3.2	1.451	-8.889	10.069
9	12/8	1	Evap25C	-40.91	47.79	-34.528	12.287	-24.417	27.154	13.023
11	12/10	1	EvapHG	-41.08	44.59	-34.793	9.192	-28.538	19.784	13.012
11	12/10	1	MDIW25C	-41.19	30.06	-35.361	-4.831	-41.764	-10.742	10.731
12	12/11	1	2xEV25C	-41.14	71.17	-34.005	34.849	-2.173	80.53	7.15
13	12/12	1	2xEVHG	-40.96	65.30	-34.016	29.189	-8.446	66.634	9.761
Carbonate Standards										
2	12/1	1	Carrara1	1.91	36.95	5.316	1.909	6.831	3.03	10.315
2	12/1	1	Carrara2	1.96	37.03	5.366	1.99	7.002	3.439	9.453
2	12/1	1	Ooids1	4.70	39.09	8.006	3.98	12.038	8.529	0.336
2	12/1	1	Ooids2	4.77	39.28	8.08	4.166	12.3	8.651	8.885
4	12/3	1	Carrara3	1.71	36.40	5.119	1.384	6.129	1.971	2.199

Day	Date	Int.[a]	Name	d^{13}C	d^{18}O	d45	d46	d47	d48	d49
6	12/5	1	Ooids3	4.70	39.29	8.017	4.179	12.246	8.463	8.437
9	12/8	1	Carrara4	1.89	36.85	5.298	1.813	6.771	3.363	3.769
12	12/11	1	Ooids5	4.74	39.30	8.053	4.185	12.311	9.516	4.294
13	12/12	1	Carrara5	1.86	36.75	5.272	1.723	6.615	2.917	8.226
Samples										
5	12/4	1	NS-WP-338-V	-7.78	26.79	-4.106	-7.913	-12.61	-19.35	15.82
6	12/5	1	NS-WP-056-J	-6.91	30.19	-3.174	-4.631	-8.42	6.84	12.193
6	12/5	1	NS-WP-442-J	-7.92	30.16	-4.124	-4.661	-9.436	-10.437	14.002
6	12/5	1	NS-WP-338-V	-7.71	26.92	-4.038	-7.791	-12.422	-18.822	14.469
8	12/7	1	NS-WP-338-V	-7.66	26.81	-3.991	-7.898	-12.462	-19.2	14.825
8	12/7	1	PL-12-09	-2.35	21.69	0.832	-12.822	-12.437	-29.625	13.657
8	12/7	1	NS-WP-442-J	-7.88	30.12	-4.09	-4.7	-9.435	-11.355	13.696
8	12/7	1	PL-12-09	-2.15	21.73	1.017	-12.783	-12.269	-30.277	15.946
February 2016 run										
Heated Gasses and 25°C Waters										
1	2/22	1	EvapHGleaky	-41.11	39.39	-34.985	4.18	-33.598	7.883	12.412
1	2/22	1	2xEV25C	-41.08	70.60	-33.967	34.306	-2.656	79.343	2.481
1	2/22	1	CarraraHG	1.88	34.96	5.228	-0.006	4.519	-1.604	7.286
1	2/22	1	OoidsHG	4.33	26.17	7.241	-8.484	-1.872	-20.389	8.129
2	2/23	1	MDIW25C	-41.22	29.91	-35.397	-4.969	-41.99	-12.704	16.856
2	2/23	1	Evap25C	-41.34	46.12	-34.991	10.678	-26.479	23.864	8.748
2	2/23	1	MDIW25C	-41.08	30.51	-35.251	-4.397	-41.286	-11.259	16.578
2	2/23	1	2xEVHG	-41.11	50.75	-34.628	15.142	-22.602	34.089	6.075
3	2/24	2	EvapHG	-41.06	37.45	-35.006	2.31	-35.411	3.742	13.986
4	2/25	2	2xEV25C	-40.50	71.36	-33.405	35.04	-1.336	81.49	3.755
5	2/26	2	Evap25C	-40.70	46.99	-34.363	11.512	-25.041	25.73	9.713
5	2/26	2	MATHHG	-3.76	30.70	-0.2	-4.134	-5.273	-10.835	9.714
6	2/27	2	OoidsHG	4.70	36.17	7.915	1.163	8.549	0.986	8.425
7	2/28	2	MDIW25C	-40.79	30.42	-34.978	-4.482	-41.106	-11.644	16.389
7	2/28	2	2xEVHG	-40.64	62.14	-33.822	26.141	-11.247	60.416	8.875
8	2/29	2	2xEV25C	-40.67	71.17	-33.563	34.851	-1.731	84.043	-0.094
8	2/29	2	MATHHG	-3.96	30.07	-0.411	-4.736	-6.108	-11.757	8.733
9	3/1	2	Evap25C	-40.98	46.20	-34.645	10.749	-26.07	24.31	9.023
9	3/1	2	CarraraHG	0.00	34.98	3.467	0.007	3.187	0.286	9.486
10	3/2	2	MDIW25C	-40.93	30.28	-35.118	-4.612	-41.413	-11.897	13.825
11	3/3	2	OoidsHG	4.60	37.78	7.875	2.72	10.113	132.966	-11.829
12	3/4	2	2xEV25C	-40.57	71.10	-33.472	34.784	-1.665	82.303	2.754
13	3/5	3	EvapHG	-40.84	31.88	-34.98	-3.073	-40.624	-8.779	14.391
14	3/6	3	Evap25C	-40.92	46.19	-34.596	10.746	-26.068	24.492	10.685
14	3/6	3	MDIWHG	-40.76	26.64	-35.073	-8.127	-45.631	-20.715	14.095
Carbonate Standards										
2	2/23	1	Carrara1	1.94	36.93	5.347	1.89	6.832	2.76	9.783
2	2/23	1	Carrara2	1.94	37.02	5.355	1.981	6.93	3.099	10.417
2	2/23	1	Ooids1	4.82	39.32	8.126	4.211	12.359	8.401	8.5
4	2/25	2	Ooids3	4.76	39.37	8.077	4.252	12.374	8.63	7.465
6	2/27	2	Carrara3	1.85	36.97	5.261	1.931	6.834	3.199	8.836
8	2/29	2	Ooids4	4.53	39.10	7.854	3.991	11.861	8.135	7.016
10	3/2	2	Carrara4	1.95	37.06	5.361	2.02	7.021	3.639	6.665
12	3/4	2	Ooids5	4.69	39.33	8.011	4.219	12.309	8.974	5.238
14	3/6	2	Carrara5	1.92	36.93	5.328	1.891	6.846	3.039	8.055
Samples										
4	2/25	2	NS-WP-148-N001	-9.62	27.76	-5.798	-6.985	-13.517	-15.1	12.161
6	2/27	2	PI2-52-2	-12.15	30.58	-8.082	-4.266	-13.204	-10.879	9.374
6	2/27	2	WC18-47-9	-9.20	27.28	-5.419	-7.445	-13.646	-16.782	12.01
6	2/27	2	WC18-49-7	-2.86	31.59	0.671	-3.268	-3.068	-8.972	10.771
7	2/28	2	PI2-52-2	-12.35	30.43	-8.277	-4.411	-13.529	-11.451	11.28
7	2/28	2	WC18-49-7	-2.95	31.54	0.585	-3.319	-3.197	-9.202	10.192
9	3/2	2	WC18-49-7	-2.77	31.67	0.759	-3.197	-2.892	-8.906	9.941
10	3/2	2	PI2-50-2	-12.31	30.11	-8.246	-4.723	-13.838	-12.276	11.695
10	3/2	2	NS-WP-442-J	-7.58	30.25	-3.802	-4.573	-9.028	-9.403	9.319
10	3/2	2	PL-12-09	-2.63	21.45	0.562	-13.054	-12.967	-31.621	11.396

Day	Date	Int.[a]	Name	$d^{13}C$	$d^{18}O$	d45	d46	d47	d48	d49
13	3/5	2	DO6-62-9	-3.95	32.81	-0.315	-2.1	-2.92	-6.25	8.66
13	3/5	2	DO6-62-9	-4.16	32.41	-0.525	-2.481	-3.507	-7.242	8.73
13	3/5	2	PI2-50-2	-12.51	30.52	-8.424	-4.326	-13.623	-11.679	10.826
13	3/5	2	DO6-62-9	-4.10	32.73	-0.452	-2.173	-3.125	-6.413	8.422
14	3/6	2	CHC-12-04	-0.88	31.16	2.513	-3.682	-1.534	-10.113	9.01
14	3/6	2	CHC-12-04	-0.88	31.03	2.515	-3.811	-1.686	-10.101	9.68
14	3/6	2	CHC-12-04	-0.87	31.21	2.523	-3.637	-1.462	-9.454	8.507

[a]Reference Frame Interval

*Red samples or standards were excluded due to high mass-48 anomalies or leaks

Table C.2 Raw Clumped Isotope Data 2 of 2

Day	Date	Int.[a]	Name	D47	D48	D49
September 2014 run						
Heated Gasses and 25°C Waters						
1	9/9	1	MCBHG	-1.269	7.855	30.75
1	9/9	1	MixHG	-1.172	3.406	22.9
1	9/9	1	CararraHG	-0.752	5.137	-3.094
1	9/9	1	OoidsHG	-0.653	12.167	-9.689
1	9/9	1	AAS25C	-1.537	-0.701	82.278
2	9/10	1	MixHG	-1.167	-1.308	24.322
2	9/10	1	MCBHG	-1.294	0.174	33.024
2	9/10	1	MDIWHG	-2.198	-1.991	64.194
2	9/10	1	AAS25C	-1.617	-0.584	86.614
2	9/10	1	Evap25C	-0.753	12.03	20.692
2	9/10	1	MDIW25C	-1.28	0.554	59.197
3	9/11	1	CararraHG	-0.736	1.742	0.588
3	9/11	1	MixHG	-1.278	-6.316	33.751
3	9/11	1	Evap25C	-0.77	10.77	26.625
3	9/11	1	MDIW25C	-1.241	-1.308	59.803
4	9/12	1	MixHG	-1.137	-1.958	23.826
4	9/12	1	MDIW25C	-1.244	0.04	59.806
4	9/12	1	MDIW25C	-1.233	-0.321	60.398
6	9/14	2	MCBHG	-1.251	-8.21	65.274
6	9/14	2	AAS25	-1.64	-11.169	97.027
7	9/15	2	CarraraHG	-0.748	2.225	-2.451
7	9/15	2	AAS25C	-1.658	-9.422	89.112
8	9/16	2	CararraHG	-0.743	2.811	-2.936
8	9/16	2	Evap25	-0.781	7.228	23.981
9	9/17	2	Evap25C	-0.822	6.717	25.134
10	9/18	2	MixHG	-1.224	-5.713	28.013
11	9/19	2	MCBHG	-1.305	-6.278	35.281
11	9/19	2	MDIW25C	-1.288	-3.14	64.9
12	9/20	3	AASHG	-2.606	-11.048	89.614
12	9/20	3	AAS25C	-1.696	-11.301	93.761
14	9/22	3	MDIWHG	-2.281	-4.691	67.63
14	9/22	3	AAS25	-1.679	-12.209	100.959
15	9/23	3	CararraHG	-0.835	-0.902	5.024
15	9/23	3	Evap25C	-0.851	6.837	25.841
16	9/24	3	EVAPHG	-0.881	5.577	29.571
16	9/24	3	AAS25	-1.678	-10.949	91.765
18	9/26	3	MDIWHG	-2.222	-4.272	65.496
18	9/26	3	AAS25C	-1.692	-9.905	91.318
19	9/27	3	AASHG	-2.603	-9.761	89.452
19	9/27	3	Evap25C	-0.855	8.244	25.914
20	9/28	3	MixHG	-1.191	-5.207	26.744
20	9/28	3	AAS25C	-1.728	-11.073	91.76
21	9/29	3	Carrara2HG	-0.814	-1.043	3.754
21	9/29	3	MDIW25C	-1.367	-3.015	61.461
23	10/1	3	EvapHG	-1.955	2.006	43.5
Carbonate Standards						
3	9/11	1	Carrara1			
3	9/11	1	Carrara2	-0.444	1.929	-3.266
16	9/24	3	Cararra3	-0.395	2.362	-4.77
22	9/30	3	Carrara4	-0.451	0.645	-1.604
				-0.454	0.519	0.274
Samples						
5	9/13	1	NS-WP-079-V			
5	9/13	1	NS-WP-148-V	-0.974	-4.4	35.754
5	9/13	1	DO14-117-8-L	-0.922	-5.206	36.722
5	9/13	1	NS-WP-421-J	-0.619	-1.968	17.279
5	9/13	1	NS-WP-148-N	-0.731	36.026	19.319
7	9/15	2	NS-WP-079-V	-0.889	18.18	28.019
8	9/16	2	NS-WP-148-V	-0.993	-5.353	35.598
8	9/16	2	DO14-117-8-L	-0.933	-6.08	37.414

Day	Date	Int.[a]	Name	D47	D48	D49
8	9/16	2	NS-WP-079-V	-0.621	-2.283	18.188
8	9/16	2	NS-WP-421-J	-1.036	-6.647	38.49
8	9/16	2	NS-WP-148-N	-0.737	15.596	20.069
11	9/19	2	NS-WP-148-V	-0.883	11.448	29.662
11	9/19	2	DO14-117-8-L	-0.951	-6.624	37.291
12	9/20	3	NS-WP-421-J	-0.608	0.718	14.672
12	9/20	3	NS-WP-148-N	-0.722	11.68	21.104
16	9/24	3	NS-WP-079-V	-0.909	1.601	31.547
16	9/24	3	NS-WP-421-J	-1.011	-6.271	35.443
16	9/24	3	NS-WP-148-N	-0.754	6.959	21.542
16	9/24	3	NS-WP-079-N	-0.884	1.382	30.538
16	9/24	3	NS-WP-442-J	-0.823	70.312	23.191
21	9/29	3	NS-WP-442-J	-0.761	0.307	22.929
21	9/29	3	NS-WP-079-N	-0.761	-0.149	24.632
21	9/29	3	NS-WP-442-J	-0.792	12.602	25.783
22	9/30	3	NS-WP-079-N	-0.786	-0.917	23.778
				-0.772	20.679	21.651
December 2015 run						
Heated Gasses and 25°C Waters						
1	11/30	1	2xEVHG			
1	11/30	1	CarraraHG	-1.216	3.9	9.608
1	11/30	1	MDIWHG	-0.946	-3.27	16.862
1	11/30	1	2xEV25C	-1.654	-3.552	71.93
1	11/30	1	MDIW25C	-0.141	8.084	-21.053
1	11/30	1	Evap25C	-0.773	-2.636	67.899
2	12/1	1	2xEVHG	-0.494	2.576	27.366
2	12/1	1	2xEV25C	-1.177	6.958	-14.015
3	12/2	1	OoidsHG	-0.129	8.827	-23.8
3	12/2	1	MDIW25C	-0.749	22.982	-7.893
4	12/3	1	EvapHG	-0.764	-2.137	64.016
5	12/4	1	CarraraHG	-1.477	-1.151	54.207
5	12/4	1	Evap25C	-0.828	-1.044	0.089
6	12/5	1	MDIW25C	-0.483	2.656	27.355
7	12/6	1	EvapHG	-0.732	-2.313	70.043
7	12/6	1	2xEV25C	-1.422	0.265	38.484
8	12/7	1	OoidsHG	-0.133	8.832	-24.476
8	12/7	1	MDIWHG	-0.86	26.118	3.241
9	12/8	1	CarraraHG	-1.627	-1.975	64.862
9	12/8	1	Evap25C	-0.867	-2.516	10.73
11	12/10	1	EvapHG	-0.468	2.37	26.755
11	12/10	1	MDIW25C	-1.407	1.291	33.243
12	12/11	1	2xEV25C	-0.75	-1.115	60.322
13	12/12	1	2xEVHG	-0.15	8.982	-23.024
				-1.054	6.989	-9.87
Carbonate Standards						
2	12/1	1	Carrara1			
2	12/1	1	Carrara2	-0.535	-0.788	0.868
2	12/1	1	Ooids1	-0.496	-0.543	-0.197
2	12/1	1	Ooids2	-0.164	0.549	-15.837
4	12/3	1	Carrara3	-0.162	0.3	-7.864
6	12/5	1	Ooids3	-0.514	-0.796	-5.94
9	12/8	1	Carrara4	-0.164	0.086	-8.265
12	12/11	1	Ooids5	-0.482	-0.265	-5.41
13	12/12	1	Carrara5	-0.143	1.118	-12.39
				-0.521	-0.529	-0.789
Samples						
5	12/4	1	NS-WP-338-V			
6	12/5	1	NS-WP-056-J	-0.631	-3.644	36.343
6	12/5	1	NS-WP-442-J	-0.611	16.23	24.937
6	12/5	1	NS-WP-338-V	-0.623	-1.147	27.874
8	12/7	1	NS-WP-338-V	-0.632	-3.354	34.64
8	12/7	1	PL-12-09	-0.615	-3.522	35.171
8	12/7	1	NS-WP-442-J	-0.675	-4.253	38.792
8	12/7	1	PL-12-09	-0.618	-1.995	27.606
				-0.735	-5.002	40.851

Day	Date	Int.[a]	Name	D47	D48	D49
February 2016 run						
Heated Gasses and 25°C Waters						
1	2/22	1	EvapHGleaky			
1	2/22	1	2xEV25C	-1.529	-0.49	43.005
1	2/22	1	CarraraHG	-0.159	8.931	-26.591
1	2/22	1	OoidsHG	-0.862	-1.592	1.721
2	2/23	1	MDIW25C	-0.928	-3.554	17.322
2	2/23	1	Evap25C	-0.813	-2.82	67.079
2	2/23	1	MDIW25C	-0.525	2.344	26.15
2	2/23	1	2xEVHG	-0.798	-2.507	65.413
3	2/24	2	EvapHG	-1.27	3.47	14.2
4	2/25	2	2xEV25C	-1.552	-0.88	48.484
5	2/26	2	Evap25C	-0.134	9.504	-27.317
5	2/26	2	MATHHG	-0.531	2.516	24.755
6	2/27	2	OoidsHG	-1.005	-2.606	18.189
7	2/28	2	MDIW25C	-0.76	-1.339	-2.286
7	2/28	2	2xEVHG	-0.82	-2.725	65.07
8	2/29	2	2xEV25C	-1.175	7.075	-5.171
8	2/29	2	MATHHG	-0.181	12.256	-30.53
9	3/1	2	Evap25C	-1.031	-2.329	18.64
9	3/1	2	CarraraHG	-0.545	2.639	25.894
10	3/2	2	MDIW25C	-0.394	0.273	5.76
11	3/3	2	OoidsHG	-0.861	-2.72	62.822
12	3/4	2	2xEV25C	-0.698	126.829	-25.266
13	3/5	3	EvapHG	-0.149	10.762	-27.742
14	3/6	3	Evap25C	-1.704	-2.659	60.03
14	3/6	3	MDIWHG	-0.591	2.822	27.534
				-1.841	-4.602	70.467
Carbonate Standards						
2	2/23	1	Carrara1			
2	2/23	1	Carrara2	-0.547	-1.019	0.346
2	2/23	1	Ooids1	-0.548	-0.863	0.787
4	2/25	2	Ooids3	-0.196	-0.038	-8.379
6	2/27	2	Carrara3	-0.17	0.108	-9.424
8	2/29	2	Ooids4	-0.498	-0.665	-0.582
10	3/2	2	Carrara4	-0.194	0.135	-9.128
12	3/4	2	Ooids5	-0.502	-0.405	-3.013
14	3/6	2	Carrara5	-0.136	0.514	-11.482
				-0.516	-0.743	-1.349
Samples						
4	2/25	2	NS-WP-148-N001			
6	2/27	2	PI2-52-2	-0.717	-1.196	32.583
6	2/27	2	WC18-47-9	-0.717	-2.385	26.73
6	2/27	2	WC18-49-7	-0.784	-1.978	32.95
7	2/28	2	PI2-52-2	-0.545	-2.463	16.571
7	2/28	2	WC18-49-7	-0.701	-2.672	29.178
9	3/2	2	WC18-49-7	-0.534	-2.591	16.185
10	3/2	2	PI2-50-2	-0.528	-2.539	15.5
10	3/2	2	NS-WP-442-J	-0.738	-2.88	30.201
10	3/2	2	PL-12-09	-0.631	-0.28	22.596
13	3/5	2	DO6-62-9	-0.702	-5.835	37.252
13	3/5	2	DO6-62-9	-0.531	-2.063	13.178
13	3/5	2	PI2-50-2	-0.527	-2.298	14.237
13	3/5	2	DO6-62-9	-0.727	-3.072	28.706
14	3/6	2	CHC-12-04	-0.524	-2.081	13.232
14	3/6	2	CHC-12-04	-0.494	-2.783	13.644
14	3/6	2	CHC-12-04	-0.521	-2.512	14.574

[a]Reference Frame Interval

*Red samples or standards were excluded due to high mass-48 anomalies or leaks

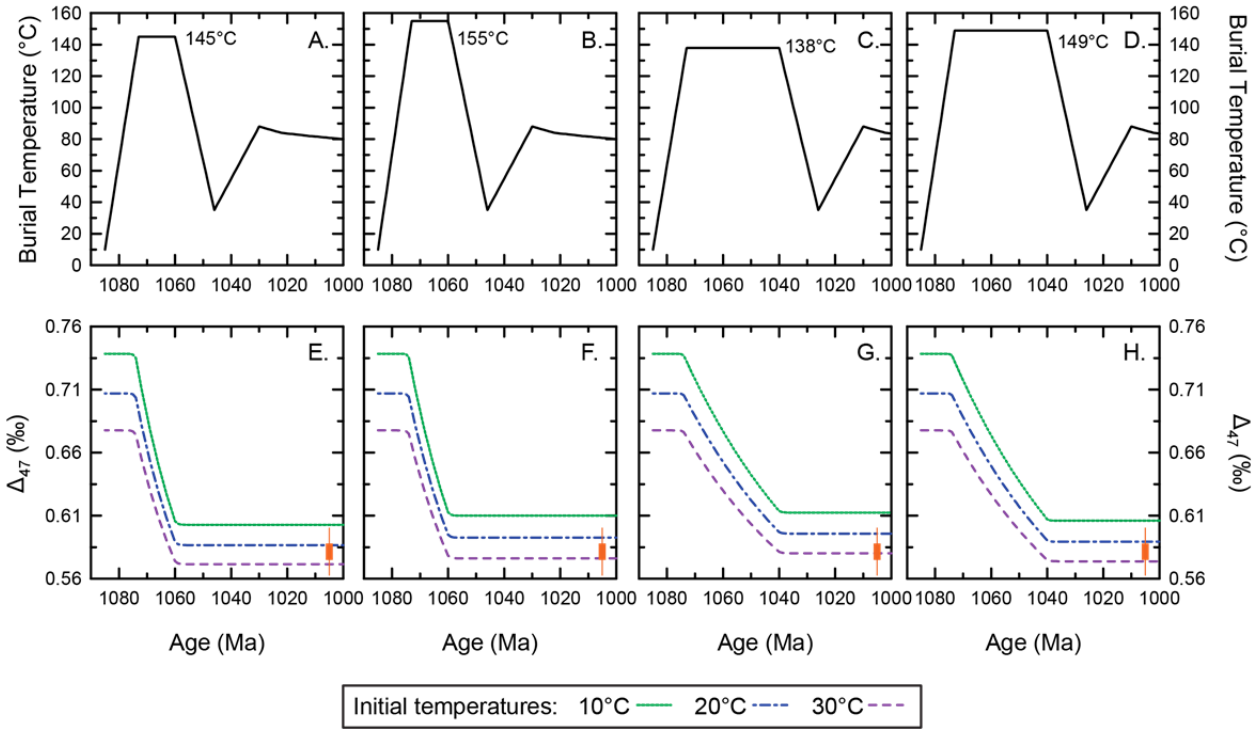

Figure C.1

Solid state reordering modelling results when varying the initial Δ_{47} value. A–D plot the different thermal history scenarios. E–H plot the modelled reordering results corresponding to the above thermal history at initial temperatures of 10, 20, and 30°C. The thick orange vertical line represents the observed range of Δ_{47} values from the sedimentary/early-diagenetic pool, and the thin orange line corresponds to the error window of this sample pool